Low-Speed Performance Enhancement using Localized Active Flow Control

Localized Active Flow Control Simulations on a Reference Aircraft (2/4)

Arvin Shmilovich, The Boeing Company
Paul Vijgen, The Boeing Company
Rene Woszidlo, The Boeing Company

April 27, 2022

Table of Contents

List of Figures

Nomenclature

Parameters

A_{ref}	Wing reference area
A	Area vector
α	Angle of attack
β	Yaw angle
C_D	Airplane drag coefficient
C_L	Airplane lift coefficient
$C_{L,max}$	Maximum lift coefficient
C_m	Airplane pitching moment coefficient
C_μ	Total momentum coefficient, $\dot{m}u_j/(0.5\cdot\rho_\infty u_\infty^2 A_{ref})$
C_p	Pressure coefficient
C_q	Mass flow coefficient, $m_j/(\rho_\infty u_\infty A_{ref})$
η	Actuation efficiency
L/D	Lift-to-drag ratio
M	Mach number
$\dot{m}$	Mass flow
P_{0in}	Motal pressure at the actuator inlet
$P_{0\infty}$	Freestream total pressure
PR	Total pressure ratio, $P_{0in}/P_{0\infty}$
PT	Normalized total pressure, $P_0/P_{0\infty}$
Re	Reynolds number based on mean aerodynamic chord
ρ	Density
T_{0in}	Total temperature at the actuator inlet
$T_{0\infty}$	Freestream total temperature
TR	Total temperature ratio, $T_{0in}/T_{0\infty}$
U	Velocity vector
u_∞	Freestream velocity
x,y,z	Streamwise, spanwise and vertical coordinates, respectively

Subscripts

in	Actuator inlet
j	Actuation jet
th	Actuator throat
∞	Freestream
0	Stagnation

Abbreviations

1D	One dimensional
3D	Three dimensional
AFC	Active flow control
APU	Auxiliary Power Unit
CD	Convergent-divergent
CFD	Computational Fluid Dynamics
CRM-HL	High Lift Common Research Model
GD	Gas dynamics
IB, OB	Inboard, outboard
LE	Leading edge
NASA	National Aeronautics and Space Administration

OML	Outer mold line
RANS	Reynolds-averaged Navier-Stokes
SA	Spalart-Allmaras turbulence model
WUSS	Wing under-slat surface

Executive Summary

A study of the potential implementations of localized active flow control (AFC) technology onto future airplanes is presented. This collaborative investigation addresses key objectives of the NASA Advanced Air Transport Technology (AATT) Project, in terms of reduction in fuel consumption and lower emission. It specifically targets the goals set forth in a roadmap developed by the NASA/Boeing team. The roadmap is a result of a series of meetings held between the two parties over the years and it represents a shared vision for practical implementations, leading up to flight demonstrations of localized flow control. If successful, localized flow control may lead to important ramifications for next generation airplanes from both the economic and environmental perspectives.

Under this contract localized AFC has been used to improve aerodynamic performance during high-lift operations using Computational Fluid Dynamics (CFD). Specifically, AFC has been applied at the aileron and at various locations in the wing leading edge (LE) regions. The applications target reduced drag and enhanced lift over the range of practical angles of attack, including stall. These benefits translate to airplane performance improvements, such as longer range or larger payload. The CFD results are used to quantify potential aerodynamic benefits, as well as the input required for actuation. This helps identify the most promising candidates, which potentially provide material net airplane level enhancements using onboard fluidic sources.

The airplane configuration selected for the CFD study is a representative of a future short/medium-range twin-engine airplane dubbed the Reference Aircraft. A slew of AFC applications has been explored and their aerodynamic performance enhancements were benchmarked against the baseline Reference Aircraft. Promising AFC candidates have been deemed practical and potentially suitable for both the aileron and the wing LE implementations. The findings on the Reference Aircraft are used to guide the development of the AFC-enhanced aileron for the CRM-HL. The wind-tunnel model of the CRM-HL will be used by NASA to validate the AFC concepts, complementing the CFD-based analysis and the integration study (final report document #3).

1 Introduction

The need for improved aerodynamic efficiency through the application of AFC has motivated a number of studies over the years. In a recent study sponsored by NASA under the Advanced Transport Technology Project (AFC-Enabled Simplified High-Lift System Integration Study, Contract/Task Order NNL10AA05B/NNL13AB65T), Boeing investigated potential benefits of reducing the cruise drag associated with modern high-lift systems. Although the performance benefits are tantalizing, that specific application dictates significant architectural changes to the aircraft, rendering it likely impractical for implementation in the next 15-20 years. Therefore, an intermediate application that matures and transitions AFC design and system capabilities in preparation for broader aircraft configuration changes is desired.

A pathway toward more practical implementations might utilize localized AFC applications with limited architectural impact on the aircraft. The prospective use of localized AFC has become especially relevant after the successful demonstration of a full-scale AFC system in flight under a collaborative project between NASA and the Boeing Company [1]. In view of these findings, this proposal focuses on a set of applications targeting smaller regions of the airframe, yet are expected to offer meaningful net performance enhancements with manageable system integration.

Localized AFC applications to commercial transports may lead to substantial environmental and economic advantages for airplane operators. In particular, enhanced high-lift performance is one of the key objectives in aircraft design. Considering takeoff as an example, since the lift-to-drag ratio (L/D) is a major determinant of performance, an increase in L/D allows for larger airplane payload, reduced runway length, or longer range, which translates to substantial economic advantages. Such benefits are illustrated by using several trade factors for a long range two-engine transport [2]:

- A 1.5% increase in maximum lift coefficient is equivalent to a 6,600 lb increase in payload for a fixed approach speed.
- A 1% increase in takeoff L/D is equivalent to a 2,800 lb increase in payload or a 150 nm increase in range.
- A 0.1 increase in lift coefficient at constant angle of attack is equivalent to reducing the approach attitude by one degree. As a result the landing gear may be shortened for a savings in airplane weight of 1,400 lb.

Moreover, the takeoff and climb-out portions of the flight profile often determine the engine rating and thereby the engine core size. Therefore applications that improve the L/D will enable a reduction in the engine core size, resulting in lower airplane weight. Consequently, this will lead to lower fuel consumption and reduced emissions. It is noted that comparable gains can be realized for a short/medium range airplane like the Reference Aircraft considered here.

Motivated by these performance metrics, Boeing has recently (prior to this contract) initiated exploratory studies of new flow control concepts for high-lift applications using CFD. The new concepts include customary methods for reduced flow separation as well as unconventional approaches that target additional parameters for enhanced aerodynamic performance. This strategy offers a wider range of opportunities, improving the odds of identifying promising candidates for subsequent development. Promising approaches identified by Boeing for further development under this contract target different areas of the wing for AFC implementations. In one application, AFC is used to improve aerodynamic performance of ailerons, which are customarily deflected during high-lift operations. AFC can also be used at specific locations on the wing LE in conjunction with slats in order to enhance the performance of the high-lift system.

The overarching objective of this program is to develop a trade study and business case for the localized AFC applications that could be inserted into the technology development pipeline for upcoming commercial aircraft. This CFD report describes the computational simulations phase of the study. Boeing has heavily leveraged the experience gained from the preceding NASA HL-CRM/AFC contract (refer to the Introduction). The Reference Aircraft will be used at the relevant flight conditions (takeoff and landing, sealed and gapped slats, etc.) with relatively modest configuration changes to accommodate AFC implementations (e.g., larger aileron deflections). Various AFC layouts and actuation techniques will be

considered for the aileron and wing LE applications. By and large, the AFC methods will be designed for the least amount of actuation power required for a specific design goal. The predicted aero data are used to establish airplane performance gains and to facilitate the integration phase of the study (final report document #3 [3]).

2 Geometry of Reference Aircraft

The Reference Aircraft was selected for the study of AFC. It represents a future, short/medium-range, twin-engine transonic airplane. The geometry definition, which includes fuselage, wing, Krueger flaps, slats, single-element flaps, nacelle/chine, aileron, etc., was adequate for CFD analysis. Detents of the high-lift elements were also available. Additional information on the structural layout, propulsion system, optional fluidic and power sources, and weights data for performance analysis and sizing, will be used in the integration study of the final report document #3 [3].

High-lift geometries for takeoff and landing are considered. The takeoff configuration consists of a system of sealed slats and a Fowler flap system whose elements are deployed to the takeoff settings. At takeoff the ailerons are symmetrically deflected to a nominal angle. The landing configuration employs a slotted slat system and flaps at appropriate detents. Customarily the ailerons aren't deflected during landing. The high-lift system includes sealed Krueger flaps in the regions between the fuselage and engine pylons for both the takeoff and landing conditions.

3 Computational Approach

This section describes the computational strategy, the geometry setup and the grid system for the Reference Aircraft. Limited validation for the baseline flow without AFC was performed for two relevant geometries using both flight and wind tunnel data. This is a necessary confidence building step before embarking on the exploratory nature of this AFC study.

3.1 Computational Method

The computational tool used for flow control is a modified version of the OVERFLOW code originally developed by NASA [4] and it forms the core process of Boeing's transport aircraft CFD in the context of AFC. OVERFLOW is based on the unsteady Reynolds-averaged Navier-Stokes (RANS) formulation for overset grid systems. The numerical procedure has been modified to simulate flows for a family of flow control techniques [5,6]. These include constant blowing, pulsed suction/blowing, swiveling jets (sprinkler), fluidic oscillators and traverse actuation. The simulation tool has been generalized for large systems of actuators [7-9]. In most flow control applications, the computational domain contains the relevant physical region. It consists of the inner regions of the actuators and the external domain, enabling a complete simulation that captures the interplay amongst the actuator jets and the surrounding flow, irrespective of the actuation input. This coupling approach is adequate for any input pressure, whether the actuator flow is subsonic, choked, or intermittently subsonic/supersonic.

In this study the second-order Roe upwind-differencing scheme is used with the ARC3D diagonalized Beam-Warming scalar pentadiagonal scheme on the right hand-side. The Spalart-Allmaras (SA) turbulence model has proven robust in the context of the highly separated flows and is used for the simulation cases presented here. The time stepping scheme is second-order as demonstrated in the framework of AFC using a system with multiple actuators [7]. The numerical procedure has been extensively validated for numerous applications of AFC [7, 10] through both wind tunnel settings and flight testing [8]. The validation studies include the characterization of flow control devices for the range of practical actuation parameters, as well as the performance of airplanes equipped with large systems of actuators.

Further details on the numerical setup will be provided for the respective applications.

3.2 Geometry Setup and Grid System

A set of geometrical simplifications were introduced to the Reference Aircraft in order to allow for quicker computational turnaround without compromising the modeling of the flow control effects. The horizontal tail, the landing gear and the brackets of the LE devices, as well as the flap track fairings have been excluded from the computational model. Flow-through engines are used in all the simulations presented here. The wing is rigid, and therefore, no aeroelastic effects are accounted for in the simulations.

No yaw conditions are considered here, so the simulations are performed on half of the airplane and assume a vertical plane of symmetry.

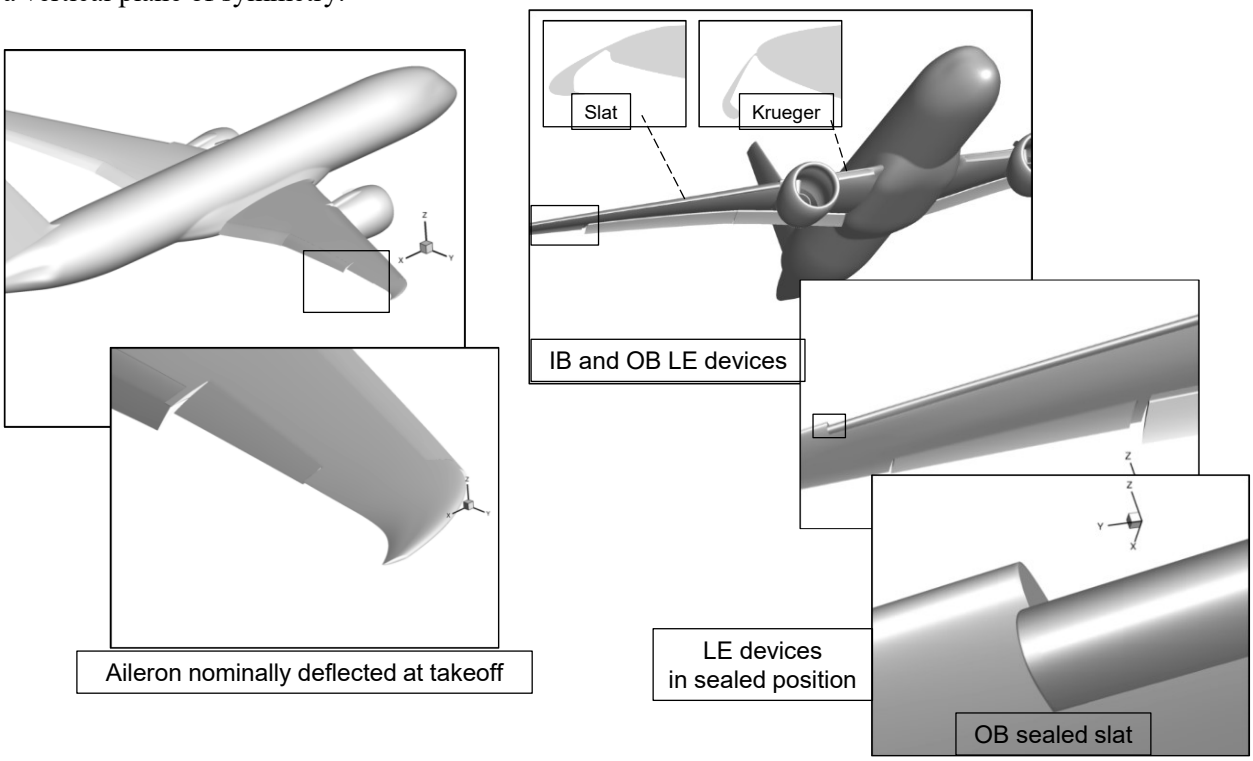

Figure 1 – Takeoff geometry used in the modeling of the Reference Aircraft.

The geometry of the surface grids in Figure 1 shows close views of the aileron and the slat in the takeoff positions. The single-element flap is deflected to 20°. The aileron is deflected to a nominal angle of 7.5° as customarily used on contemporary takeoff procedures. The wing LE consists of a sealed Krueger flap inboard of the engine station. Outboard of the engine there are four slat elements, which are in the sealed position. In the majority of the simulations, the slats are treated as a continuous element, unless otherwise noted.

3.3 Code Verification

It is highly desirable to gain confidence in the validity of the computational simulations for AFC using experimental data. However, due to the investigative nature of this study, validation cannot be performed at the present time. Nevertheless, code verification for the baseline flow without AFC was performed for two relevant geometries. The first configuration represents a contemporary short/middle-range airplane. The computational model includes all the relevant high-lift components. Figure 2 shows the CFD geometry and the computed lift compared to measured flight data, indicating good agreement in the range in which data are available.

The second configuration is the Reference Aircraft that will be subsequently used for the AFC study. Here, in lieu of validation, the OVERFLOW solutions have been verified with results obtained with another RANS code. CFD++ is a general purpose RANS code that uses a finite volume solver [11]. It is noted that the CFD++ solutions were obtained prior to this contract. Those results were obtained on an unstructured grid system using the SA turbulence model. The OVERFLOW settings were generally aligned with the CFD++ setup.

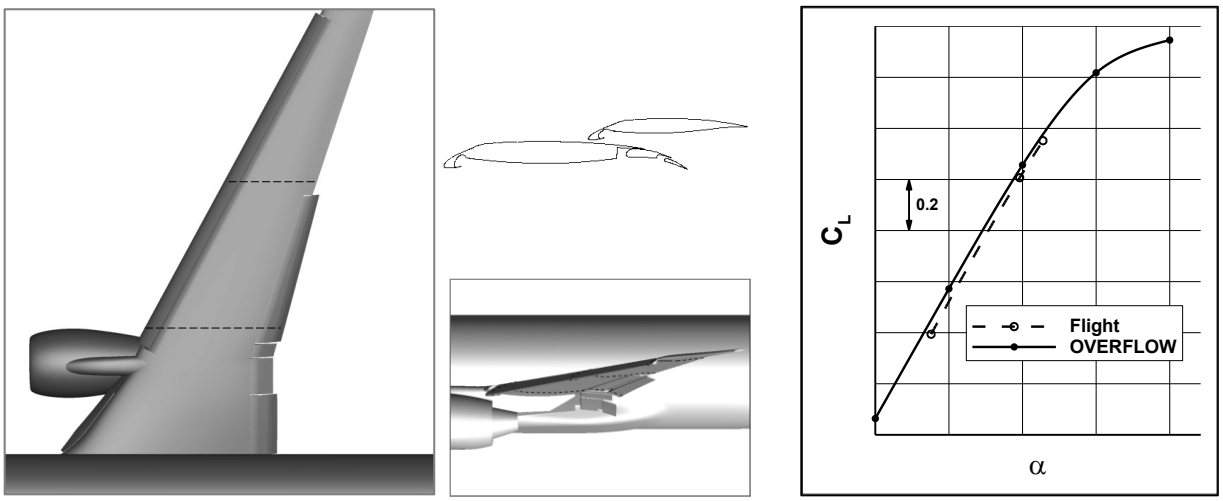

Figure 2 – Validation of OVERFLOW with flight measured data at takeoff conditions.

The OVERFLOW and CFD++ simulations were performed for the takeoff configuration in Figure 1, which consists of sealed LE devices and aileron set at a nominal deflection of 7.5°. A slight difference in the CFD geometries exists as CFD++ includes the flap track fairings while OVERFLOW does not. The solutions were obtained in free air and with fully turbulent flow. The freestream Mach number is 0.26 and the Reynolds number is 6 million based on the mean aerodynamic chord. Comparisons of the aerodynamic forces between OVERFLOW and CFD++ is shown in Figure 3. Generally, there is a very good agreement in the linear range of the lift curve, although some differences are noticeable in L/D. Aside from the geometrical difference, another factor that might have contributed to these discrepancy is that CFD++ solutions were obtained using low Mach number preconditioning.

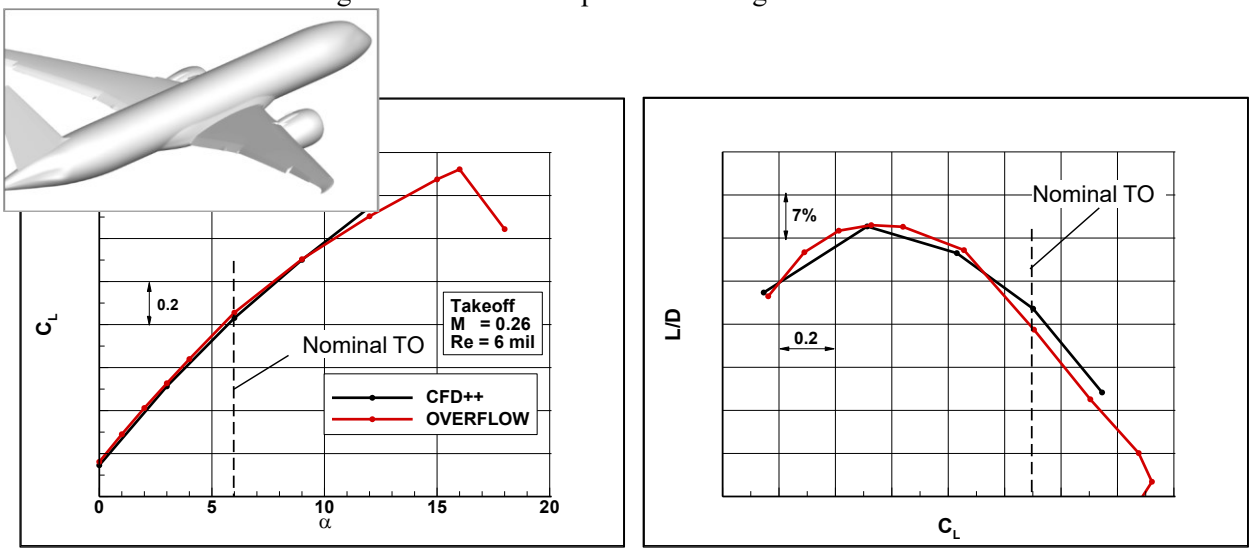

Figure 3 – Comparison of OVERFLOW and CFD++ of the baseline Reference Aircraft at takeoff, M_∞=0.26, Re=6 million.

Based on these code verifications, combined with extensive AFC validation performed previously on numerous AFC applications (Section 3.1), the OVERFLOW code is deemed appropriate for evaluation of AFC concepts per the objectives of this study.

4 Localized AFC Concepts

AFC concepts for high-lift applied to the aileron (Section 4.1), the wing LE devices (Section 4.2) and the nacelle/pylon/wing (Section 4.3) are explored for both takeoff and landing conditions. The approaches target reduced drag and enhanced lift over the range of practical angles of attack, including stall. Another objective is to provide solutions for the integration of the high-lift system with high-by-pass-ratio engines (Section 4.3). A set of optional AFC layouts have been analyzed and promising candidates have been identified based on improved aerodynamic performance relative to the input required for actuation. All along this study the new AFC concepts have been developed while continually taking into consideration aspects of integration. The practicality of the AFC implementations will be assessed in the integration study (final report document #3 [3]).

The flow control approaches considered here include constant blowing from a variety of nozzle shapes. Based on Boeing's experience, actuation based on constant blowing is also a suitable proxy for unsteady actuation that, depending on actuation parameters, could potentially provide higher efficiencies.

4.1 AFC on a Deflected Aileron

Customarily, the ailerons are drooped to a nominal angle to produce high L/D during takeoff. As the aileron is deflected, the increase in wing camber results in added lift. The higher lift leads to increase in the form and the induced components of drag. Although total airplane drag increases too, if the aileron deflection is sufficiently small, a net increase in L/D can be realized. At larger aileron deflections, however, flow separation develops, and the associated drag increase becomes prohibitive, resulting in a drop in L/D. This places a limit on the L/D that can be achieved using drooped ailerons. This constraint can be addressed by improving the flow quality on the aileron. In this application AFC is used in conjunction with ailerons deflected to higher angles in order to enhance their effectiveness. Following subsections summarize the baseline flow over the aileron, as well as various AFC configurations and parameters over a deflected aileron.

4.1.1 Baseline Flow

The first set of results is used to gain insight into the flow development as a function of aileron deflection for the baseline unactuated flow. The aileron is deflected at 0°, 7.5°, 12°, 16° and 25°, where 7.5° is considered the nominal angle for takeoff (also dubbed nominal aileron). The freestream Mach number is 0.20 and Re=6 million. The nominal angle of attack at takeoff is 6°.

Figure 4 shows the flow fields for the 0°, 7.5° and 25° aileron deflection angles in terms of the surface pressure distributions, the flow separation bubbles (in either blue or gray for clarity) and the normalized total pressure, PT, at a set of cross-sectional cuts just downstream of the wing. At these conditions, the baseline flow fields contain pockets of flow separation along the trailing edge of the flaps. The flow is fully attached on the undeflected aileron, but progressively larger flow separation forms at increasingly higher angles, triggered by the adverse pressure gradient close to the hinge line. At the nominal deflection, the flow is separated at the trailing edge of the aileron. However, at the 25° deflection the entire aileron is separated, indicating a thicker wake with larger total pressure loss. This is indicative of higher drag. The total pressure also indicates that the tip vortex elements get stronger, commensurate with the increased aileron loading at the largest deflection. The tip vortex from the inboard edge of the aileron is particularly coherent.

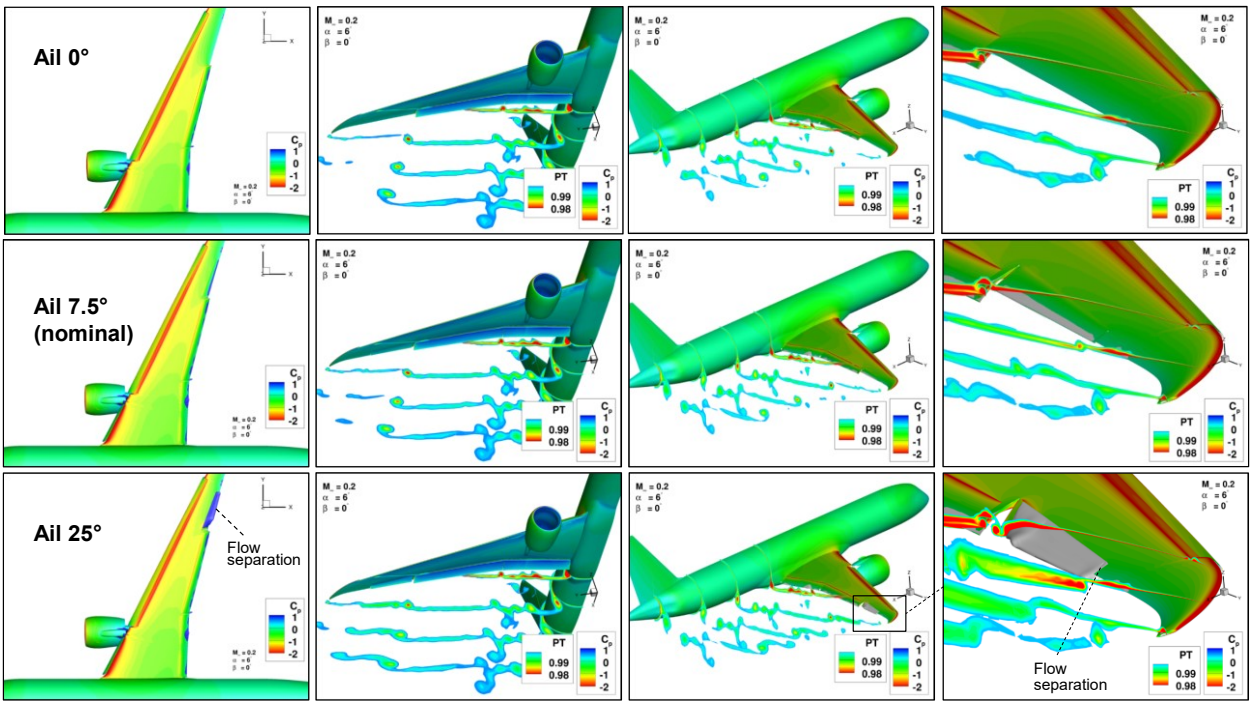

Figure 4 – Baseline flows fields for the different aileron deflections at the nominal takeoff condition (α=6°).

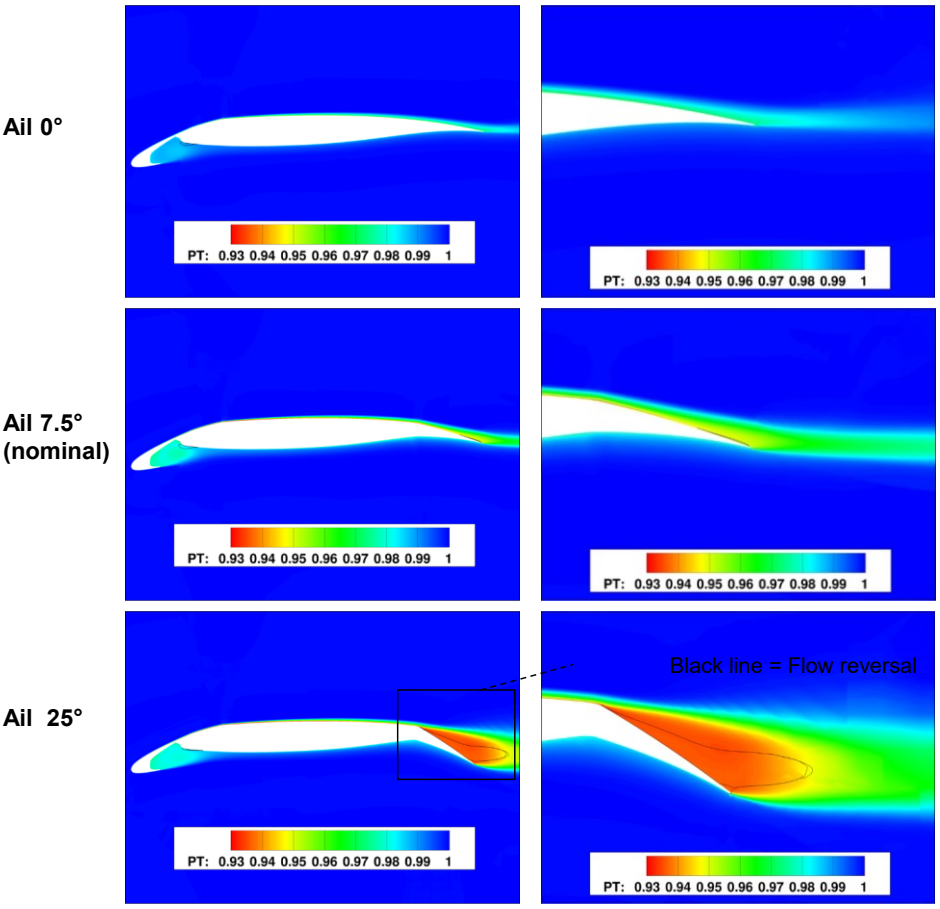

Figure 5 – Baseline flow: total pressure contours at the midaileron cross sections.

Figure 5 shows the total pressure contours at the midaileron cross sections, where the black lines denote the regions of flow reversal. Figure 6 presents the span load and the pressure distributions at the midaileron sections. The higher aileron deflections help increase the wing load in the aileron span segment. This load augmentation extends toward the tip due to the wing sweep. The sectional pressure distributions indicate that as the aileron is deflected, the increased wing camber results in increased global circulation affecting the entire wing section, and hence higher sectional lift. As the aileron is deflected to higher angles, the flow starts to separate and drag becomes significant. This is clearly shown in the aerodynamic performance in Figure 7, where the drag increment at large deflections is such that L/D drops at around 10°. Here the dashed lines denote the nominal aileron deflection of 7.5°. The goal is to augment L/D beyond the level achieved with the nominal aileron deflection by using larger aileron deflection in conjunction with flow control. Specifically, AFC will be used to lower the pressure drag by reducing flow separation, and the induced drag through spanload redistribution.

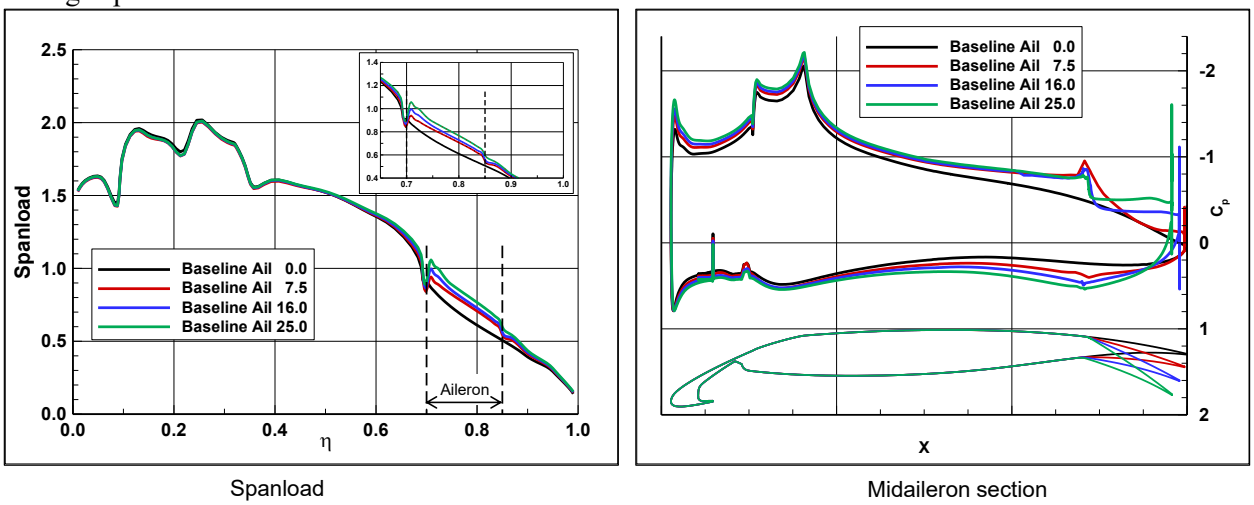

Figure 6 – Baseline flow: span load and pressure distributions at the midaileron sections.

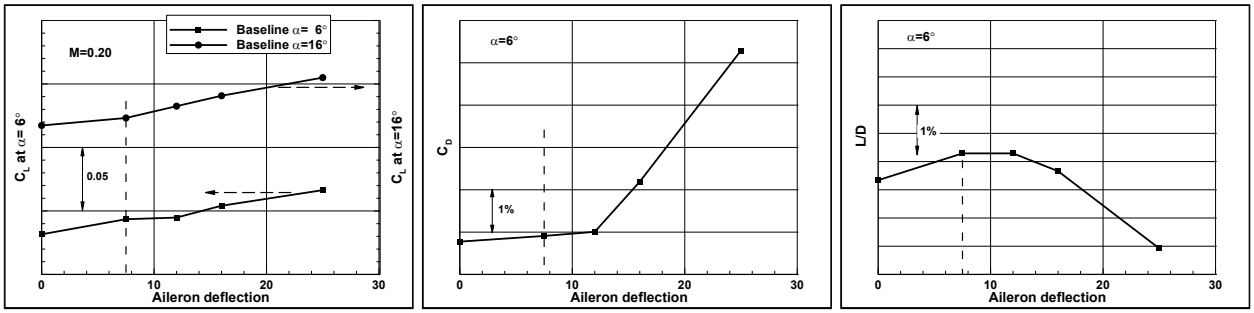

Figure 7 – Baseline flow: aerodynamic performance as function of aileron deflection.

4.1.2 Surface Blowing

Since AFC analyses place considerable demands on computational resources, it is necessary to adopt a systematic approach that is practical, with the goal of quickly identifying most effective AFC implementations. The analysis process evolved through a sequence of progressively complex flow control representations, starting off with surface boundary conditions, up to systems that include dozens of discrete nozzles. Selected results illustrating the design process are discussed hereafter.

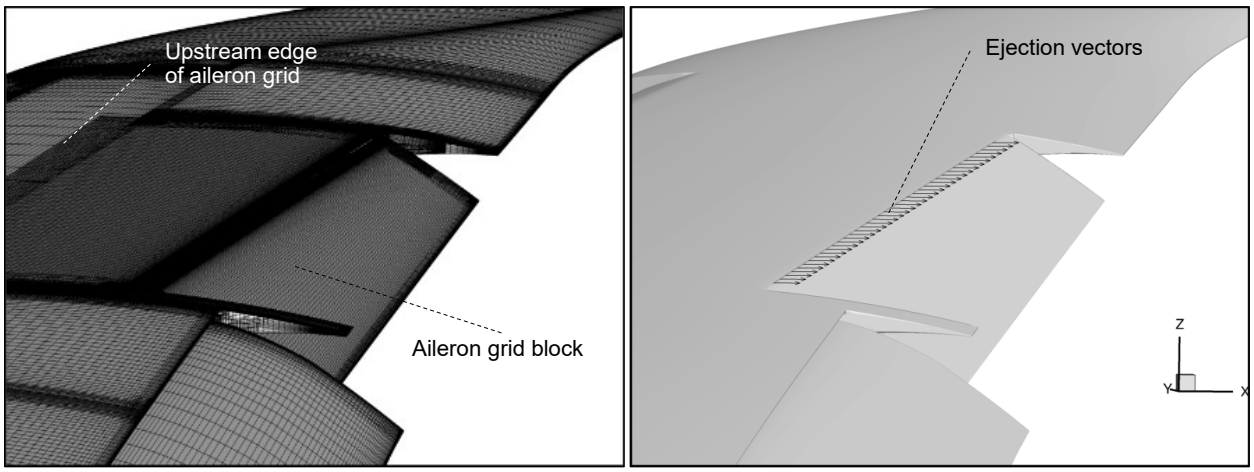

Figure 8 – Approach for the modeling of surface blowing jets.

A set of flow control cases utilizing constant surface blowing is first considered. This is a quick step that helps guide port placement and orientation of the blowing jets. Surface boundary conditions are applied on the outer mold line of the wing, where the blowing velocity is defined by the mass flow rate and the stagnation pressure and temperature. The actuation is applied just downstream of the aileron hinge line. The blowing jets are perpendicular to the respective hinge lines (when viewed from the top) and they create an angle of 25° relative to the local surface. A very fine grid block is placed in that region for the application of the blowing jet and for capturing the interaction between the jet and the surrounding flow. This block extends from around the midchord station on the wing upstream of the aileron and extends beyond the aileron trailing edge. The boundary condition is applied on a narrow strip of constant width of 0.22% of wing chord length at the midaileron station. The strip contains 16x170 cells in the streamwise and spanwise directions, respectively. The grid consists of 76 million points and 211 subgrids. This modeling approach is illustrated in Figure 8 for an aileron deflection of 25°. All solutions using the surface blowing are obtained for the 25° deflection.

Figures 9 through 11 present the results of a jet that spans the entire aileron, pointing in the x direction with PR=2 and TR=1. TR=1 will be used in all actuation patterns throughout this report, unless otherwise noted. The flow field in Figure 9 was obtained at α=6° and it is compared with the baseline cases for the aileron at the 7.5° and the 25° from Figure 4. This particular jet is very effective in eliminating the flow separation. The intensity of the aileron vortex sheet has been considerably reduced. The two distinct tip vortices are the results of the increased loading on the aileron. The total pressure contours at the midaileron section in Figure 10 shows that the circulation produced by the streamlining effect at the aileron affects the entire flow field, including the slat cove. The blowing jet affects the flow upstream of the hinge line, where the thickness of the viscous layer is noticeably reduced. The impact of AFC on the aerodynamic performance is shown in Figure 11. Flow control results in increased lift over the lift range, including $C_{L,max}$. The span load obtained with flow control, which is closer to an elliptical distribution, and the reduced separation result in lower drag. This results in significantly higher L/D. The increased loading at the aileron results in a nose-down pitching moment, resulting in potential trim drag penalty which needs to be accounted for. It is noted that the drag levels throughout this CFD report are untrimmed. Trim drag effects will be addressed in the integration study (final report document #3 [3]).

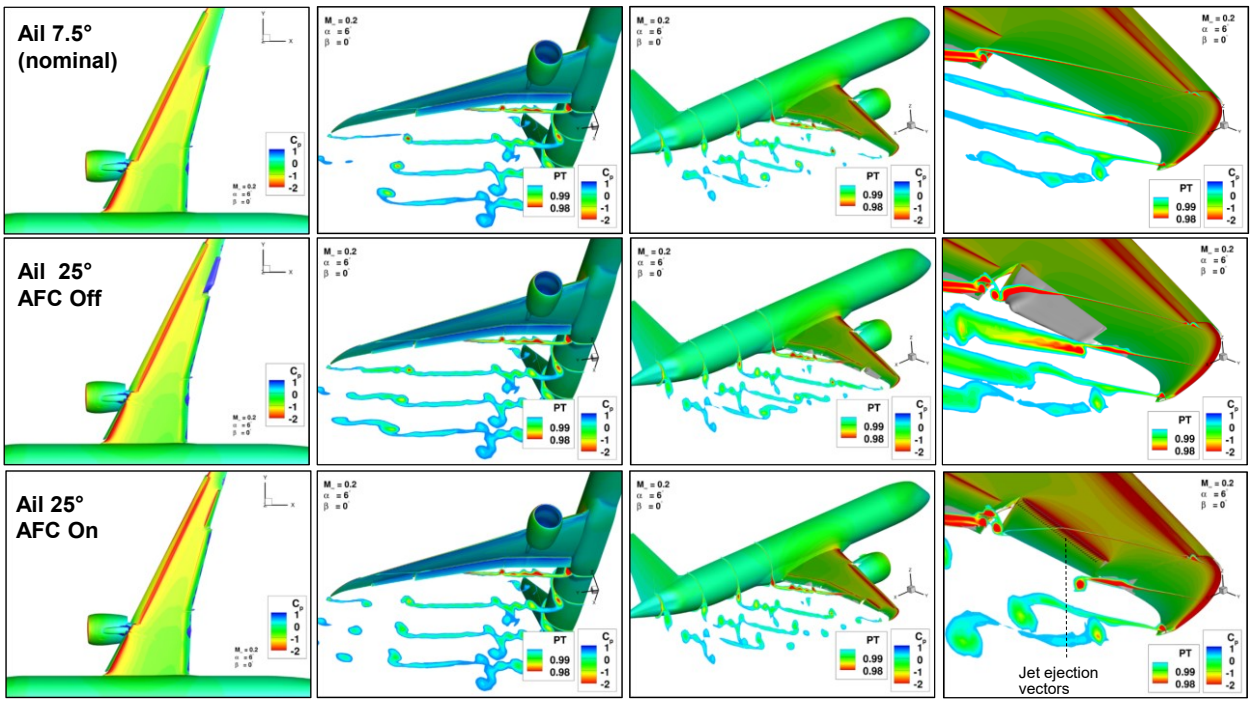

Figure 9 – Flows fields for the nominal aileron deflection, and the baseline and AFC actuation on the 25° aileron (α=6°).

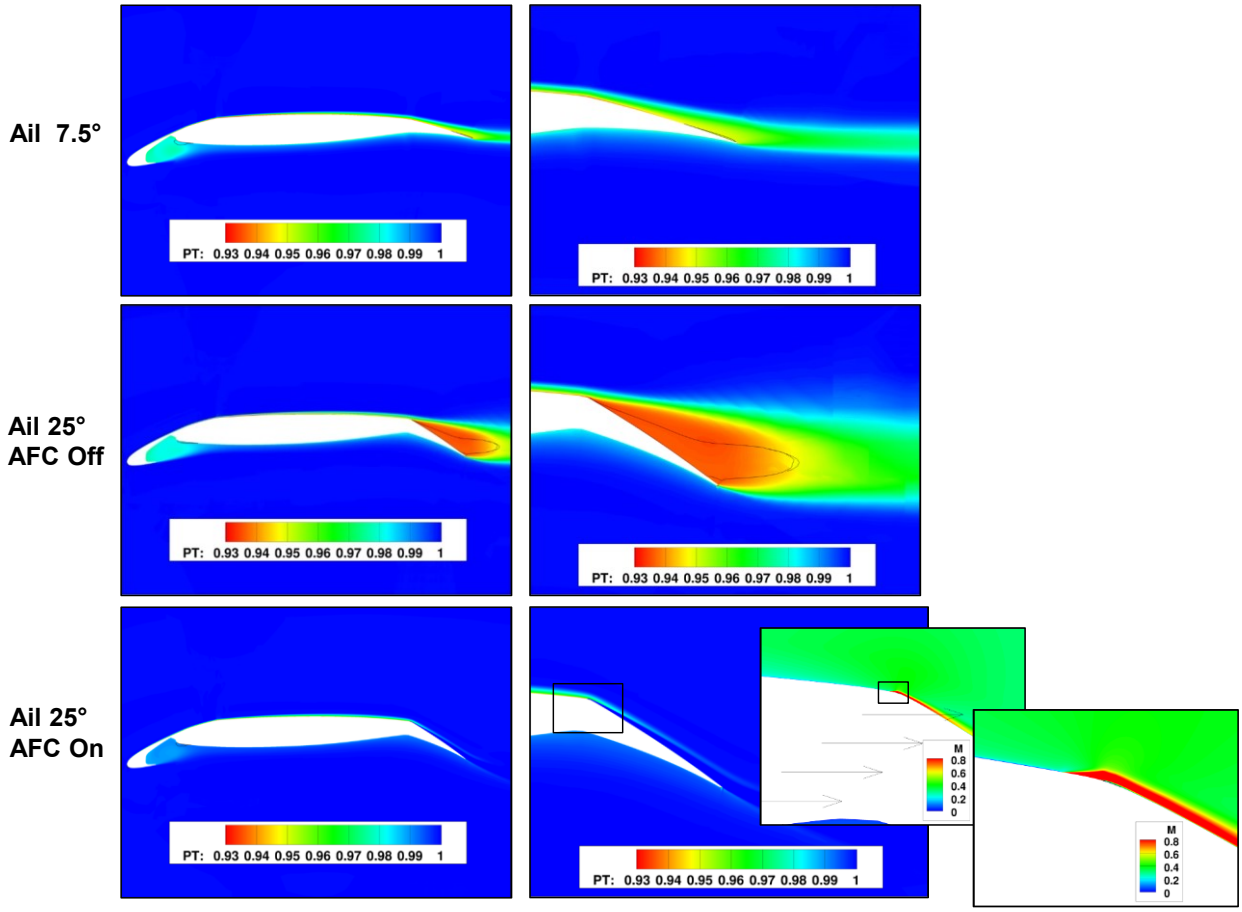

Figure 10 – Flows fields at the mid aileron section for the cases in Figure 9.

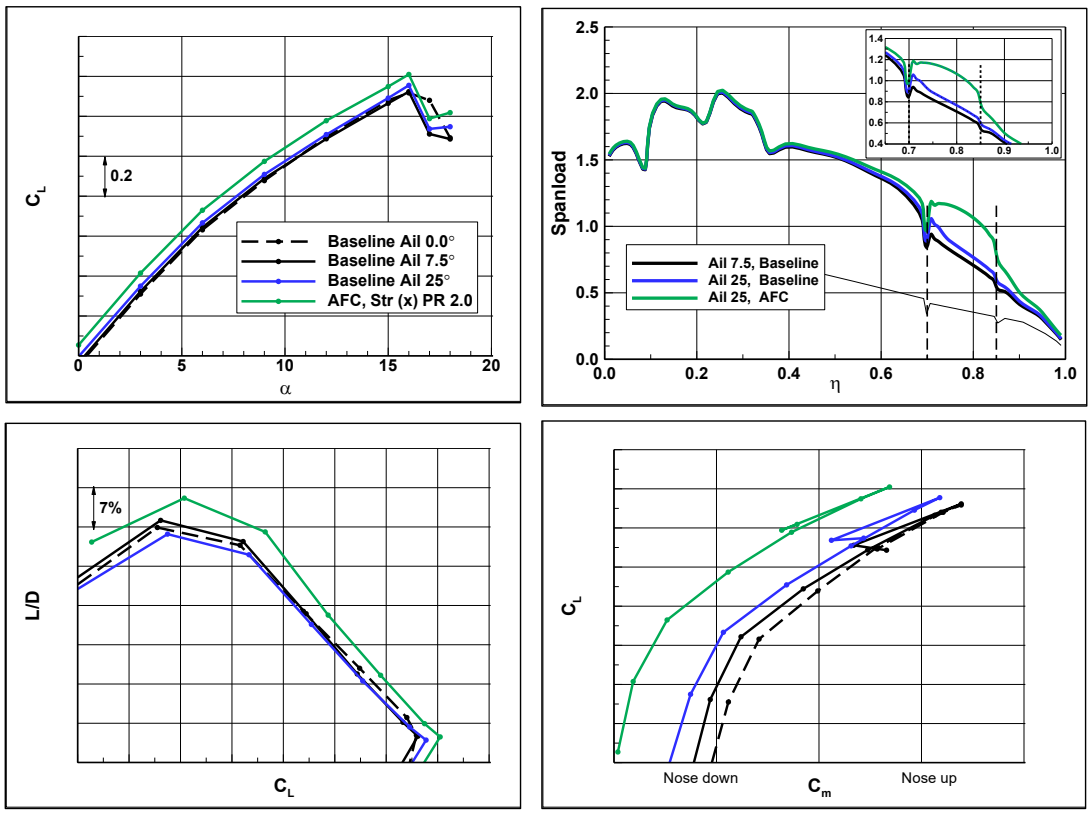

Figure 11 – Aerodynamic performance due to jet with PR=2.

The sensitivity to jet intensity is analyzed in Figures 12 and 13 at α=6°. Here the PR varies from 1.05 to 2. Relative to the baseline case, the addition of momentum with increased actuation intensity helps to gradually attach the flow. The flow is effectively attached at a relatively low PR of 1.2. The increased camber effect results in added lift in the outboard wing segment. Combined with the reduction in drag, flow control results in improved L/D over the input pressure range. As the pressure ratio increases the force and moments increase as depicted in Figure 13. Choosing the best actuation parameters for an efficient and practical flow control system is a critical design criterion and it will be the central theme throughout the remainder of this report.

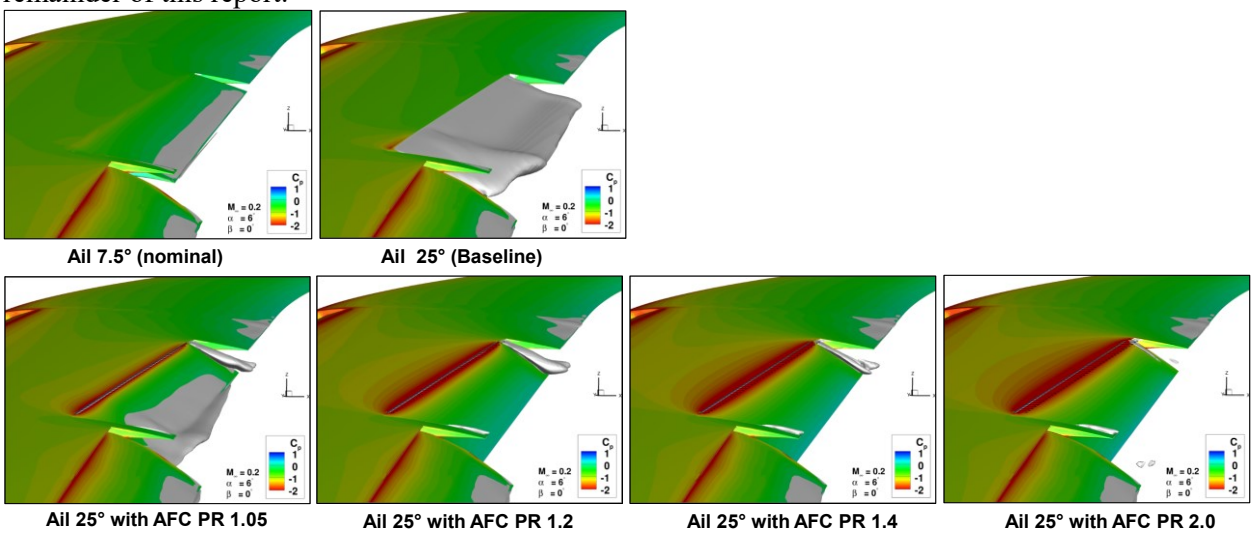

Figure 12 – Sensitivity to actuation level.

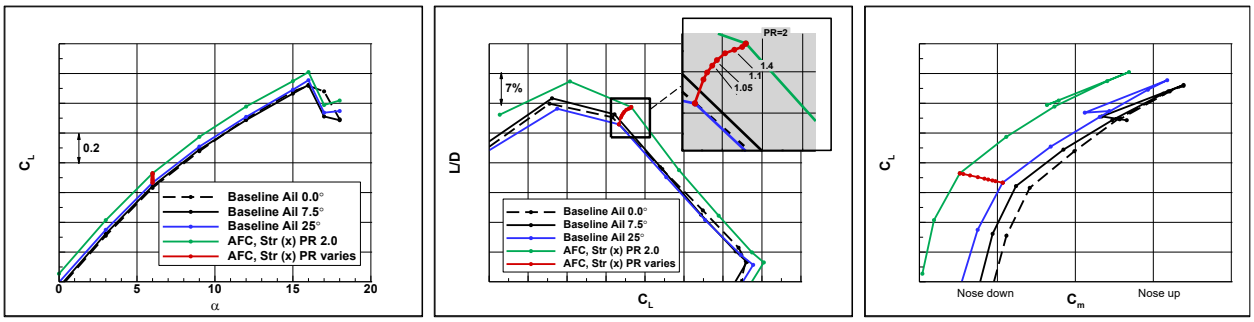

Figure 13 – Effect of actuation intensity on aerodynamic performance.

In the analysis of AFC systems, it is instructive to refer to the corresponding inviscid flow. The inviscid lift determines the theoretical upper limit of an airfoil to produce lift in the absence of viscous effects. Consequently, the inviscid lift level can be used as a yardstick for AFC efficiency. Throughout the following analysis, the inviscid lift is used to gauge the performance of the various actuation patterns.

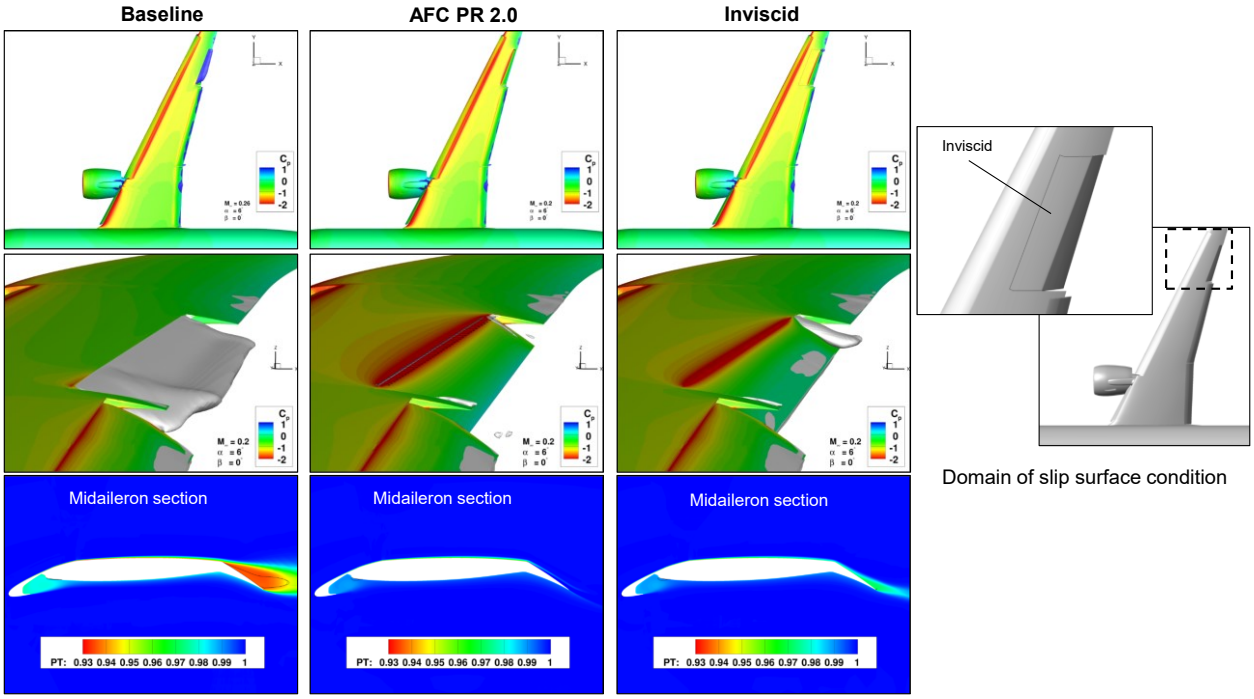

Figure 14 – Pseudo-inviscid flow is used to gauge the efficiency of flow control.

Since here the flow control is applied locally, a special modeling procedure has to be devised to establish a comparable inviscid limit. This pseudo-inviscid model uses a slip surface condition on the upper surface of the aileron and on portion of the wing ahead of the hinge line. This strategy is illustrated in Figure 14, together with the flow fields obtained for the 25° aileron. It is noted that the inviscid solution results in a very small separation pocket, likely due to the numerical dissipation. Based on these solutions, the actuated flow with PR=2 produces a flow that is more effective than the inviscid case. The jet is strong enough to suppress separation and provide added circulation beyond the inviscid level. This is also evident from the wing load distributions and the sectional pressure plots in Figure 15.

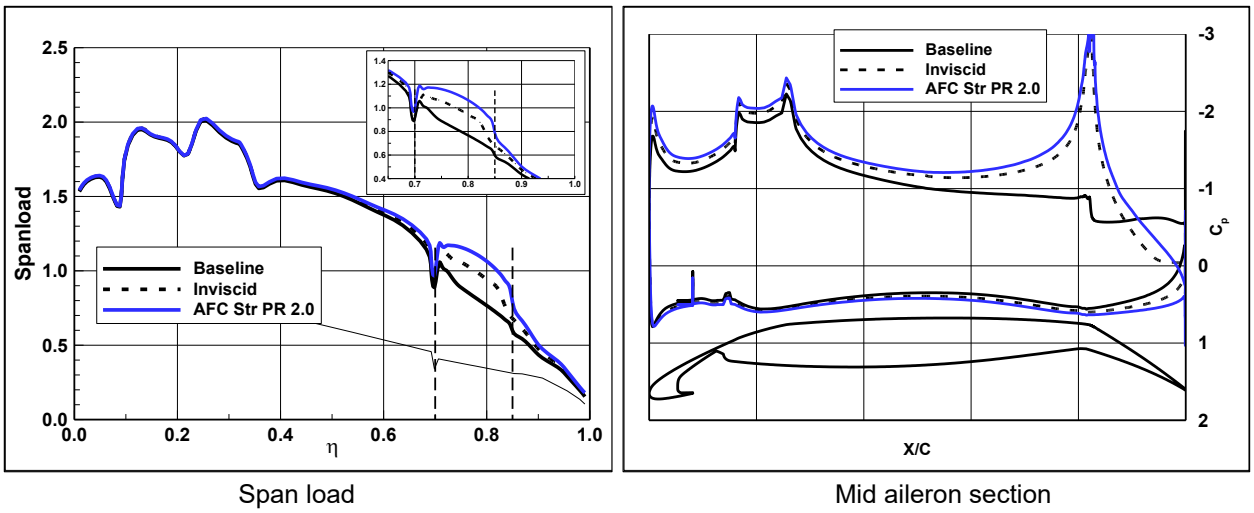

Figure 15 – Aerodynamic characteristics of the wing for the pseudo-inviscid and the actuated PR=2 case.

The aerodynamic performance as a function of actuation mass flow coefficient C_q is shown in Figure 16. The lift is obtained at α=6° and the percentage increment in L/D due to AFC is taken relative to the corresponding baseline C_L. The baseline (unactuated) aileron 25° results in higher lift relative to the nominal aileron, but it comes with higher drag, as indicated by the drop of about 1% in L/D. However, flow control makes up for this shortfall with very small pressure ratio. As input pressure becomes larger, the incremental lift and L/D become substantial. Using the inviscid level as a measure of efficiency, it becomes apparent that PR can be dialed down for more efficient actuation. Flow control is very effective in reducing viscous effects and suppressing separation up to PR of about 1.2, and it becomes less efficient at higher pressure where actuation becomes a mechanism of circulation control. It is pointed out that the C_q is small since it is being referenced to the wing area and it represents actuation input for both ailerons. Also, C_q of 0.00018 corresponds to the mass flow that could potentially be supplied by an APU (marked by the vertical dash line).

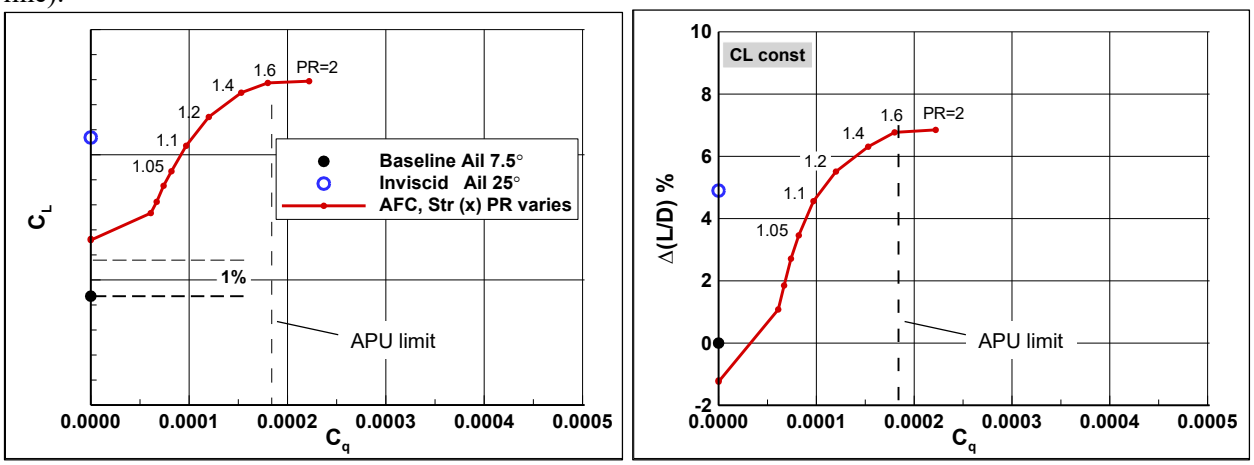

Figure 16 – Aerodynamic performance as function of actuation input, aileron 25°.

Several actuation patterns are considered next. The first is spanwise actuation because it relates to an important integration aspect. The space available for installing the AFC system in the aileron and the neighboring area is limited. It is therefore instructive to evaluate the effect of AFC relative to span placement. Figures 17 and 18 show the effect of actuation of PR=2 on the inboard (IB) half span vs the outboard (OB) half span segments of the aileron. Results indicate that the actuation has a local effect on the separation pattern and the aerodynamic gains in terms of L/D are quite similar, with a slight advantage to

the inboard actuation. This is likely due to the spanwise effect on swept wings where perturbations propagate outboard toward the wingtip as can be inferred from the span load distributions. Both of these actuation patterns are less efficient than the entire span actuation (Figure 18). It is noted that there are implications to structural integrity of the aileron and its mechanical actuators particularly under the added load from different actuation patterns.

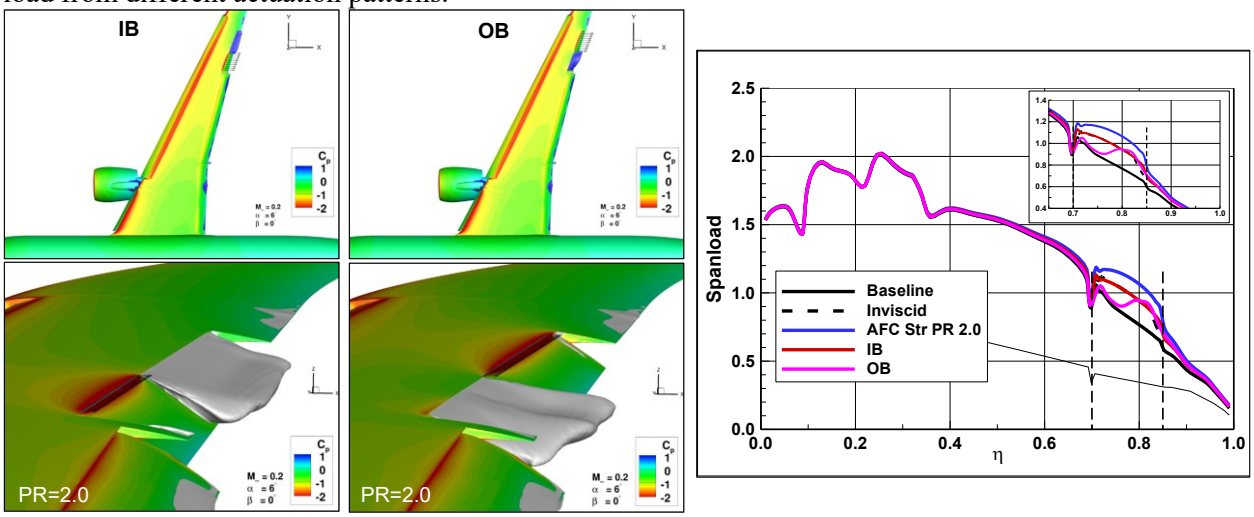

Figure 17 – Inboard versus outboard aileron actuation, aileron 25°: flow field.

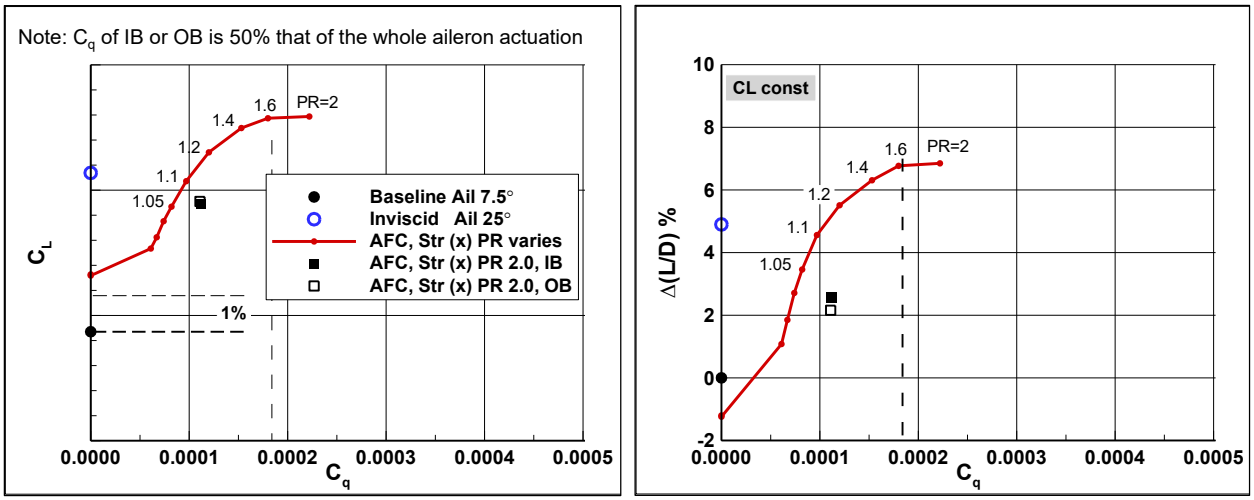

Figure 18 – Inboard versus outboard aileron actuation, aileron 25°: aerodynamic performance.

Jet angle to local surface is investigated next in Figures 19 and 20. The jet angle is measured relative to the x coordinate, so in the previous actuation modes, the angle is 0°. Jet angles of +10° and -10° have been analyzed, which correspond to 22° and 2° off the local surface, respectively. In this analysis using a surface boundary condition that is applied on a constant strip width, when the jet angle varies, the mass flow changes according to $\dot{m} = \rho \mathbf{U} \cdot \mathbf{A}$, where **U** and **A** are the velocity and area vectors, respectively. For example, when the jet is perpendicular to the strip, $\dot{m}$ is maximum. As the jet becomes tangent to the surface, $\dot{m}$ becomes very small. This is illustrated in Figure 19, which shows the flow fields in the midaileron section in terms of total pressure and Mach number. Figure 20 shows that the jet effectiveness increases with smaller jet-to-surface angles. When the jet angle is large, low velocity jets are ineffective, whereas low angle jets affect the flow even at very low pressure ratios.

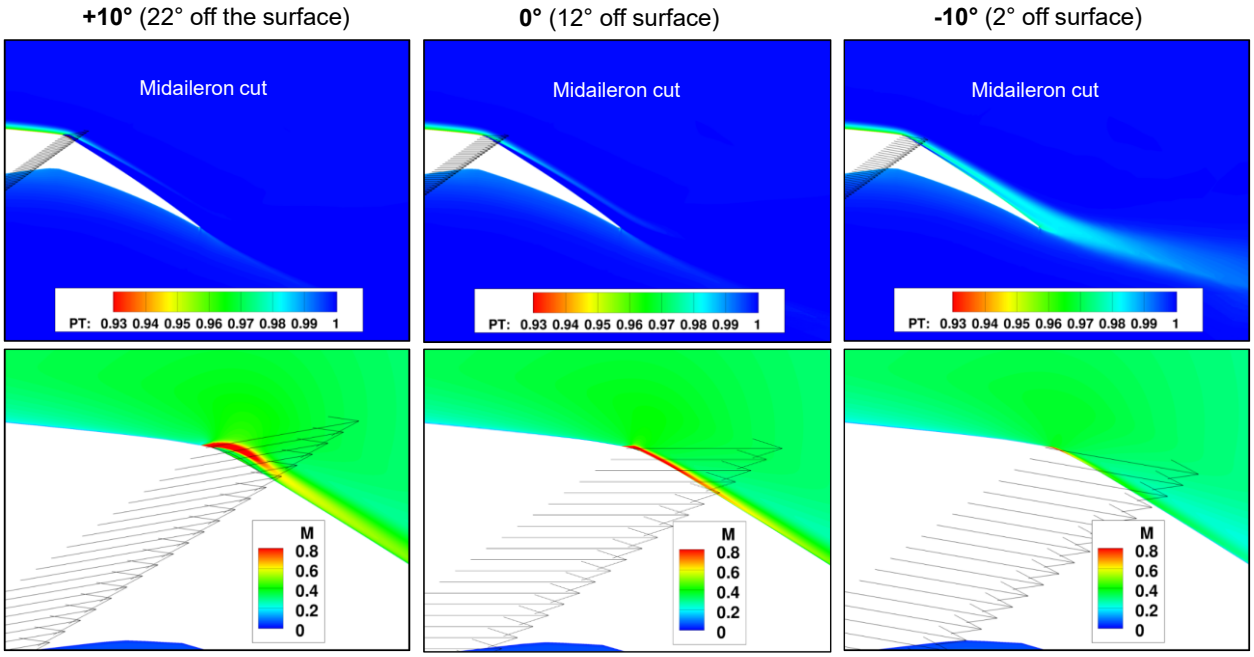

Figure 19 – Effect of jet ejection angle, aileron 25°: flow field.

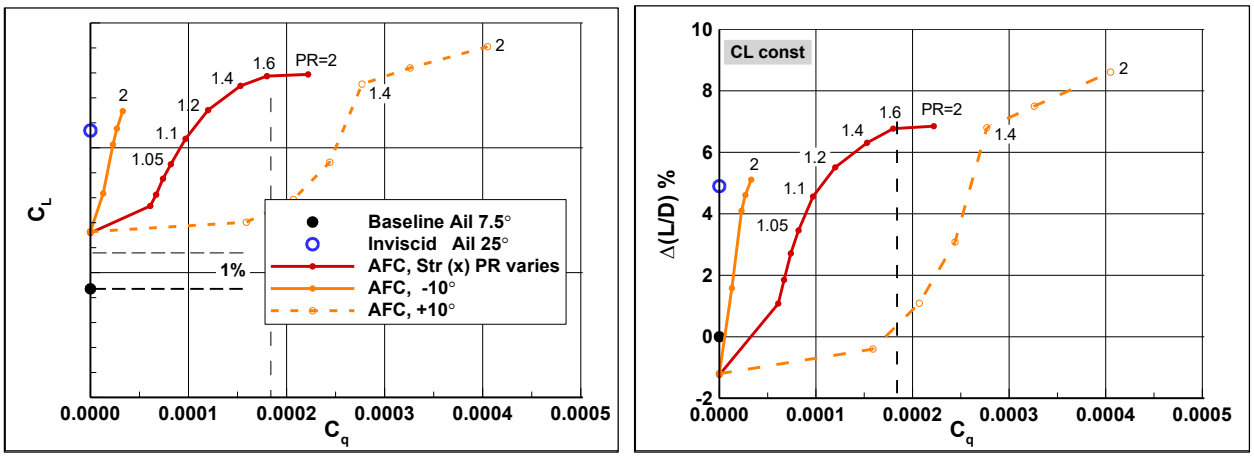

Figure 20 – Effect of jet ejection angle, aileron 25°: aerodynamic performance.

Segmented AFC application is analyzed in Figure 21 for PR=2 and -10° angle, based on the aforementioned convention. There are 11 discrete jets of the same width, spread at equal distance apart across the aileron span. This actuation exhibits an alternating pattern of separated and attached regions, which are coincident with the unactuated and actuated span segments, respectively. The discrete jets result in a wavy wing load distribution. The segmented AFC pattern in not as efficient as the full span actuation.

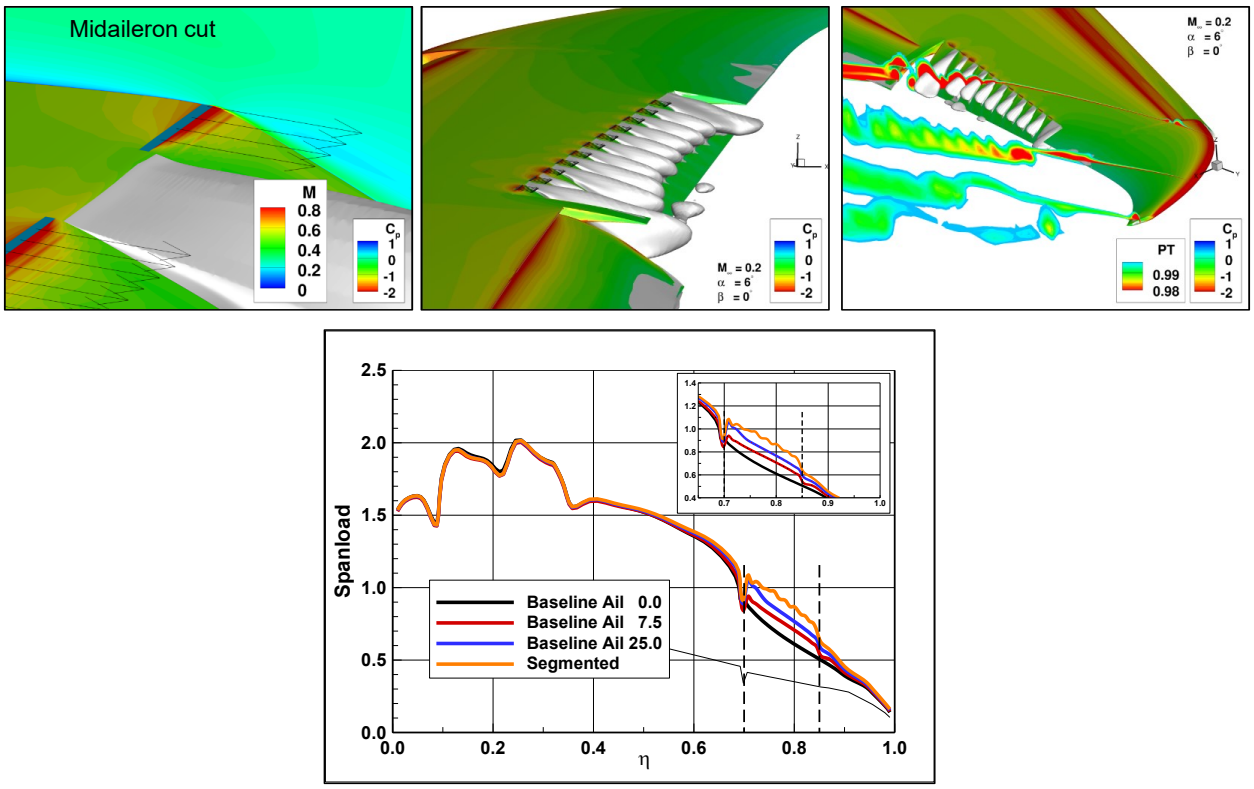

Figure 21 – Segmented AFC application, aileron 25°, PR=2, jet angle -10°.

4.1.3 Blowing Nozzle

After getting insight into the effects of actuation parameters and placement using the simplified modeling approach in Section 4.1.2, we now consider a realistic implementation of flow control. It consists of a continuous nozzle that runs the full span of the aileron. The long nozzle system is described in the inset in Figure 22. It consists of a two-dimensional convergent-divergent (CD) section in the vertical plane (xz) whose exit section forms a long slot along the aileron. The throat to inlet area ratio, A_{th}/A_{in} is 0.4. The inlet consists of a constant area duct, which is connected to a convergent duct section. The diffuser is long enough to ensure that its half angle is smaller than 15° to prevent the flow from separating. The nozzle cross-section is identical along the span. The grid system consists of 85 million points. The solution for PR=2 is also shown in Figure 22. At this pressure ratio, the CD nozzle becomes choked. The flow accelerates in the diffuser and the jet is ejected at supersonic velocity over the aileron. At this condition, the blanket of high speed flow helps energize the viscous layer and prevent flow separation over the entire aileron.

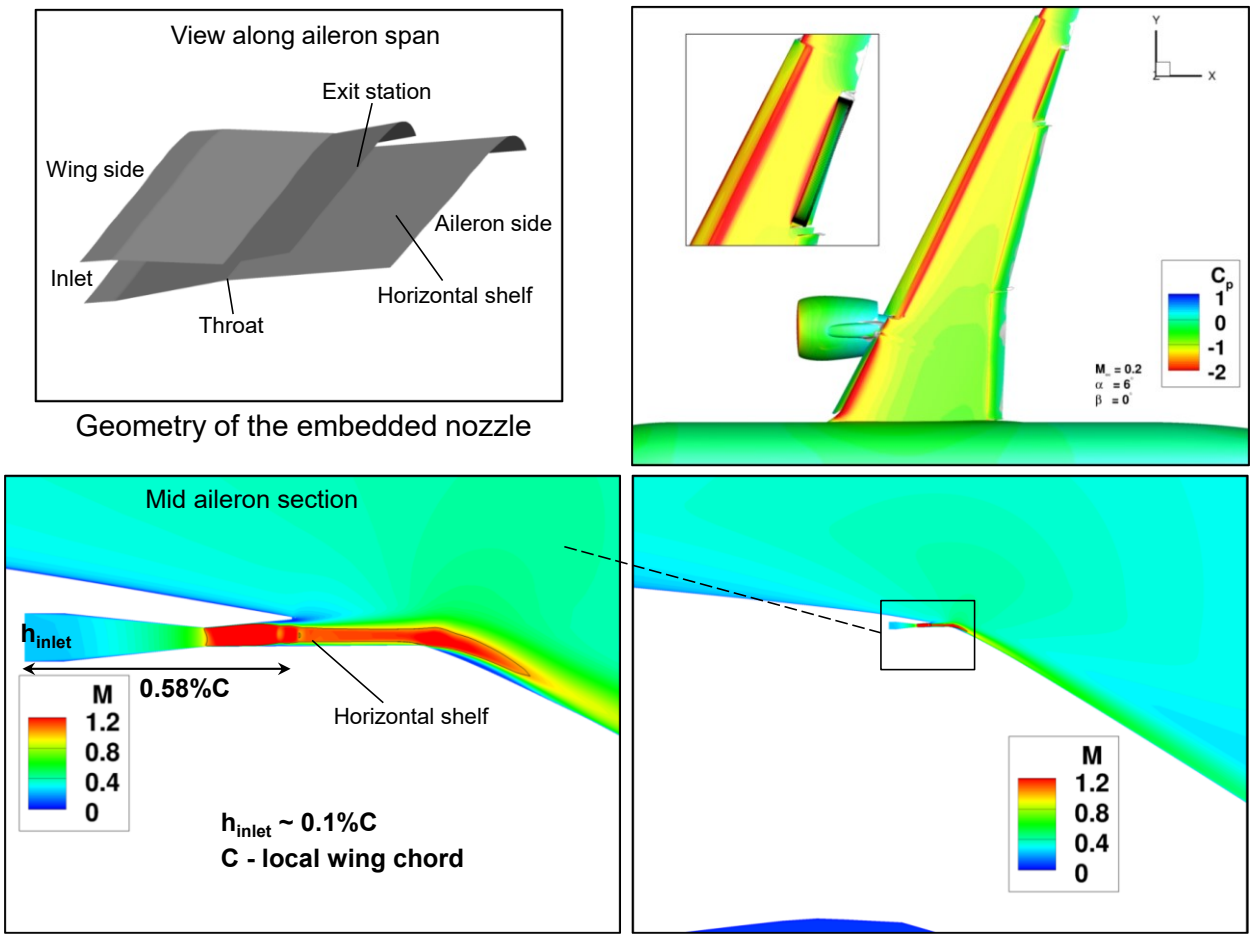

Figure 22 – Blowing convergent-divergent nozzle, aileron 25°, PR=2.

It is interesting to see the differences in the results obtained with the surface blowing and the CD nozzle. The cross-sectional Mach number contours indicate that at some distance from the outer mold lines the flow fields look very similar for both pressure ratios. The more realistic representation of the jet with the CD nozzle shows a higher efficiency in terms of L/D across the pressure range.

Figures 23 and 24 show the effect of input pressure ratio. Here the black lines denote sonic conditions. As PR increases, the nozzle becomes choked and supersonic velocity is attained in the diffuser and beyond. The jet expands as it reaches the aileron surface and accelerates as it emerges over the upper surface of the aileron.

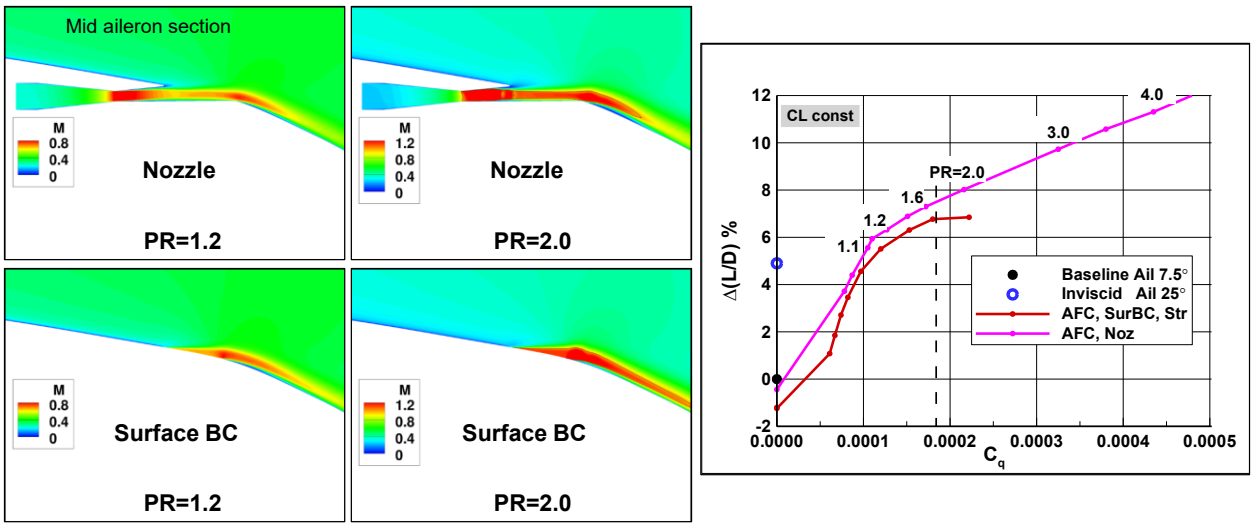

Figure 23 – Solution comparison between the surface boundary condition and the blowing nozzle, aileron 25°.

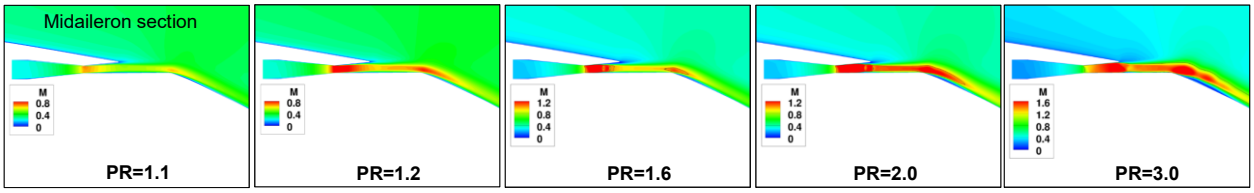

Figure 24 – Effect of pressure ratio of the blowing nozzle, aileron 25°.

Driven by integration issues such as space availability and breach of the wing and aileron outer mold line (OML), an assessment of nozzle size was conducted. The size of the original nozzle has been reduced by a factor of two, to produce two sequentially smaller nozzles having identical area ratios. Denoting the original nozzle as nozzle 100%, the smaller nozzles are dubbed nozzle 50% and nozzle 25%. Nozzle layouts and sample solutions obtained for PR=2 are presented in Figure 25. The nozzles span the entire aileron and their exit station is at the same streamwise location. All of the three nozzles are effective in reducing flow separation. The flow fields within the nozzle are very similar since the nozzle area ratio is the same. Figure 26 shows the relative efficiency of the different sized nozzles. Although the smaller nozzles are more efficient, they require higher PR. Ultimately the AFC integration and the available air sources (PR, $\dot{m}$) will drive the selection of the nozzle size.

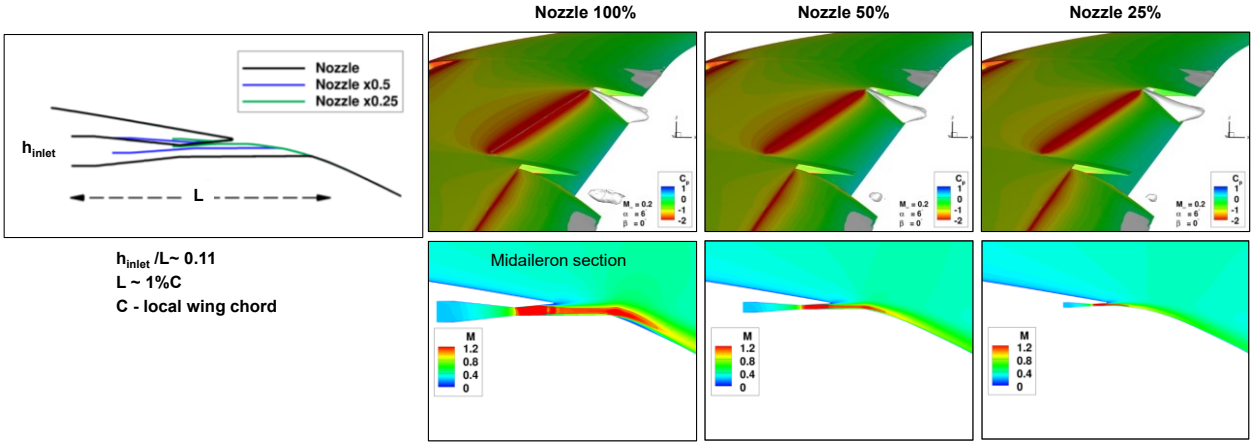

Figure 25 – Effect of nozzle size on flow field, aileron 25°, PR=2.

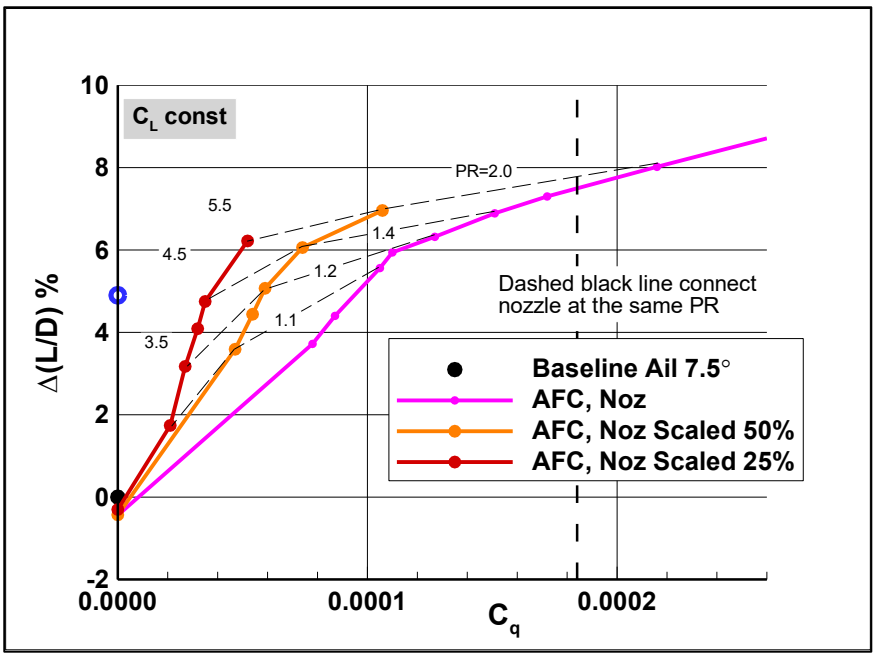

Figure 26 – Effect of nozzle size on aerodynamic performance, aileron 25°.

4.1.4 Discrete Blowing Nozzles

Systems of discrete actuators have also been considered for the aileron application. An array of actuators in the form of CD nozzles, where the sectional geometry is defined in the horizontal plane xz. The geometry of the actuators is identical and of the same size, with throat to inlet area ratio of 0.4, identical to that of the blowing nozzle. The nozzles are spaced at equal distances along the aileron at the same location as the blowing nozzle. The center lines of the nozzles are perpendicular to the hinge line.

Two layouts were considered for the computational assessment of the discrete nozzles. One consists of 78 nozzles with an aspect ratio of 2 at the throat section of each nozzle, where the shorter dimension is vertical. The other set uses an array of 63 nozzles with aspect ratio of 3. The two layouts are denoted AR2 and AR3. The throat area A_{th} of each nozzle is the same in both layouts. Therefore, the ratio of total throat area between AR2 and AR3 is 1.24. These arrangements are described in Figure 27, where the blowing nozzle 100% from Section 4.1.3 is included for reference. Note that the exit stations of the nozzles lie on a backward facing step. The step size is identical but nozzle height is different. Each of the grid systems of these configurations consists of about 86 million points.

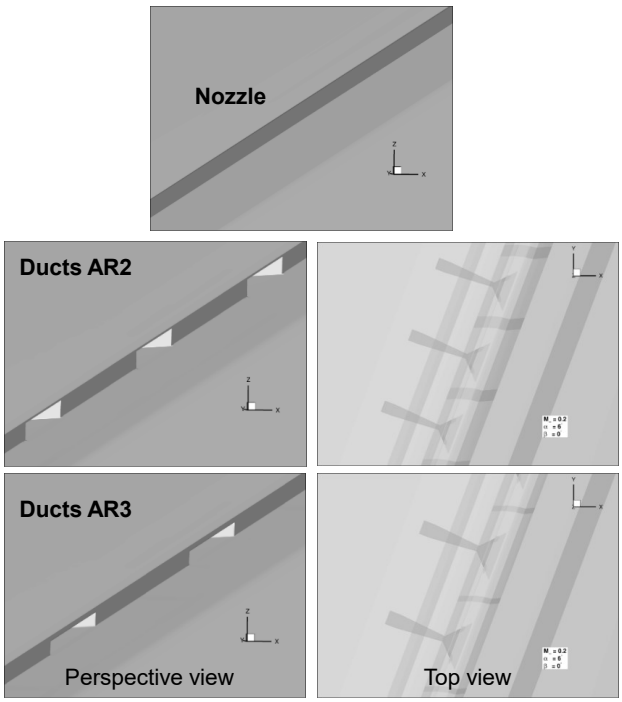

AR (at throat)	# nozzles per aileron	A_{th} per nozzle	A_{th} total
2	78	A_{th}	$78 \cdot A_{th}$
3	63	A_{th}	$63 \cdot A_{th}$

Figure 27 – Layouts of the discrete nozzles.

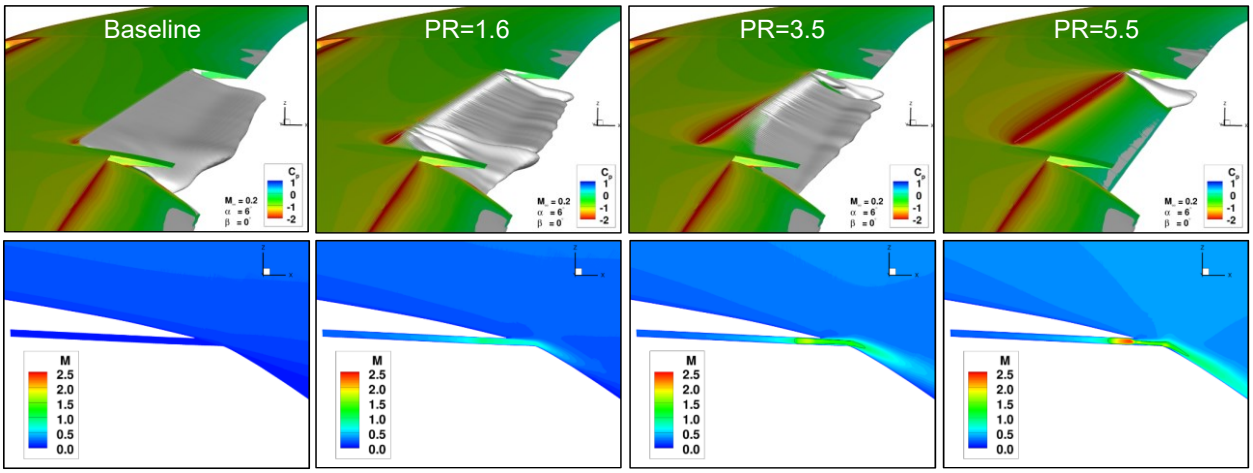

Figure 28 – Flow fields of the discrete nozzles AR2, aileron 25°.

Figure 28 shows the flow fields obtained for the AR2 layout at different input pressure. Cross-sectional cuts through one of the actuators are also included. As PR increases, the actuators become choked and the supersonic jets start affecting the separation bubble. The AR2 pattern is very efficient, but because the total throat area is very small, it requires high PR. Even at the highest PR of 5.5 a sliver of separated flow still exists at the trailing edge of the aileron. Performance comparison of AR2 and AR3 and the blowing nozzle is presented in Figure 29. Both actuation layouts are effective, but from the separation patterns in the

PR=5.5 cases, it appears that AR2 has an advantage, likely due to its larger area. The aerodynamic performance of the family of blowing nozzles and the discrete nozzles are summarized in Figure 30 as functions of C_q and the momentum coefficient, C_μ (integrated at the throat section). Interestingly, the various curves are fairly clustered in the C_μ plot, reinforcing the notion that the momentum coefficient is the relevant AFC parameter for the kind of flows considered here. Clearly both nozzle families are potential candidates of actuators as they require mass flows well within the capability of an APU or another equivalent source for producing meaningful L/D gains. Irrespective of the type of nozzles, better efficiency is achieved with smaller area actuators, but they require higher PR. This type of trades is a central element in the design of a practical AFC system. Figure 31 summarizes the major trade factors for the type of nozzle candidates used in this study. Aspects of system integration that considered actuator sizing, the pairing up with potential sources, as well as other factors, are addressed in the integration study (final report document #3 [3]).

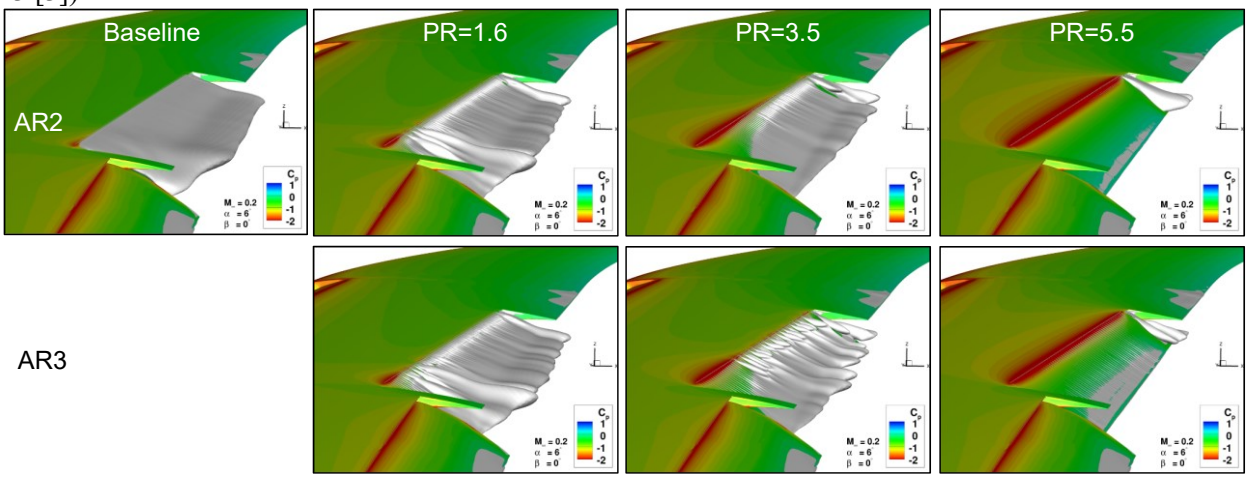

Figure 29 – Flow fields for the discrete nozzle layouts, aileron 25°.

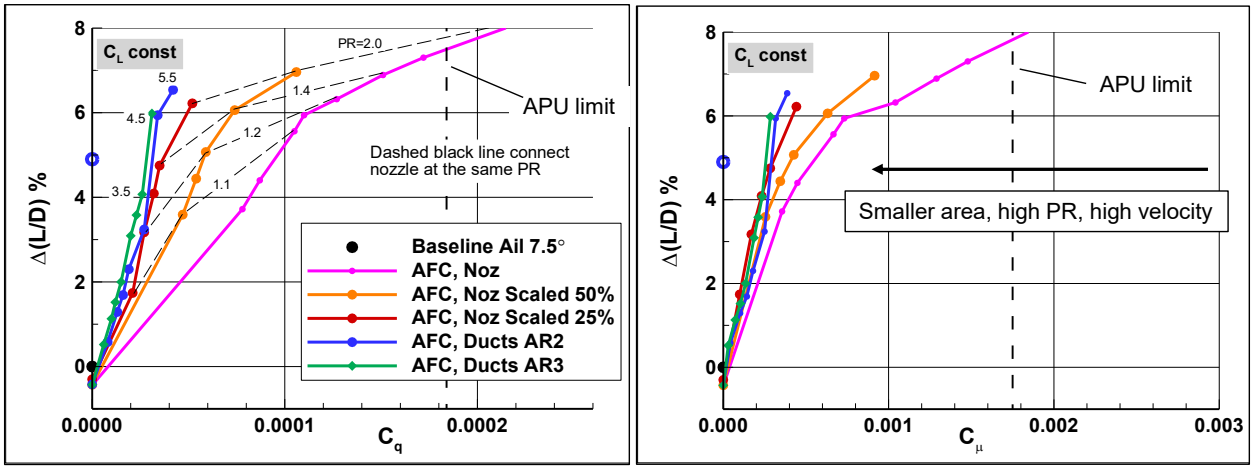

Figure 30 – Aerodynamic performance of the blowing nozzles and the discrete nozzles, aileron 25°.

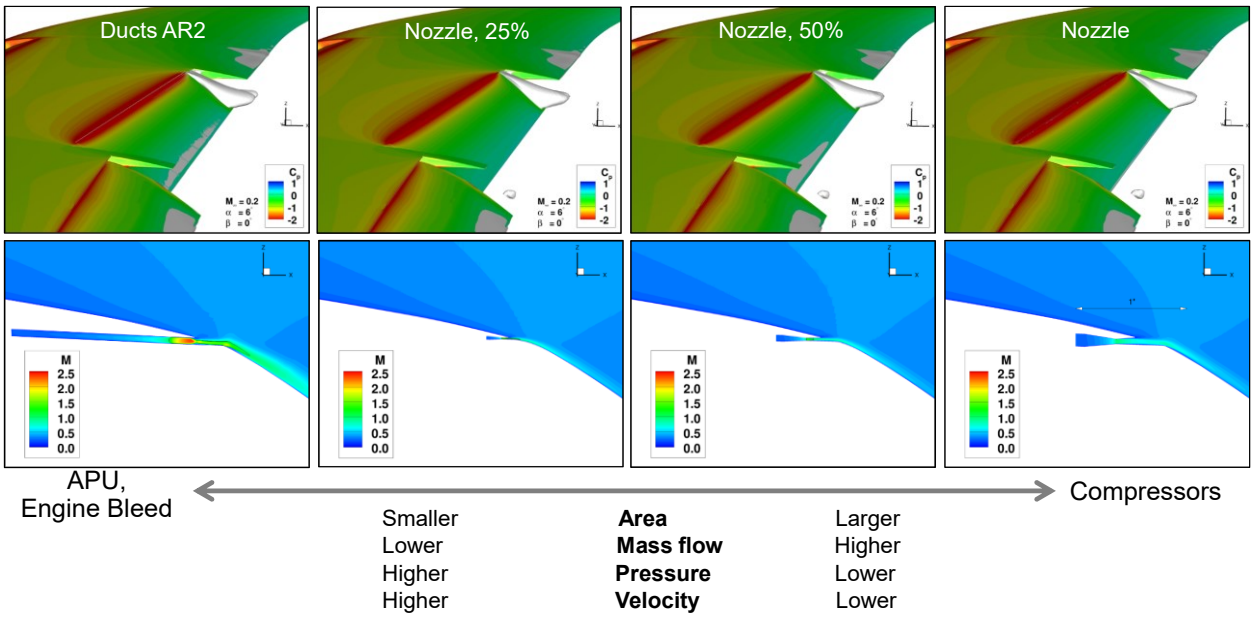

Figure 31 – Trade factors that will impact the practical design of AFC.

The manner in which integration factors and power sources might determine the type of actuation is illustrated in Figure 32. It presents the results of some of the nozzles discussed earlier in terms of the gain in L/D and C_q required for actuation as functions of PR. For example, if the design target is an increase of 6% in L/D, two optional layouts might be considered. One scenario denoted A might employ a system of discrete nozzles AR2 with a high PR source of 4.5, which requires limited mass flow. The option marked 'B' uses the blowing nozzle 50% with PR=1.4. Scenario C represents a low-PR, low-C_q system with 1.3 and 0.00003, respectively, which is based on nozzle 25% and attains a 4% improvement in L/D. Finally, it is pointed out that although all these scenarios are within the limits of an APU in terms of mass flow, the maximum pressure available at the inlet of the actuators isn't known. That will depend on the distance from the source to the actuators, the plumbing system and other factors. These considerations will be discussed in the integration study (final report document #3 [3]).

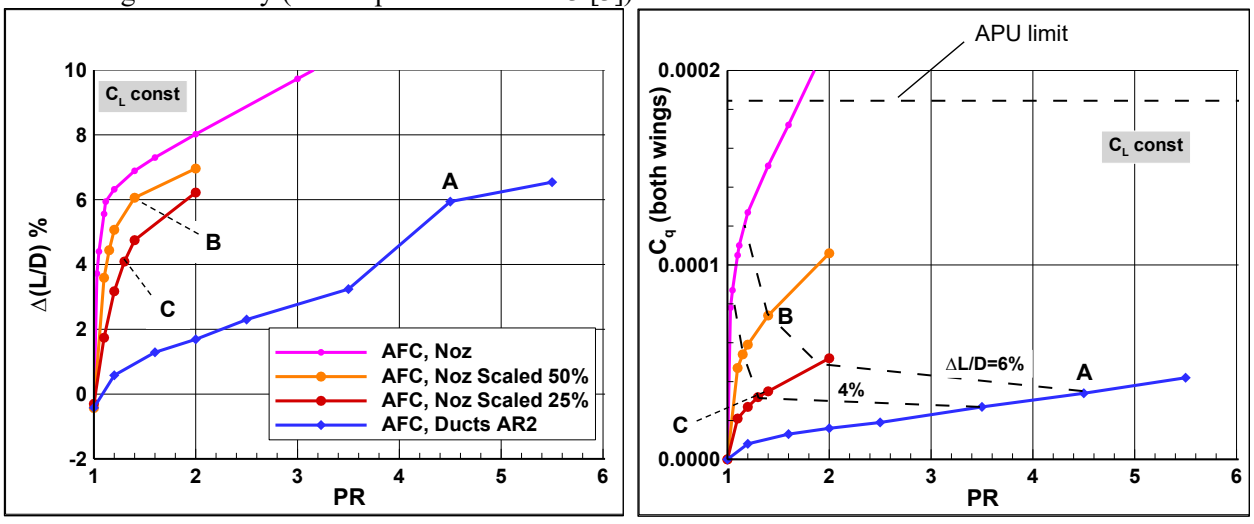

Figure 32 – Trade factors for the various nozzles configurations.

4.1.5 Actuator Efficiency

It is instructive to compare the efficiency of the actuators with respect to their internal flow. Gas dynamics (GD) for the one-dimensional (1D) inviscid flow in nozzles having comparable area ratios is used to gauge effectiveness for a set of blowing nozzles considered in Sections 4.1.3 and 4.1.4. This will provide the flow properties of the comparable ideal flow with no losses. Figure 33 shows the actuation coefficients as a function of PR and the dash curves are the GD counterparts. Generally, all nozzles exhibit good quality flow for all nozzle shapes, especially at PRs higher than about 1.5. The difference between the theoretical and the computed flows are due to viscous losses and deviations from the 1D flow. The differences in efficiency of the nozzles are presented in Figure 34, using the ratios of the computed to the ideal GD values of the actuation parameters C_q and C_μ. This efficiency measure is plotted against the total area of the throat sections for each of the nozzle layouts. The computed trends indicate that the smaller the actuators, the bigger losses are. A plausible reason is that in small actuators the viscous boundary layers occupy a bigger fraction of the cross-sectional area.

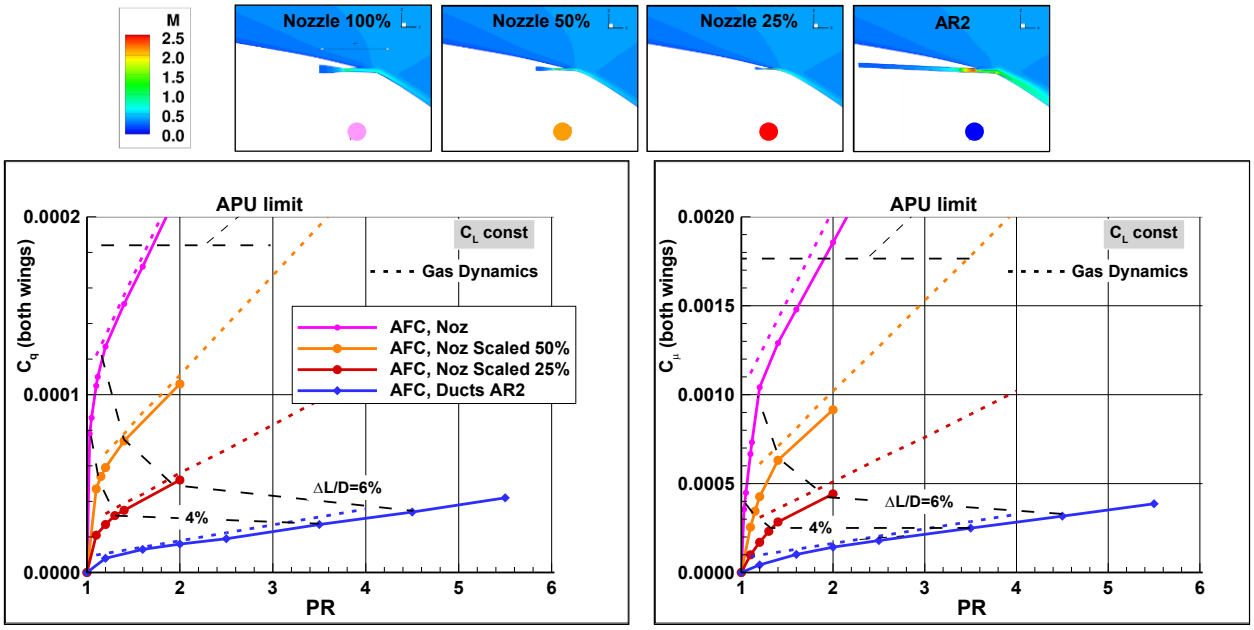

Figure 33 – Actuators efficiency for a set of blowing nozzles (Part I).

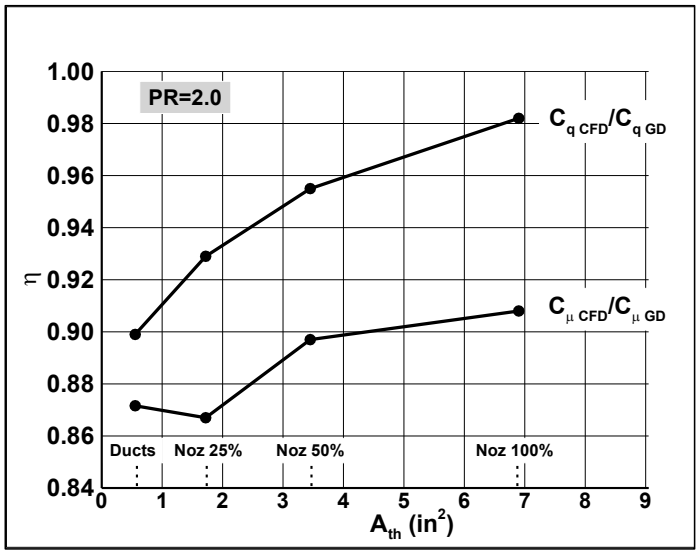

Figure 34 – Actuators efficiency for a set of blowing nozzles (Part II).

4.1.6 Aileron Deflections

The AFC simulations presented in the previous sections were performed for an aileron deflection of 25°. At this point, more practical aileron deflections will be considered as lower deflections are more consistent with the designs of current airplanes. Smaller deflections will result in lower loads, and hence more acceptable hinge moments for the aileron mechanical actuators to handle. Moreover, this might lead to reduced wing twist and bending moments, as well as lower trim drag.

For ease of integration, the analysis is performed for the medium size nozzle of 50%, the cross-section of which is shown in Figure 35 for the ailerons 16° and 25°. To the extent possible, the analyses use similar grids for the different aileron deflections in order to ensure minimal differences in discretization errors. The baseline flows for α=6° are shown in Figure 36. Mild separation forms along the trailing edge of the aileron at 7.5°. Flow separation develops over the entire aileron at 16° deflection, with a larger region of flow reversal at 25°. The size of the separation pockets for the set of aileron deflections is also evident from the cross-sectional wake contours of PT. The larger the deflection angle, the thicker and more intense the wake is. The flow fields obtained with actuation of PR=1.4 are illustrated in Figures 37 and 38 for the progressively higher aileron deflections. The aerodynamic characteristics of the wing for aileron 16° with nozzle 50% at PR=1.4 in Figure 39 shows the loading in the aileron wing area and outboard, with more elliptic-like load distribution. The L/D improvements from actuation at various PRs in Figure 40 show that when the aileron is largely separated, the flow control is very effective. The effectiveness drops at the lower deflections, where separation is relatively mild and by and large the AFC benefits are due to circulation control. These effects are also captured in Figure 41.

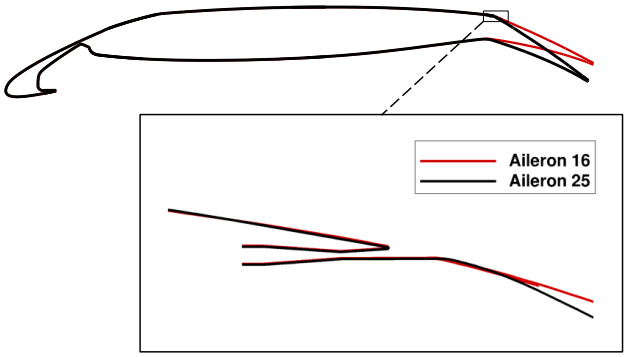

Figure 35 – Nozzle 50% embedded in the aileron 16° and 25°.

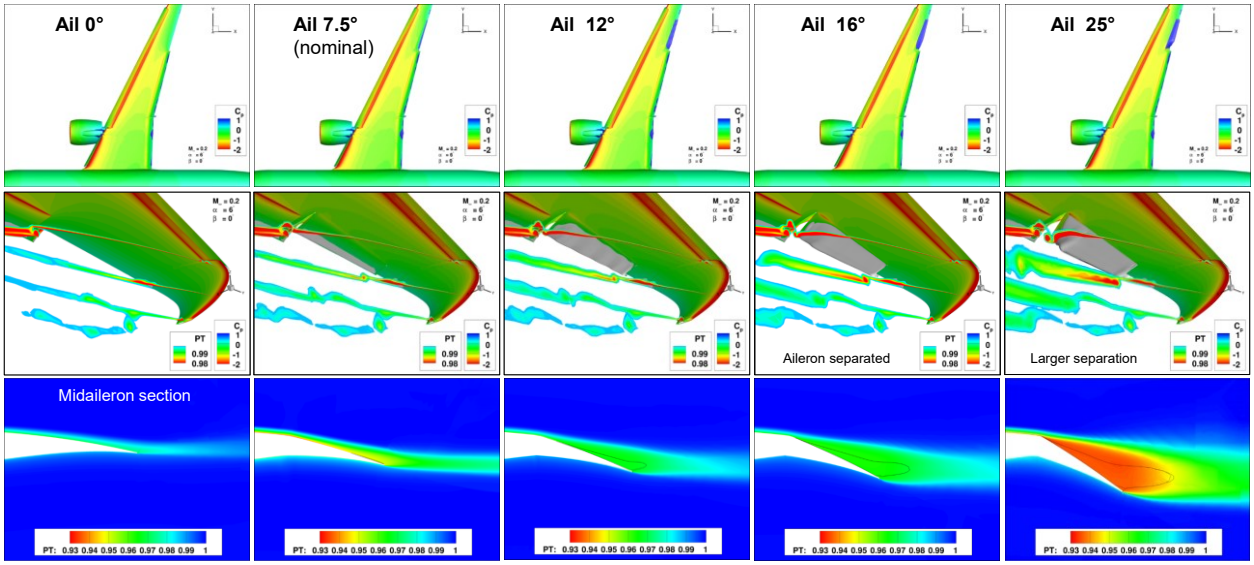

Figure 36 – Baseline flow fields for various aileron deflections, α=6°.

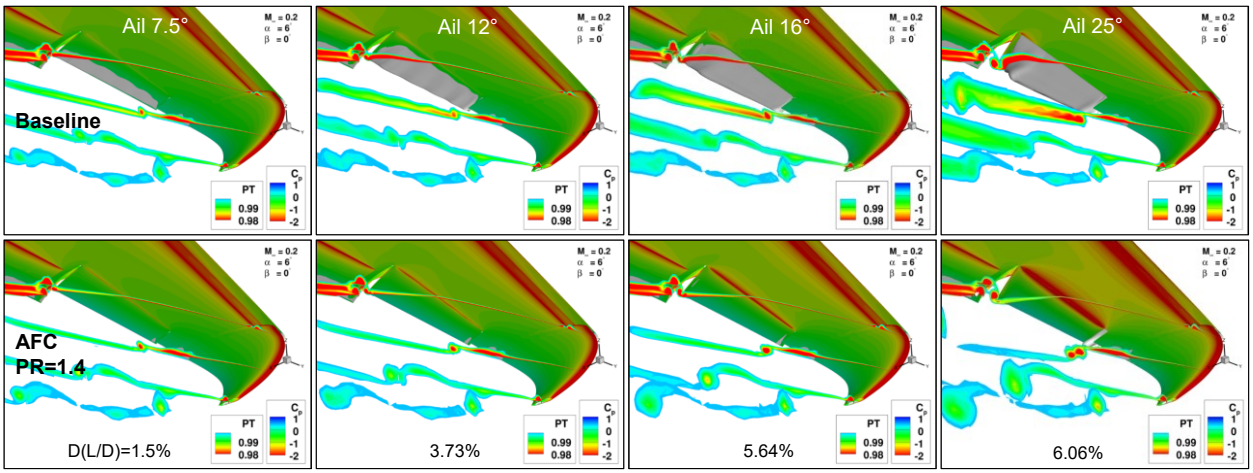

Figure 37 – Flow fields for the baseline and the actuated nozzle 50% at PR=1.4 for various aileron deflections.

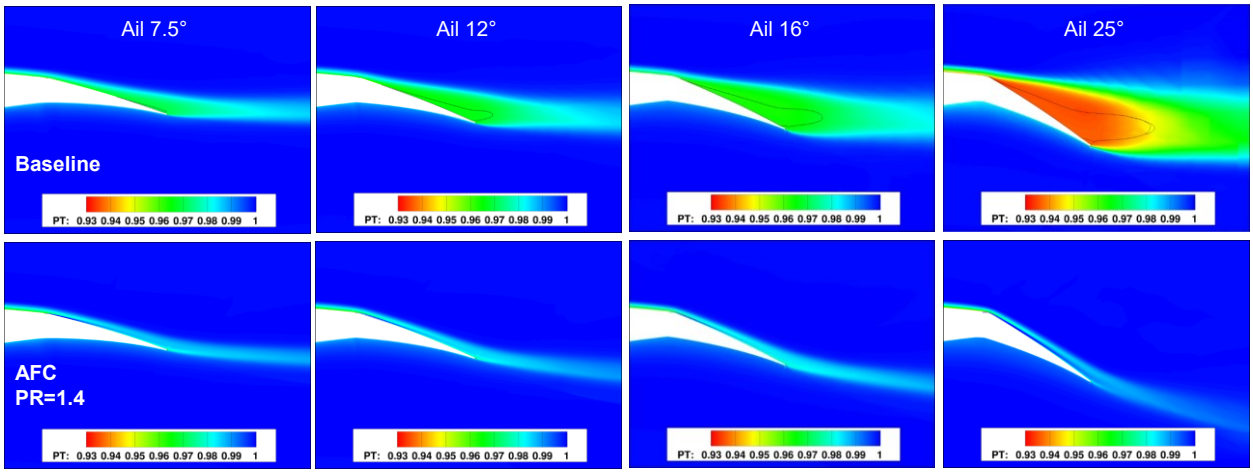

Figure 38 – Flow fields at the mid aileron section for the baseline and 50% actuated nozzle at PR=1.4 for various aileron deflections.

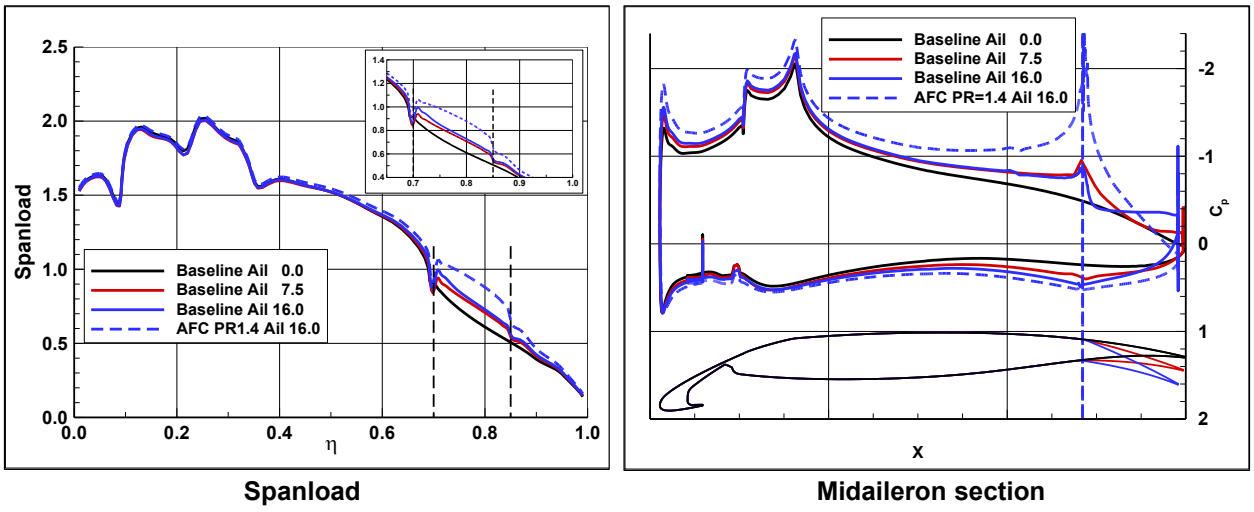

Figure 39 – Aerodynamic characteristics of the wing for aileron 16° with nozzle 50% at PR=1.4.

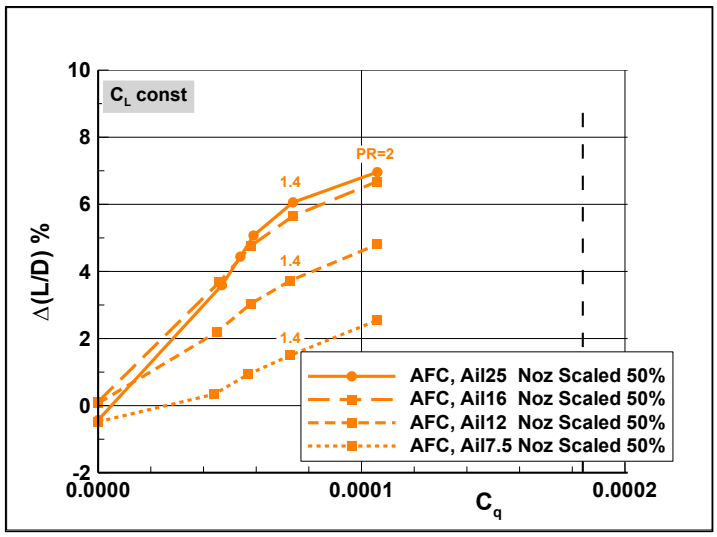

Figure 40 – AFC effectiveness drops at smaller aileron deflections.

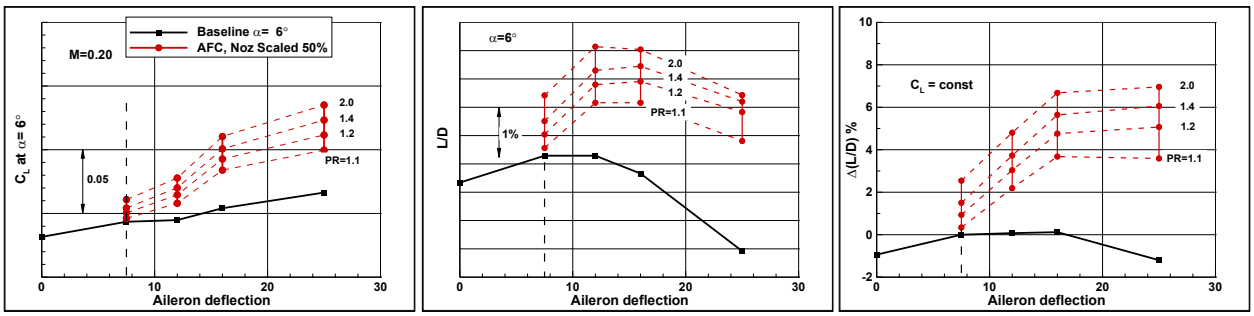

Figure 41 – Aerodynamic performance due to AFC using nozzle 50% as function of aileron deflection.

4.1.7 Reynolds Number Effects

All the simulations described in the previous sections were obtained for Re=6 million. Results of representative flight conditions for Re=25 million are presented next. Figures 42 and 43 show the Re effects on the performance of the baseline airplane at takeoff for the aileron deflections of 6°and 25°. The high Re produces higher lift and lower drag, consistent with the flow fields in the midaileron cuts. The viscous effects are less pronounced at high Re, clearly seen by the thinner boundary layer on the upper wing surface as it passes over the aileron. The effect of Re on AFC is captured in Figure 44. Commensurate with the smaller viscous effects at high Re, the AFC gains are also slightly smaller across the pressure range. Interestingly, the relative AFC effects depend on PR. Low PR is more effective at high Re because of the thinner boundary layer, as shown in the flow fields in Figure 45. That is because it takes very little momentum from AFC to affect the flow when the viscous effects are milder. At PR of about 1.2, the situation reverses, whereby larger momentum is more impactful for the low Re case when the viscous effects are greater. This trend inversion is shown in Figure 46. The fact that low PR is more effective at low Re at flight conditions might be exploited with a localized compressor-based system, per the discussion in Section 4.1.4. The effects of Re on AFC for the set of aileron deflections are presented in Figure 47.

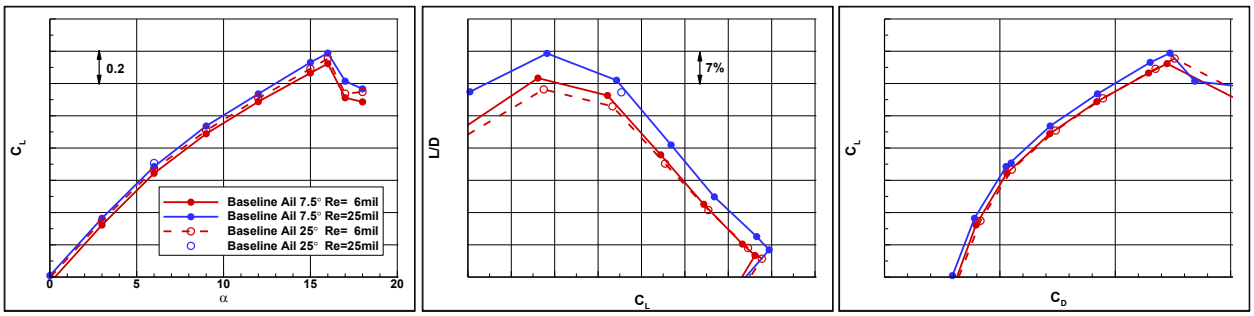

Figure 42 – Reynolds number effects on the performance of the baseline airplane at takeoff for the Ail7.5 and Ail25.

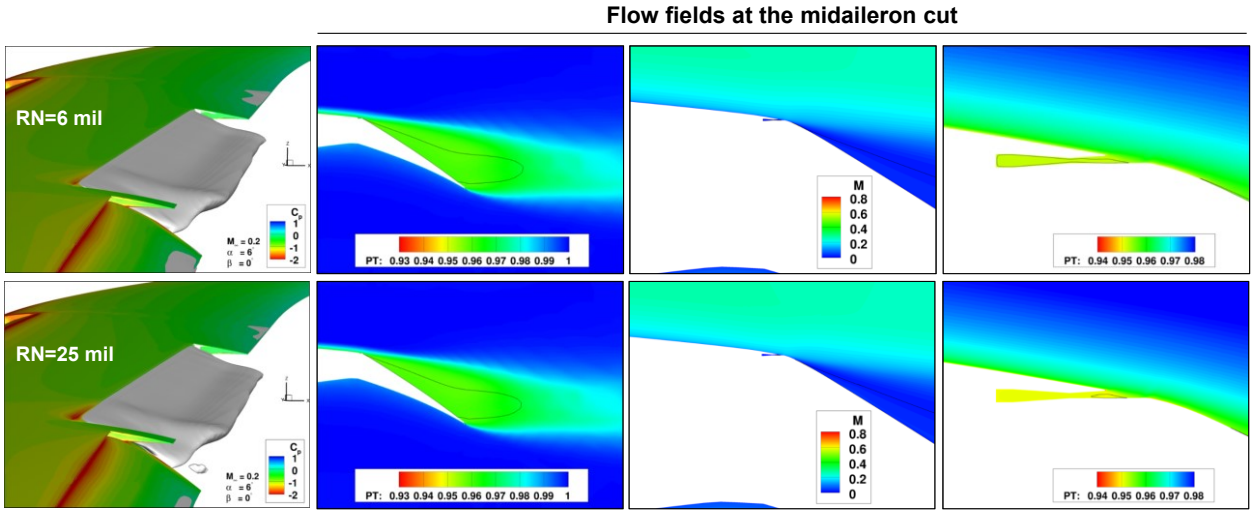

Figure 43 – Reynolds number effects on the flow fields of the baseline airplane at takeoff for Ail25.

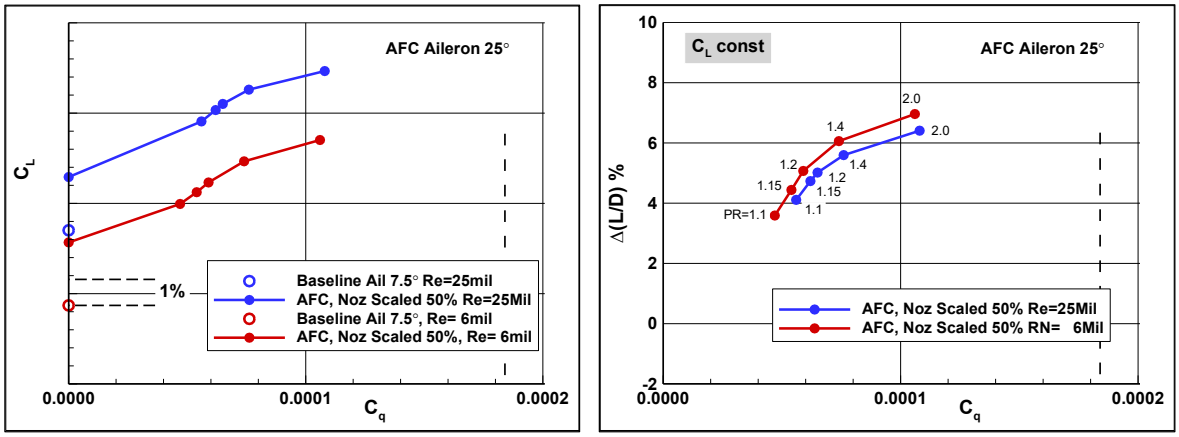

Figure 44 – Effects of Reynolds number on AFC at takeoff for Ail25.

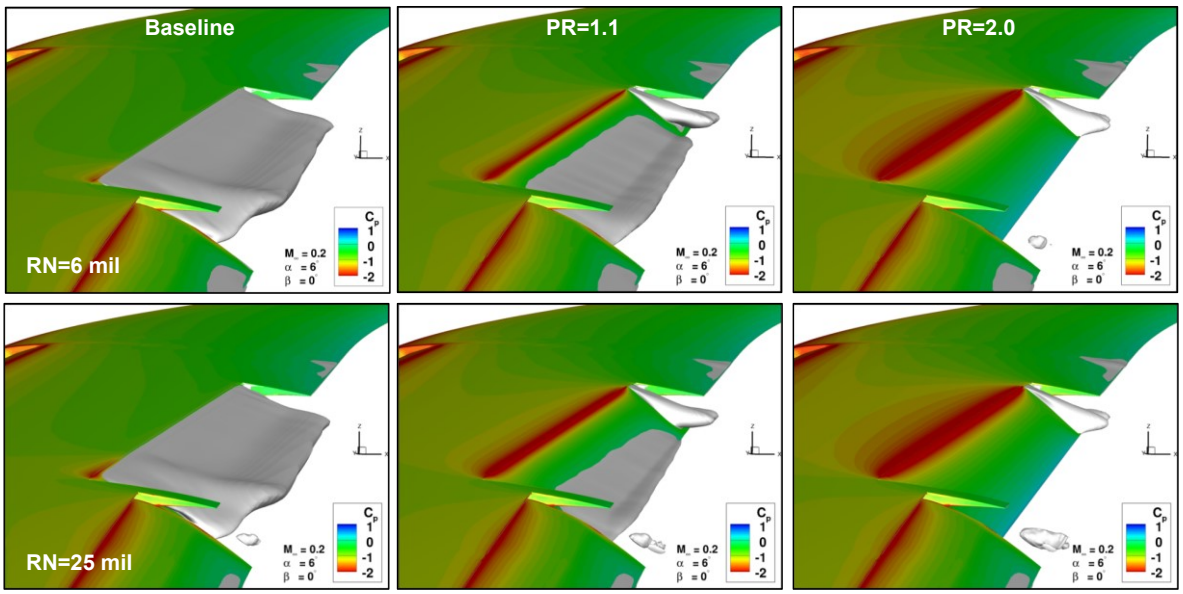

Figure 45 – Effects of Reynolds number on the flow fields with AFC at takeoff for Ail25, α=6°.

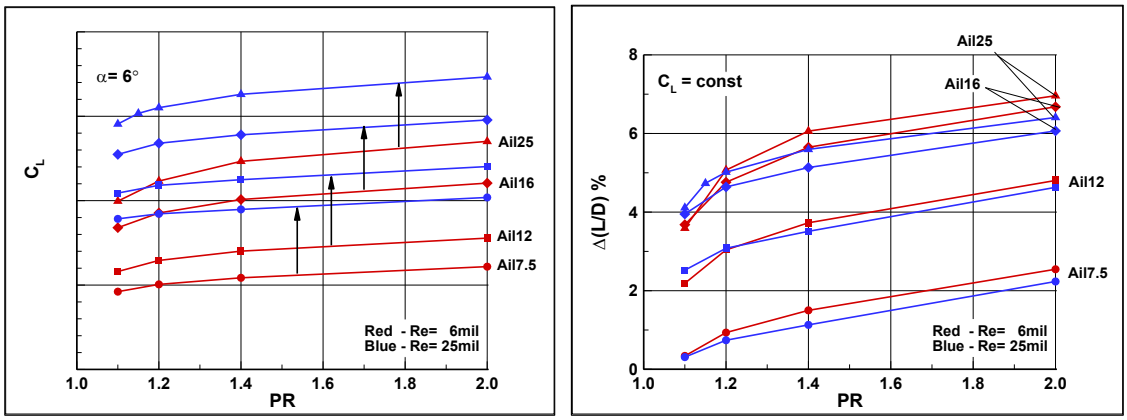

Figure 46 – Effects of Reynolds number on AFC as function of PR at takeoff for Ail25 aileron deflection.

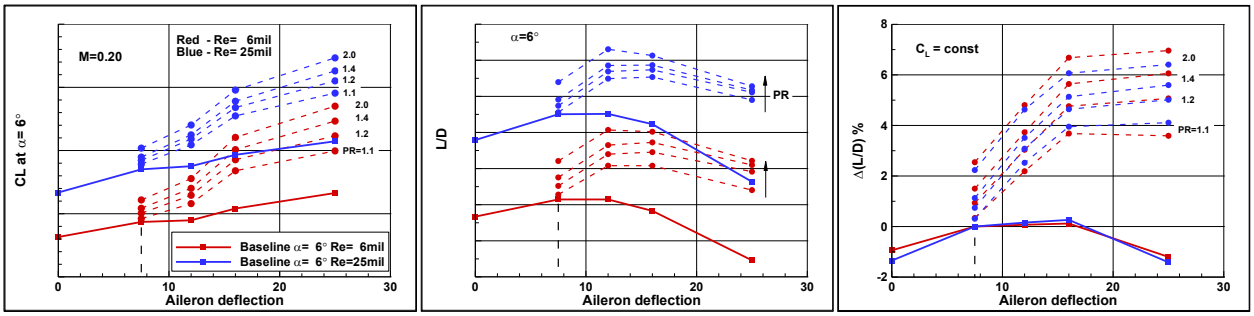

Figure 47 – Effects of Reynolds number on AFC at takeoff for various aileron deflections.

4.1.8 Landing Conditions

Landing conditions are evaluated for a typical landing configuration with slotted slats and landing flap deflections. The nominal aileron deflection is 0°. The freestream Mach number is M=0.20 and Re=6 million. The results are shown in Figures 48 and 49 where flow control is applied to the aileron at 16° using nozzle 50% at PR=2. The results illustrate similar aerodynamic effects as those obtained for the takeoff condition.

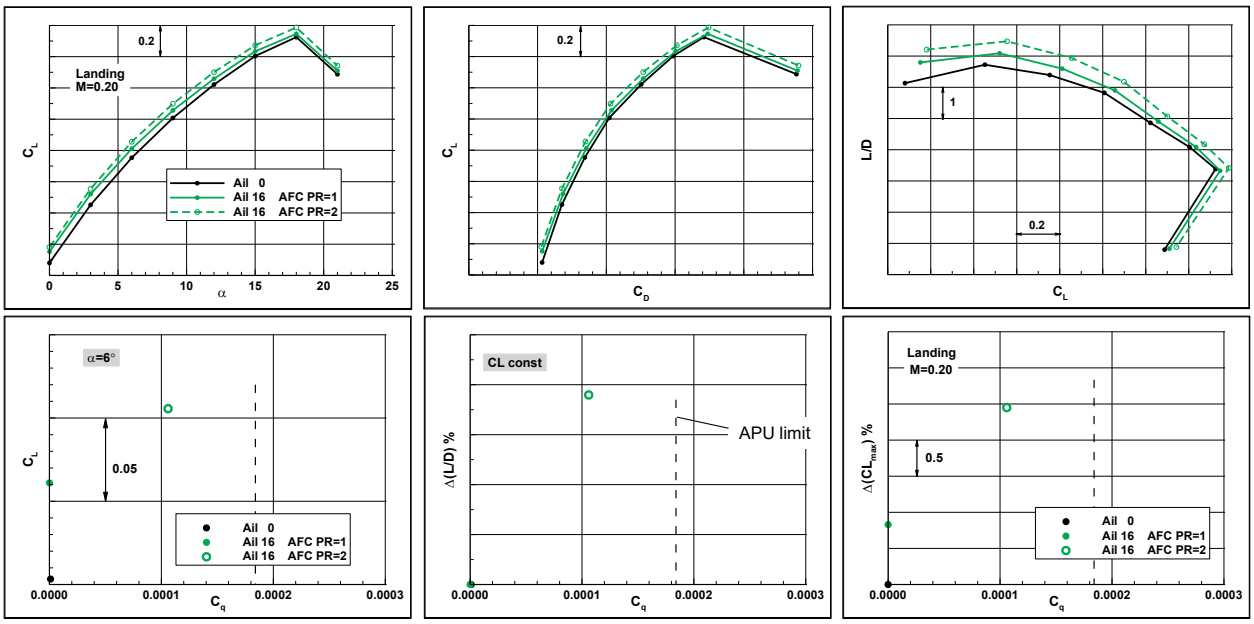

Figure 48 – Landing conditions: Aerodynamic performance due to AFC using nozzle 50% for Ail16.

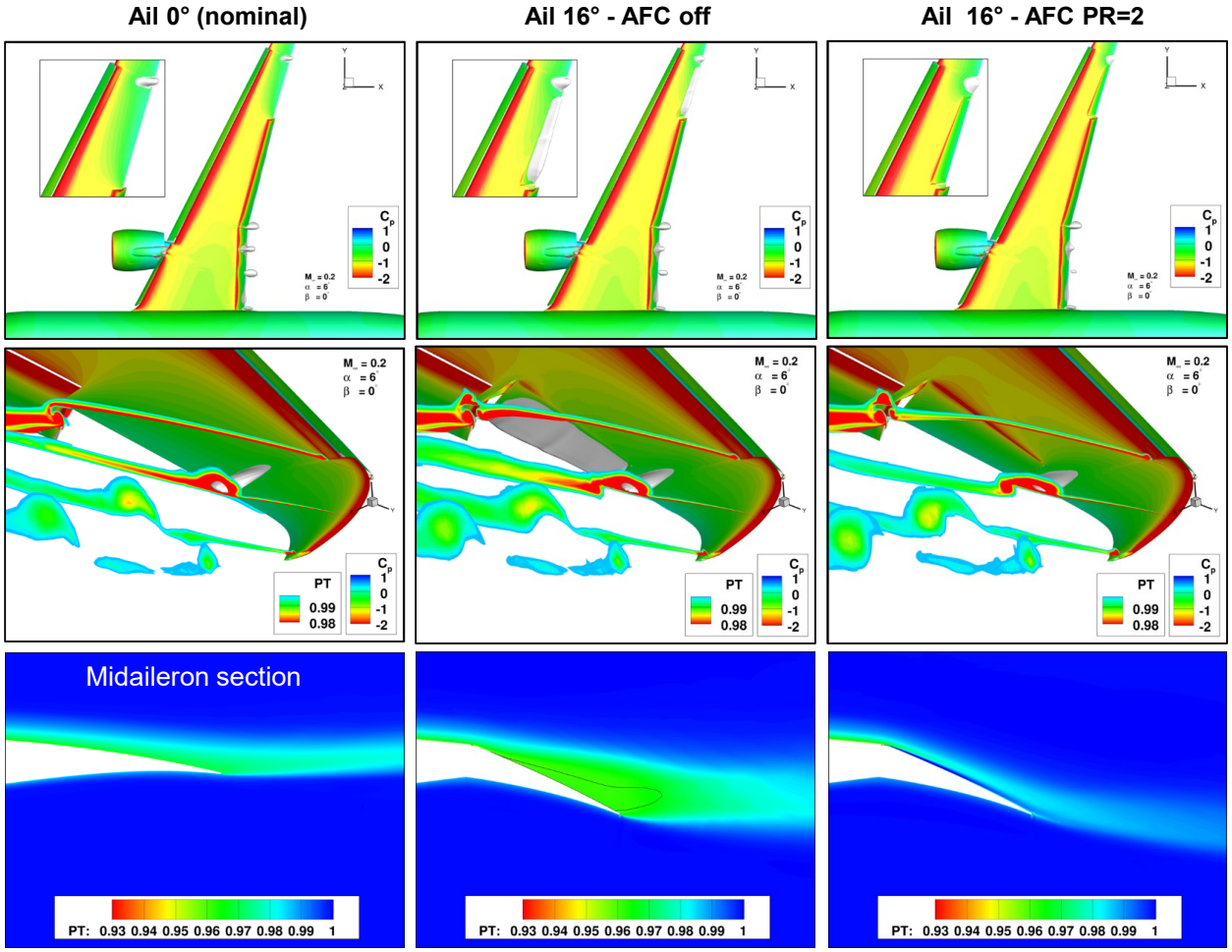

Figure 49 – Landing conditions: Flow fields for the baseline and the actuated nozzle 50% at PR=2 for Ail16, α=6°.

4.2 AFC in Leading Edge Region

An alternative method that aims at improved L/D at takeoff by applying flow control at the leading edge devices is investigated here. In one example, AFC is used in conjunction with the deployed slats, which was the subject of a previous study [12]. Subsequent to that study Boeing embarked on a follow up internal investigation to refine the AFC approach. A set of actuators have been embedded within the slat cove as an integral part of the high-lift system in order to enhance its performance and efficiency. During takeoff, the slats are deployed and the actuators are simultaneously activated. The system of air jets alters the flow recirculation within the cavity formed by the slat and main wing element. This flow mechanism results in reduction in total airplane drag. This is an unconventional application of flow control, which is customarily used for reduced flow separation.

Computational assessments will be used to investigate AFC applications in the slat cove as well as other related flow control concepts at the wing LE. Actuation modes and parametric sensitivities will be established for the Reference Aircraft. Although the aileron is deflected to the nominal 7.5° for takeoff, here AFC is applied exclusively at the LE, and it is separate from the aileron application in Section 4.1. Similar to the aileron application in Section 4.1, a practical design has to be powered by resources available on board. Therefore, the primary objective is to identify promising AFC approaches and preferred layouts that yield improved takeoff L/D with little or no degradation in lift, while using low actuation input.

4.2.1 Proximity to Fluidic Sources

The proximity to potential fluidic sources are an important factor in the design of the AFC system, therefore, considerations with regard to their potential availability is in order. Figure 50 presents a schematic layout of the Reference Aircraft, identifying the LE devices at which AFC is being considered. Flow control will be considered for the set of slats outboard of the engine strut (pylon). Air ducting is available in the strut region, where potential sources might include engine bleed. Also, an existing APU line at the engine station could be tapped into. Another potential source is the hot air of wing anti-ice (WAI) used in slats 3 and 4, and might offer AFC efficiencies associated with high temperature supply. Finally, compressors might be embedded at the wing LE for localized treatment with flow control.

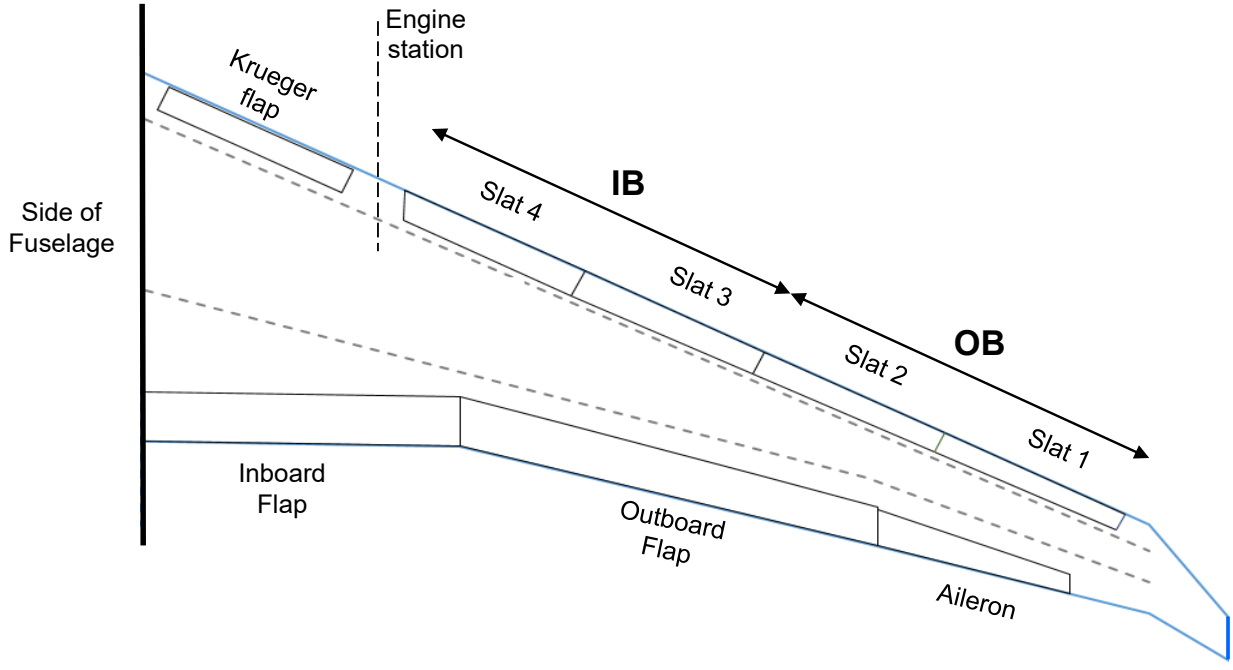

Figure 50 – Potential sources at the engine strut might be available for powering AFC at the slats.

4.2.2 Targeted Applications

Several AFC applications that will be described in the following sections are mapped in Figure 51. The orientation of the jet efflux is also schematically shown for the respective applications. Potential fluidic sources for each of these implementations are also listed. Further details and simulation results will be provided in the respective sections.

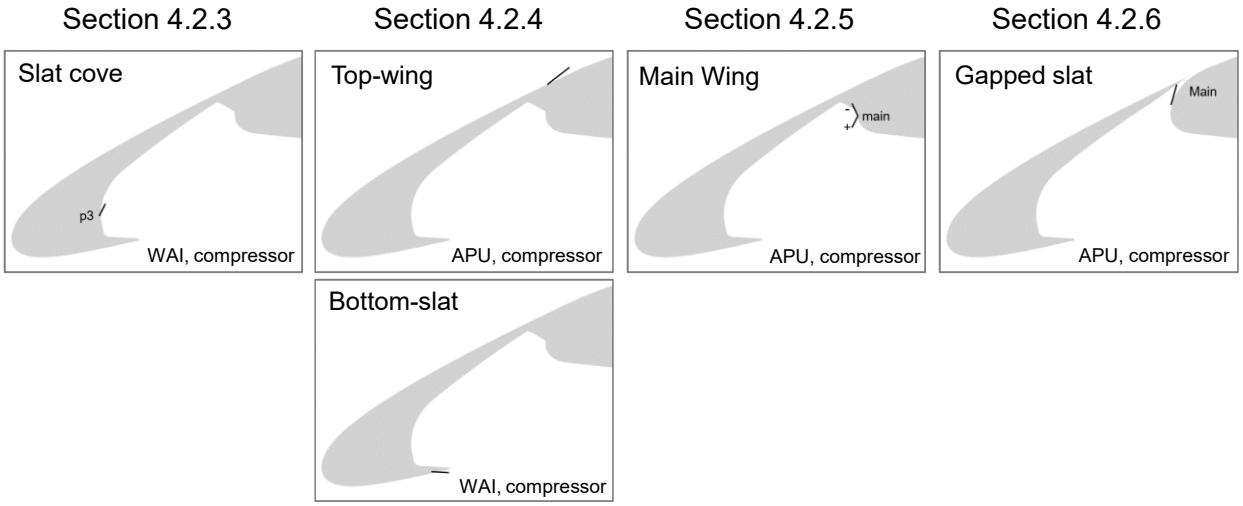

Figure 51 – Targeted AFC application at the leading edge region.

4.2.3 Slat Cove

The flow control is applied in the cove region of the sealed slat for the Reference Aircraft in Figure 50. AFC is first applied at slats 3 and 4, which are also the slat elements that use WAI. The cove region uses very fine grids to capture the important flow features associated with the recirculation flow and jet interactions. Surface boundary conditions are used on a strip of constant width along the slat span, as illustrated in Figure 52. In this section the jet is applied at the vertical section of the cove surface, which is the forward part of the cove. The jet is discretized by 40 and 136 cells in the xz and the spanwise directions, respectively. The grid consists of 98 million cells and 214 subzones. The jet angle is specified and AFC intensity is determined by PR and TR. The freestream Mach number is 0.20 and Re=6 million. The nominal angle of attack at takeoff is 6°. Figure 52 shows the Mach number contours on a vertical cut for the baseline and the actuated cases obtained for the nominal takeoff angle of attack of 6°. The baseline case indicates the formation of a counterclockwise vortex with a span component. This particular actuation helps suppress the recirculation.

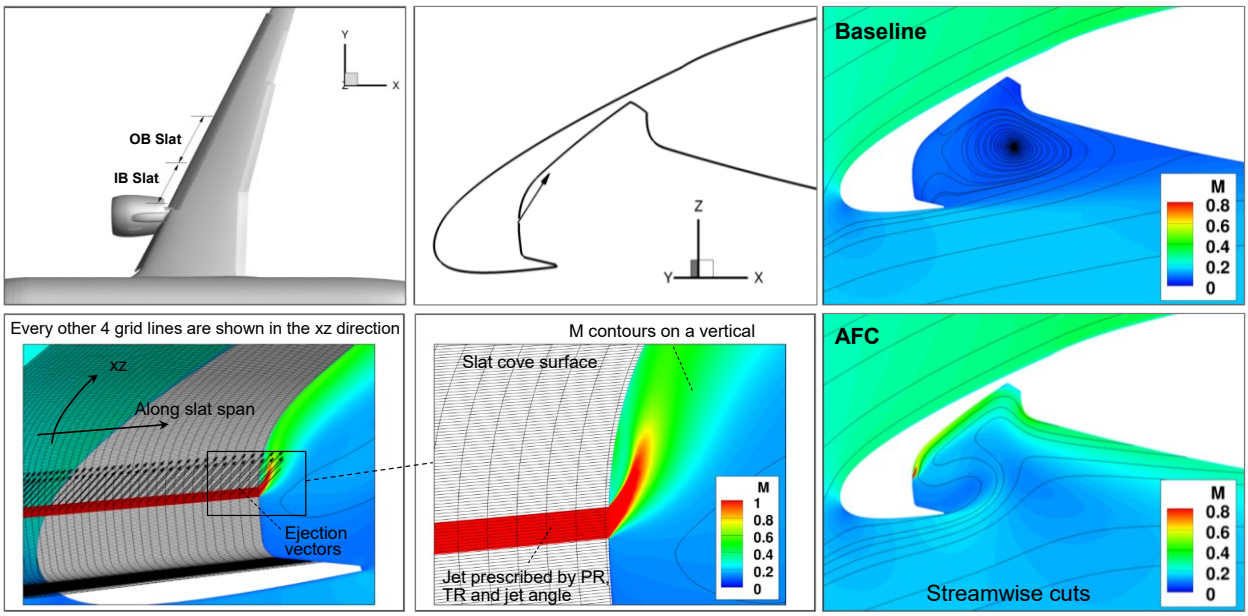

Figure 52 – Modeling approach of AFC in the slat cove

Figure 53 shows the flow around the airplane in a set of perspective views to help examine the impact of actuation on the flow structure. A set of streamwise cuts shows total pressure contours and wing wake development. A packet of streamlines from the slat cove help shed light on the flow patterns at the slats. The simulation indicates that the baseline flow is predominantly three dimensional in the vicinity of the slat, whereby vortical flow forms in the slat cove and it emerges into the ambient stream toward the wingtip. In a sense, the vortex is trapped within the cove. The actuation pattern shown in the inset depicts the ejection vectors that protrude through the transparent OML. The actuation helps break the original counterclockwise flow. This helps curb spanwise flow in the cove region and reduce 3D effects. The streamlines indicate that the actuation promotes faster mixing of the cove stream with the surrounding flow. The intensity of the trailing vortex is thereby reduced, hence resulting in lower airplane drag.

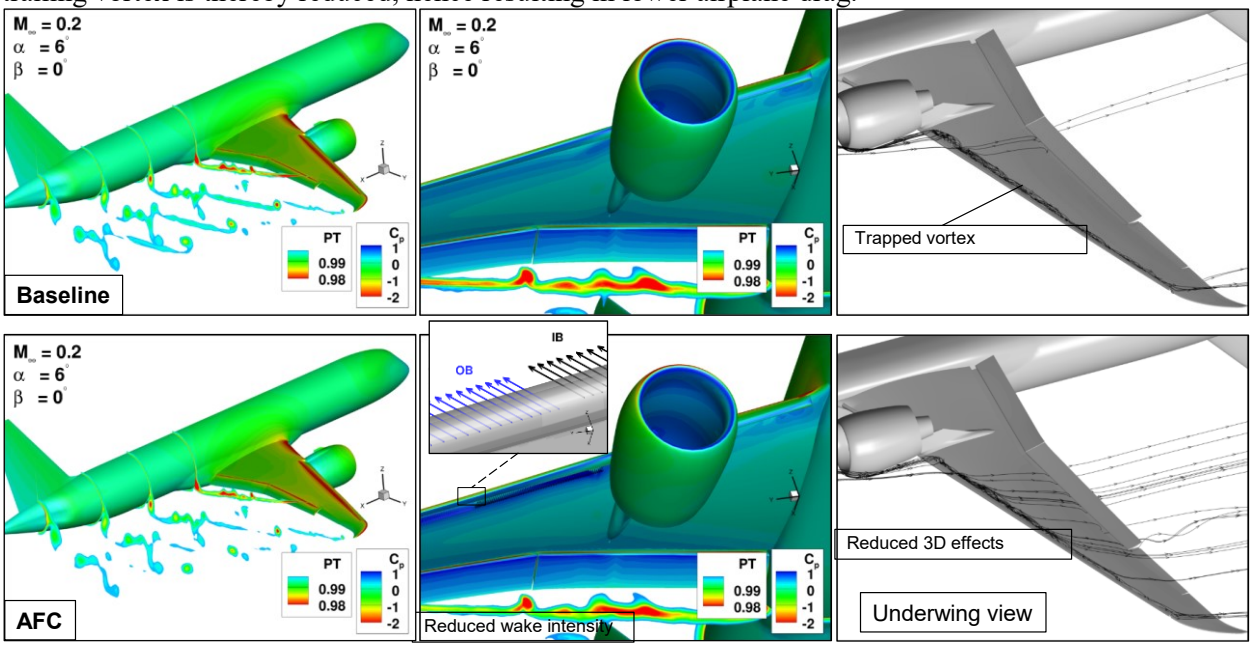

Figure 53 – Impact of slat cove AFC on airplane flow structure.

The first round of simulations uses actuation in the coves of slats 4 and 3, or in the IB and OB segments per the notation of the planform inset in Figure 52, respectively. A set of simulations were obtained for various jet angles and jet layouts. These results are included in 'Appendix A – AFC Layouts for the Slat Cove', and a concise summary is presented in Figure 54 in terms of L/D improvement as a function of actuation mass flow. These flow control patterns are based on xy20, where the jet is at 20° off the surface and it points toward the tip of the wing. In addition to the first three patterns, which have been described in 'Appendix A – AFC Layouts for the Slat Cove', two other layouts are included. In the xy20 IB Midx2, the jet is applied at the center of the IB slat element over 25% of its span. The xy20 IB Mid Thin layout denotes a jet applied at the center of IB over 50% of its span, and it is half the jet width used in all the other xy20 patterns. The results indicate that only the smaller jets of these last two layouts require mass flow within the limits of an equivalent APU, producing less than 1% improvement in L/D. Figure 55 shows the aerodynamic characteristics of some of the patterns.

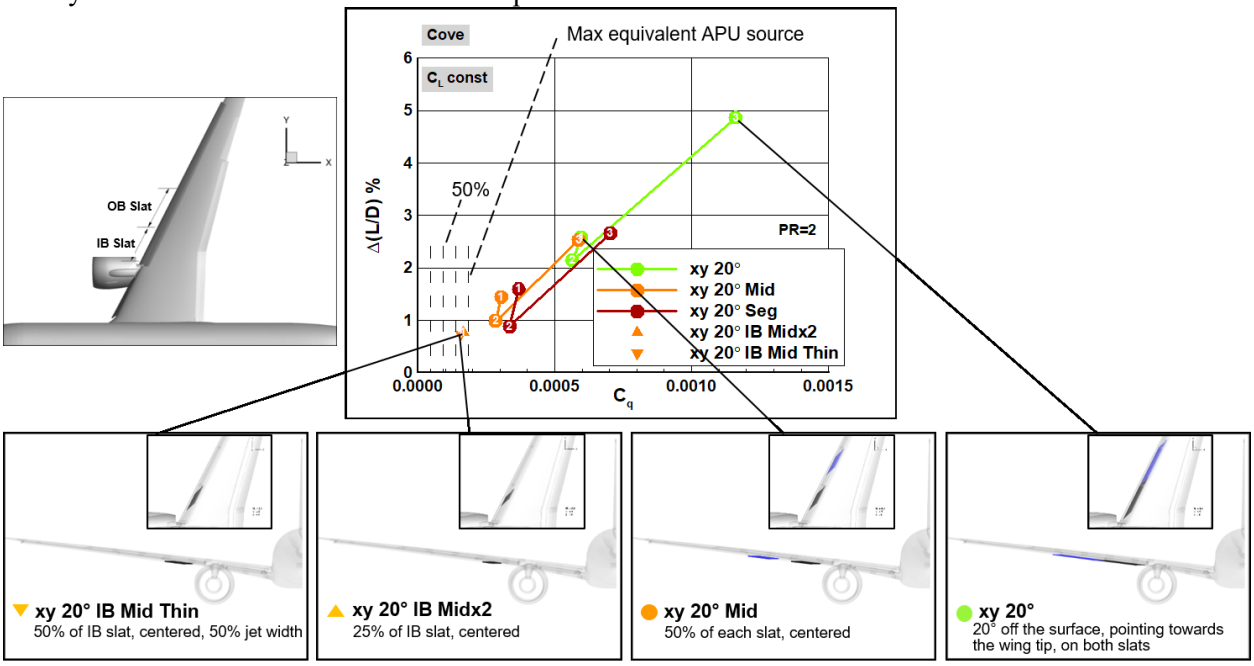

Figure 54 – L/D gains due to actuation in the slat cove.

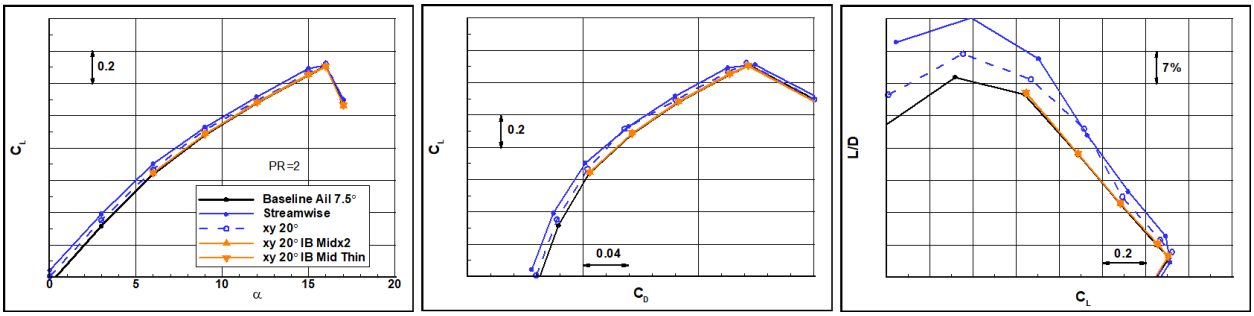

Figure 55 – Effect of slat cove actuation on the aerodynamic performance.

4.2.4 Top-Wing/Bottom-Slat

Other possible applications of AFC might be considered. For example, actuation on the top of the wing in the wing under-slat surface (WUSS), so that the actuator exit is concealed within the OML during cruise. Potential sources are APU or local compressors. Another potential application of AFC is at the lower surface of the slat where the air from the WAI system is exhausted into the freestream. Pressurization of this air could be exploited for flow control if proven aerodynamically beneficial. These two application

types are denoted Top-wing and Bottom-slat. Sample solutions are shown in Figure 56 with actuation on all the slat elements, based on the convention in Figure 50, where IB consists of slats 3 and 4, and OB includes slats 1 and 2. The L/D gains due to the Top-wing and Bottom-slat are shown in Figures 57 and 58, respectively. Flow control patterns marked "Mid" denote a jet centered at the midspan of the slat, spanning 50% of its length. Also, the jets have a fixed nominal width, unless marked Thin, which signifies a smaller jet width having half the nominal value. The label "Thinx2" is a jet of one quarter that of the nominal jet width. The actuation intensity of the cases identified by individual symbols corresponds to PR=2. Selected flow control patterns have been obtained at PR=2 and 4, in which cases, they are identified by a solid line. Generally, actuation at the OB section is more effective than IB, for both the Top-wing and Bottom-slat modes. Also, Top-wing is more effective than Bottom-slat. This is conveniently inferred from Figure 59, which groups the cases from Figures 57 and 58 into the black and blue family of symbols, respectively. Based on these results and assuming a maximum allowable mass flow level of an APU (the right most vertical dash line), the following conclusions can be drawn. The Bottom-slat pattern 'AFC Bot OB Mid Thin' produces an L/D gain of about 1% at PR~1.5. The Top-wing actuation 'AFC Top OB Mid Thin' with PR~2.5 results in 3% improvement in L/D.

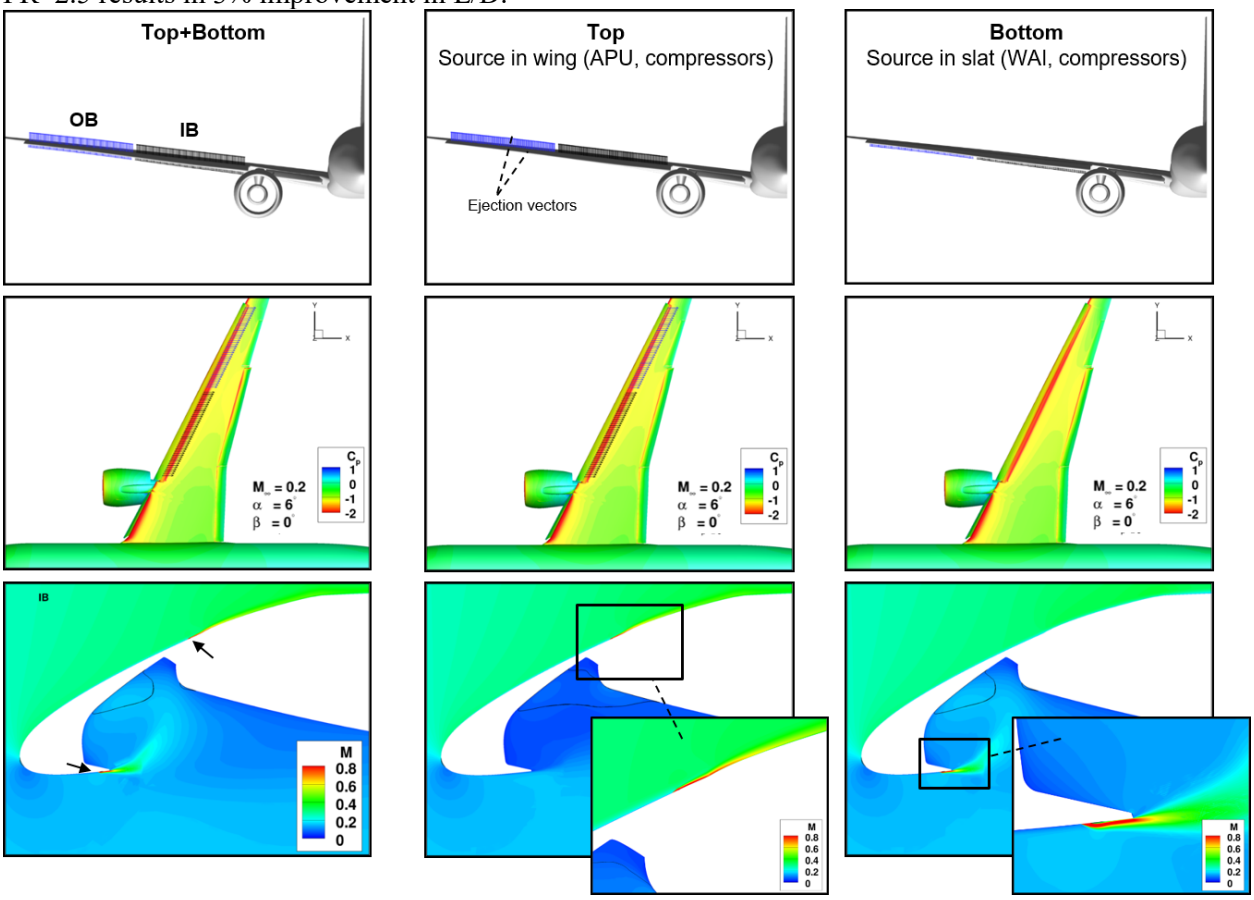

Figure 56 – Top-wing, Bottom-slat and combined Top-wing/Bottom-slat applications.

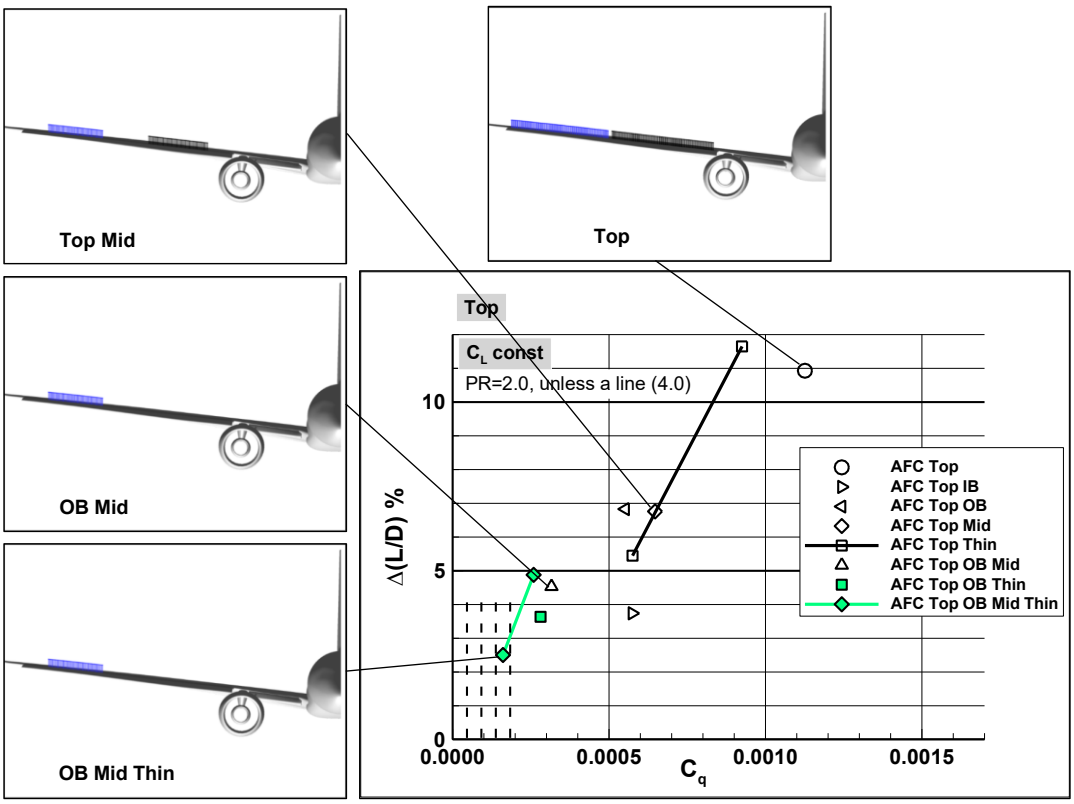

Figure 57 – L/D improvements due to AFC at the top wing.

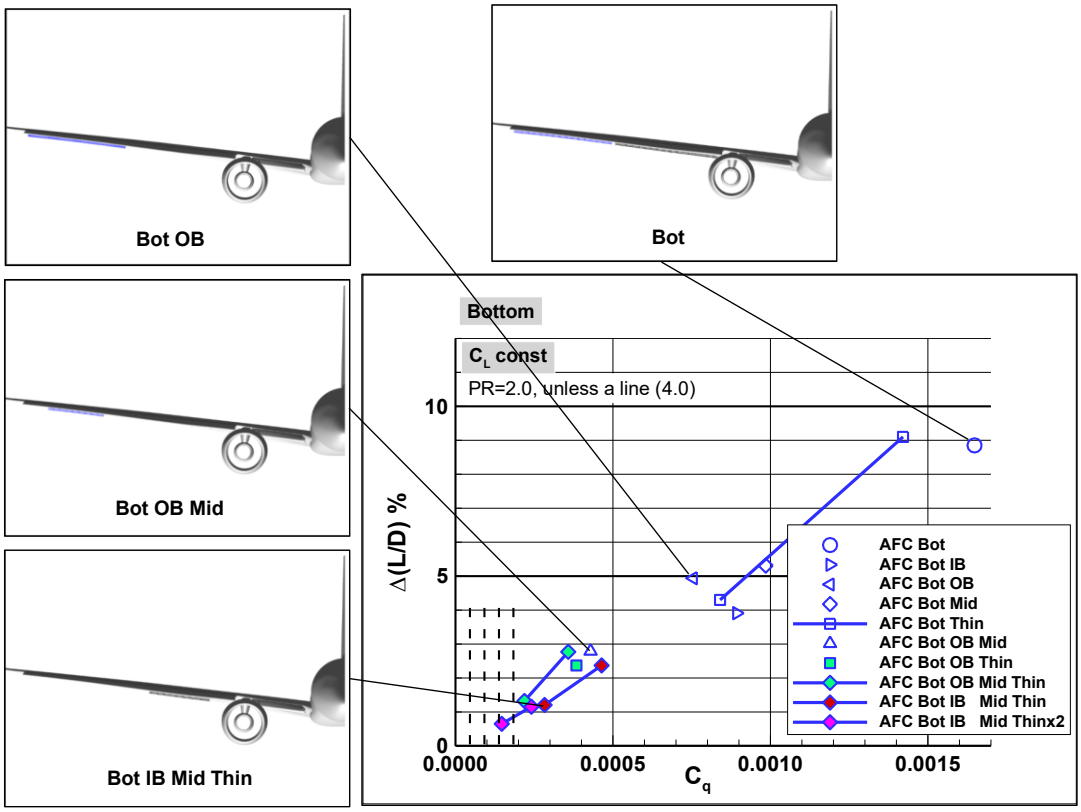

Figure 58 – L/D improvement due to AFC at the bottom slat.

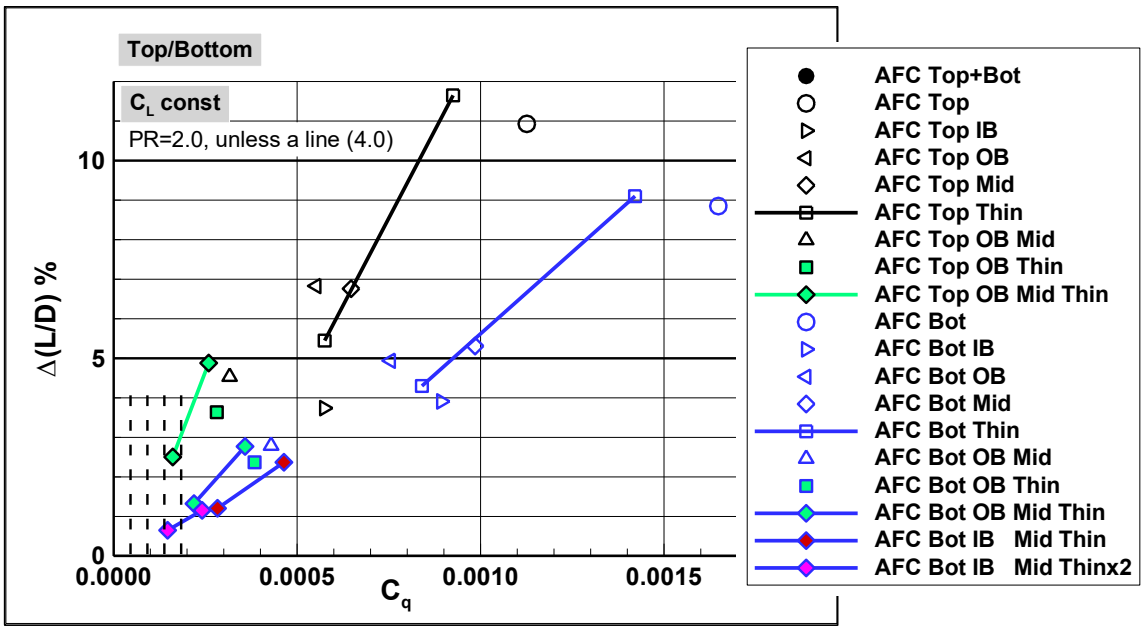

Figure 59 – L/D improvement due to combined top wing/bottom slat application.

The aerodynamic performance of some of the actuation patterns are shown Figure 60. Aside from potential for higher L/D, there is also a benefit in maximum lift, which is also presented in terms of percentage improvement as function of actuation input level.

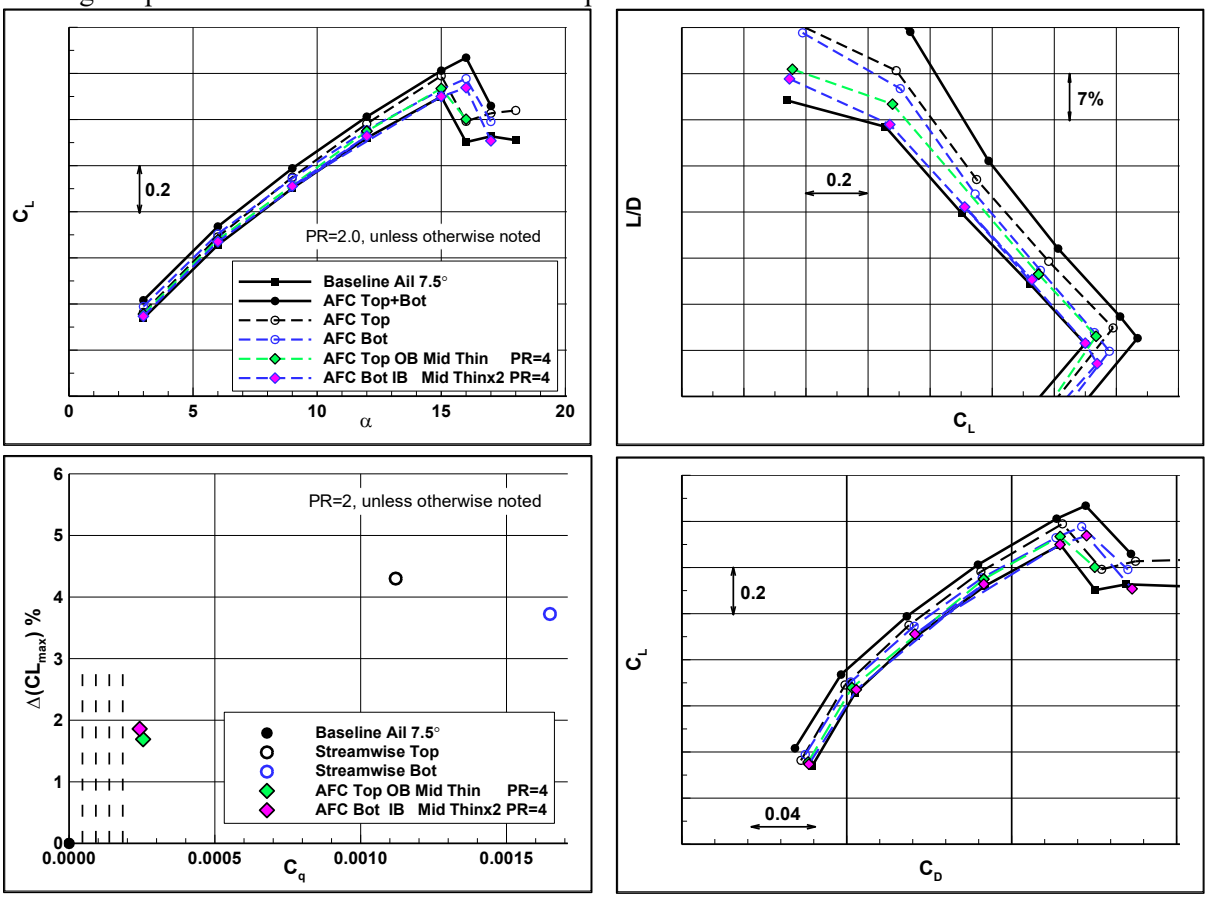

Figure 60 – Aerodynamic performance due to selected AFC applications from Figures 57 through 59.

4.2.5 Main Wing

Actuation is applied in the slat cove but at the main wing element. Potential fluidic sources are APU and local compressors. Figure 61 presents the flow fields in the cove region in the midsections cuts of the IB and OB segments. The jet angle is at about 40° angle to the surface. The jets are applied in the clockwise and counterclockwise directions, and denoted ‘p’ and ‘m’, respectively. The nominal jet width is identical in both cases. These solutions are shown in the two columns on the left hand side of Figure 61. The L/D gains are shown in Figure 62. The plot includes solutions obtained for thinner jets, having 50% of the nominal jet size. These smaller jets are marked ‘p Thin’ and ‘m Thin’. Although the clockwise oriented jets are slightly more effective, none of these jet patterns offer benefits in the practical mass flow range. For a more effective Coanda effect in the LE region where surface curvature is relatively high, a shallower angle of about 30° was also applied to the clockwise jet. This pattern is shown in the right column in Figure 61 and it is dubbed ‘p Ang-10’. The L/D gains for a set of patterns are shown in Figure 63, demonstrating that refinements in jet layout might yield significant improvements. There is high dependency on jet angle and span location. Jets with smaller surface angles are more effective. Also, outboard placement of the jets is more advantageous, similar to the findings in Section 4.2.4. Nevertheless, main wing application produces modest gains in L/D. The aerodynamic performance obtained with actuation at the wing is shown in Figure 64 for selected jet patterns, indicated no improvement in maximum lift.

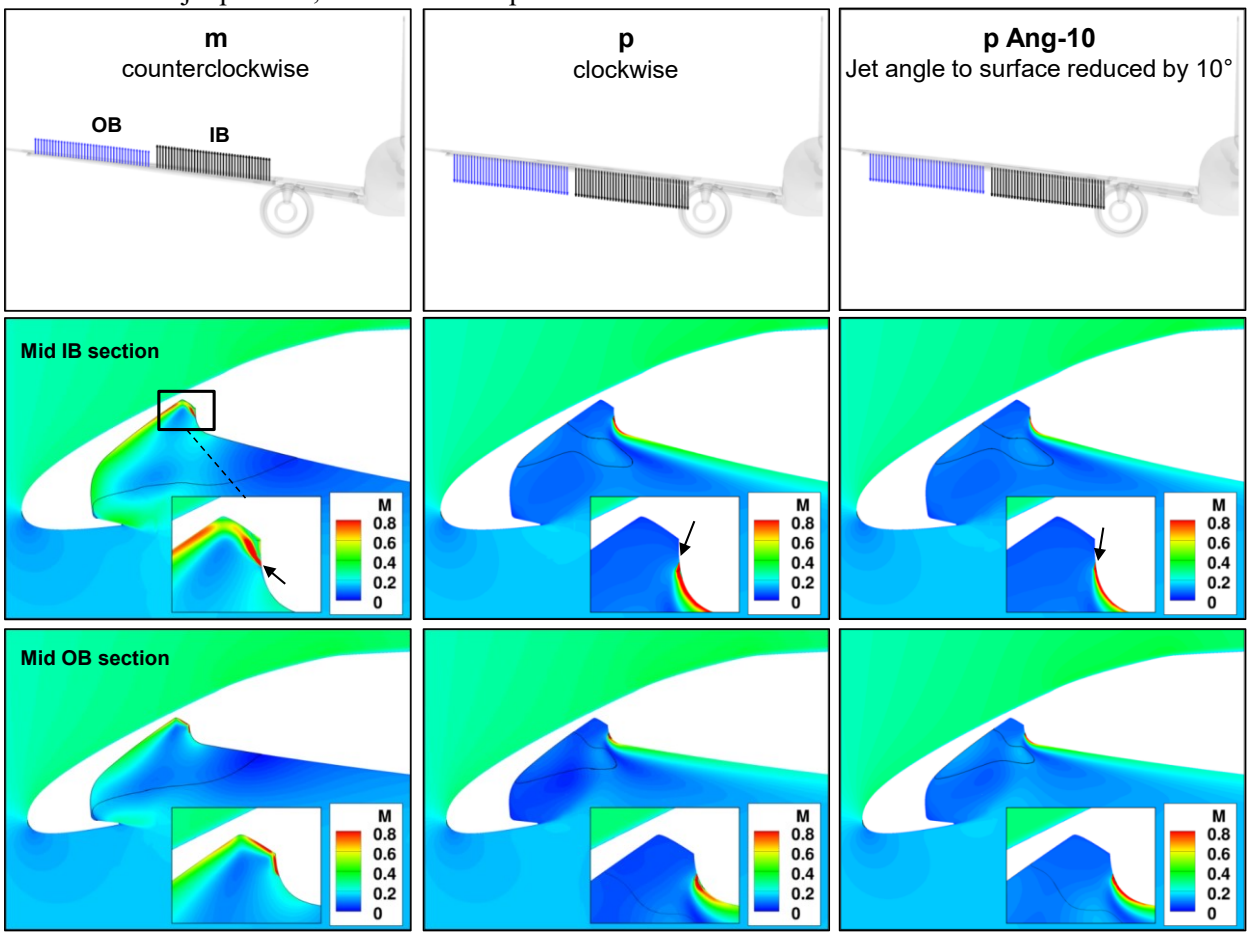

Figure 61 – Main wing applications.

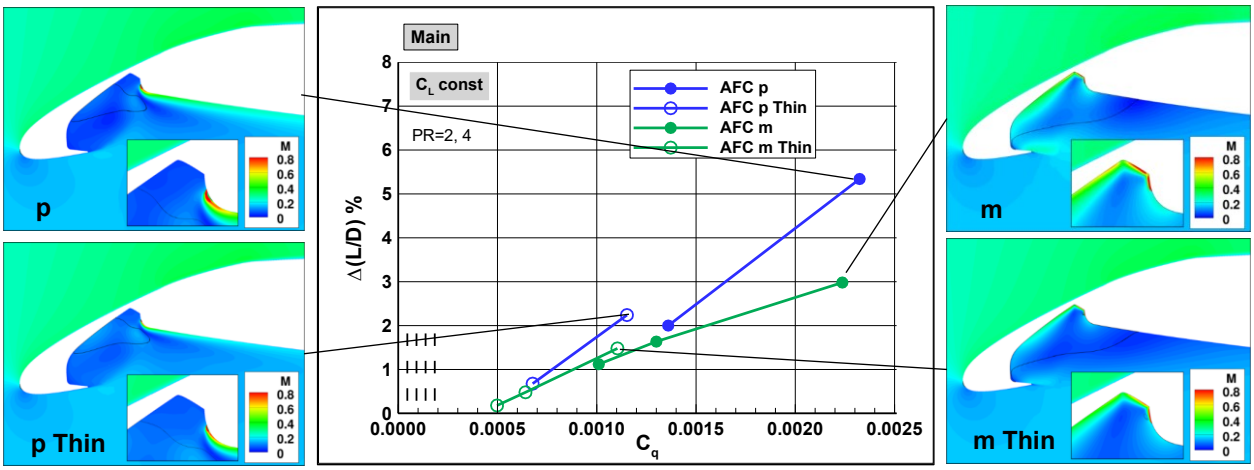

Figure 62 – L/D due to AFC at the wing.

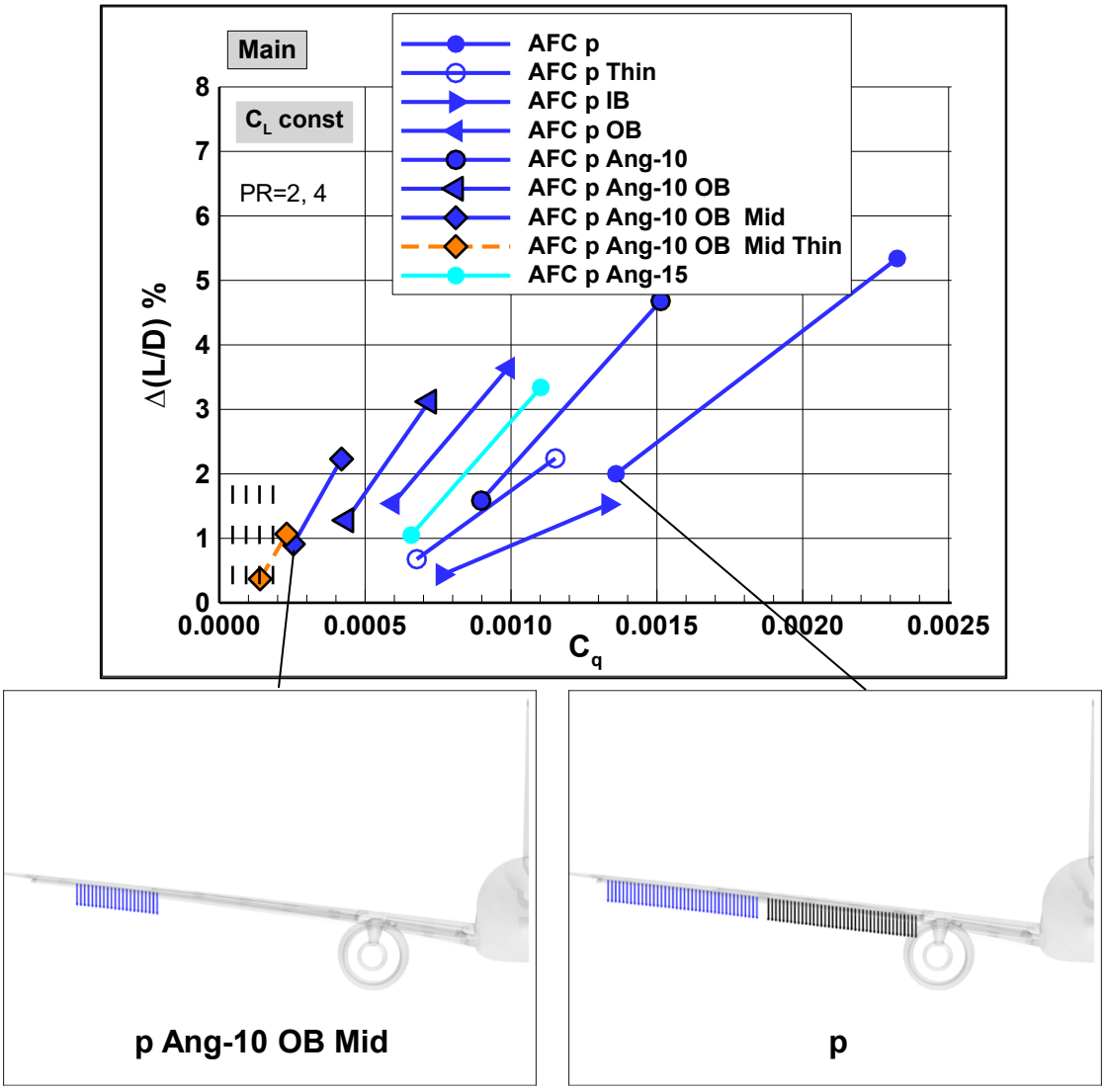

Figure 63 – L/D improvements due to AFC at the wing for various jet patterns.

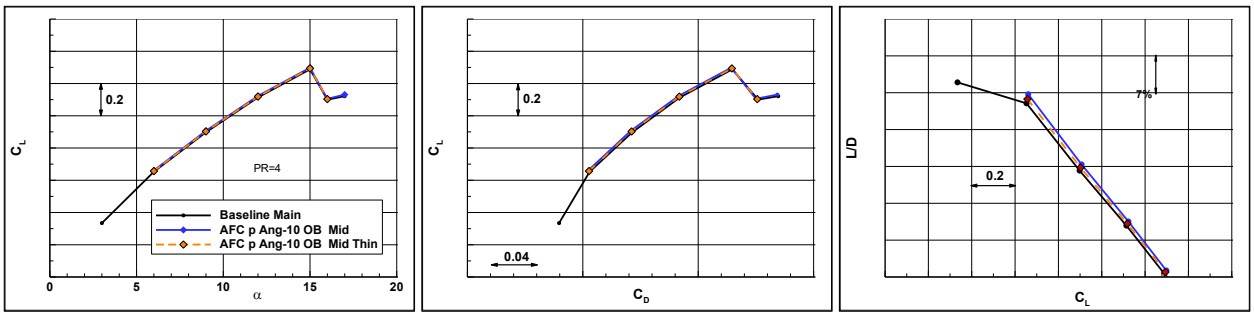

Figure 64 – Aerodynamic performance due to AFC on the wing for selected AFC applications from Figure 63.

4.2.6 Gapped Slat

This flow control approach was conceived from the Top-wing (Section 4.2.4) and Main wing (Section 4.2.5) applications. For convenience, the Mach number distributions at a spanwise cut in the LE region obtained with these two approaches are presented in Figure 65. The gapped slat variant is obtained by introducing a small gap between the slat and main wing. The flow control is provided by a jet similar to the one shown in the Main wing inset. Here the jet is injected at a ~20° angle to the surface toward the throat section. Essentially the gap creates an effective converging nozzle, so that the jet will emerge over the upper surface of the wing, similar to the jet ejection in the Top-wing case. The converged nozzle helps accelerate the jet to higher velocity, thus providing high momentum and amplifying flow control effectiveness. In yet another variant, also included in Figure 65, the gap is designed to create an effective convergent/divergent nozzle so that the jet can be accelerated to supersonic flow for even higher momentum. The convergent/divergent gap will be used in the following results. The gapped slat application can be powered by either APU or local compressors.

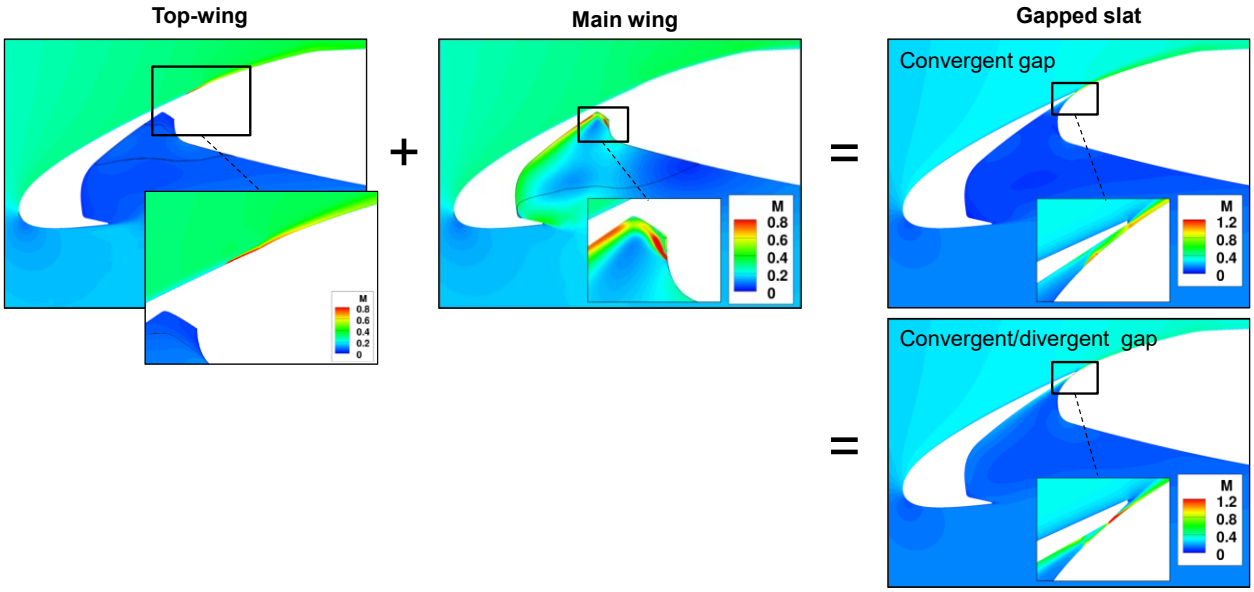

Figure 65 – Gapped slat layout is obtained from the combination of the Top-wing and Main-wing approaches.

The CFD model for the gapped slat is shown in Figure 66. The slat is at the same detent as in the original sealed position in order to preserve the general aerodynamic characteristics of the original wing. For the purpose of this analysis the slat lower surface is modified to incorporate a convergent/divergent section. The nozzle area ratios will determine the jet velocity as it exits the gap. The diffuser section has an angle of 7.5° to help prevent local flow separation. The wing surface was not modified. It is noted that the gapped slat system uses very small gaps and the slats are at the takeoff detent, and it should not be confused with the slotted (sometimes referred to as gapped) slats used at landing.

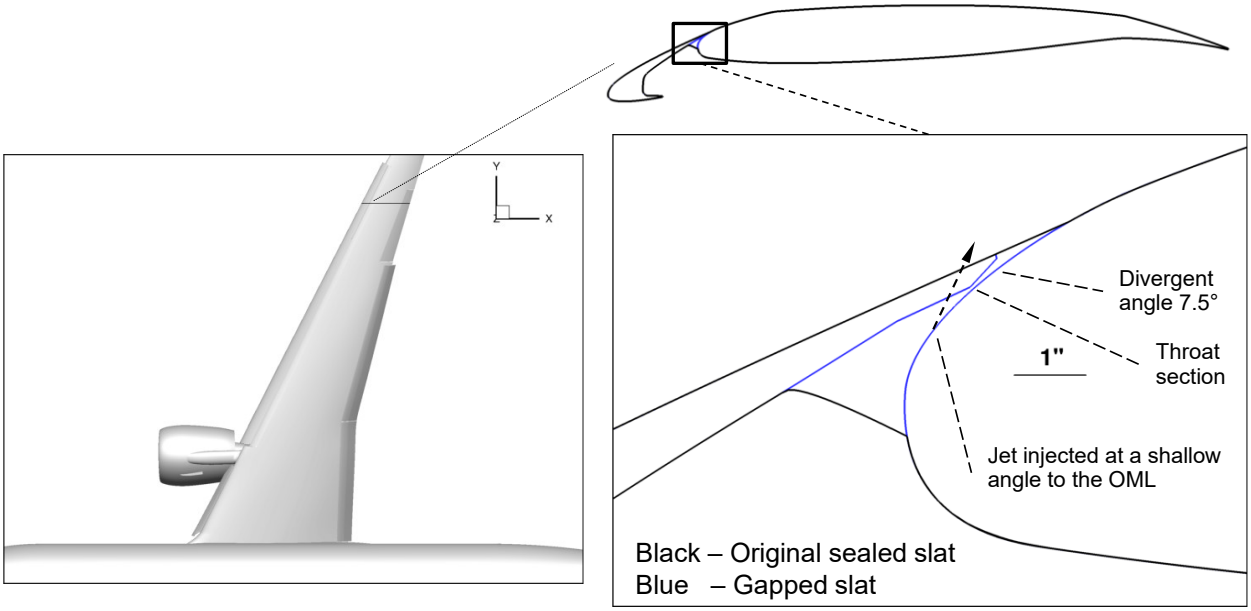

Figure 66 – Gapped slat geometry for the CFD model.

An optional implementation of a gapped slat system on the airplane is shown in Figure 67. Here the wing has alternate span segments that incorporate very shallow indentations in the WUSS. When the slat is in the sealed position, the indented sections become gapped and the nonindented sections become sealed. In other words, in the sealed slat mode, the indentations form a set of nozzles from which the jets are ejected on the upper surface. When the slats are retracted, the indentations are completely hidden and the cruise mold lines are not affected. Another implementation might use indentations on the lower slat surface.

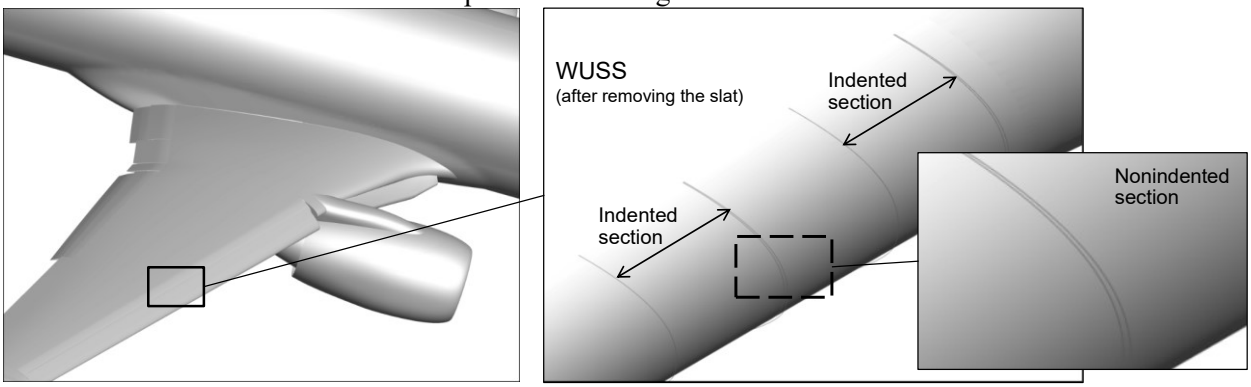

Figure 67 – Gapped slat implementation.

In the first round of CFD simulations, a single grid system was used with gaps at the four slat elements (see Figure 50). A systematic analysis revealed that the outboard slat (slat 1) was the most effective. However, applying AFC only on a single slat has rendered the unactuated slats effectively unsealed (open gaps). This has resulted in maximum lift degradation. Therefore, a new grid system was developed where only slat 1 incorporates the gap, at the wing segment where actuation is applied. The initial analysis with the set of four gapped slats is described in 'Appendix B – AFC for All Gapped Slats'. The results with the gapped outboard slat are presented next.

Figure 68 shows the solutions for several AFC layouts. The actuations with PR=2 and 4 clearly show that the jets are diffused right after leaving the wing surface, but accelerate to sonic velocities at the throat section, and further to supersonic velocities in the divergent section of the gap. The actuation produces a thin film of high momentum that remains attached to the upper wing surface. The difference in the flow development on the upper surface between the two jet intensities is evident. The effect of jet location relative to the throat section is shown in the third column from the left. Relative to the original location, the jet has been placed further downstream and closer to the throat. This actuation uses PR=2 and it is denoted 'OB Dns'. Relative to the original jet location (first column), 'OB Dns' results in higher velocities in the diffuser and further over the upper surface of the wing. The fourth column presents a case in which the original PR=2 actuation is limited to just the outboard half of the slat, labeled 'OB ob'.

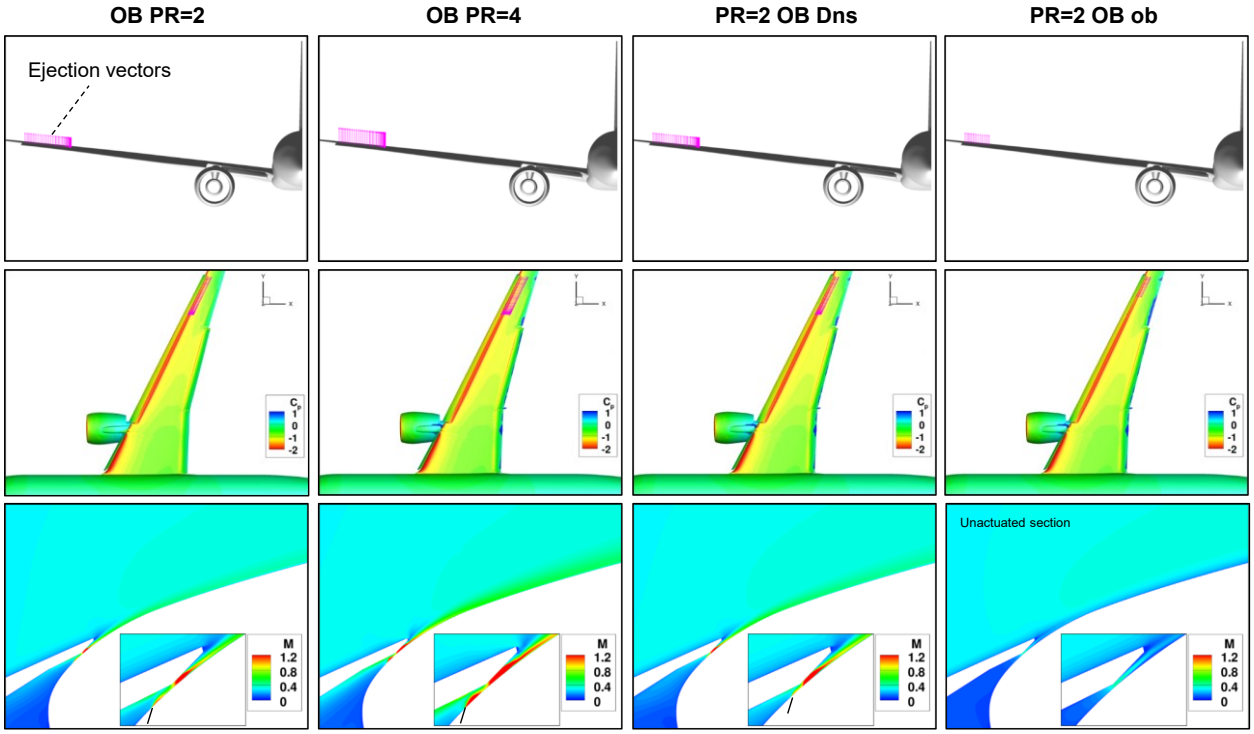

Figure 68 – Selected gapped slat applications on the outboard slat (slat 1).

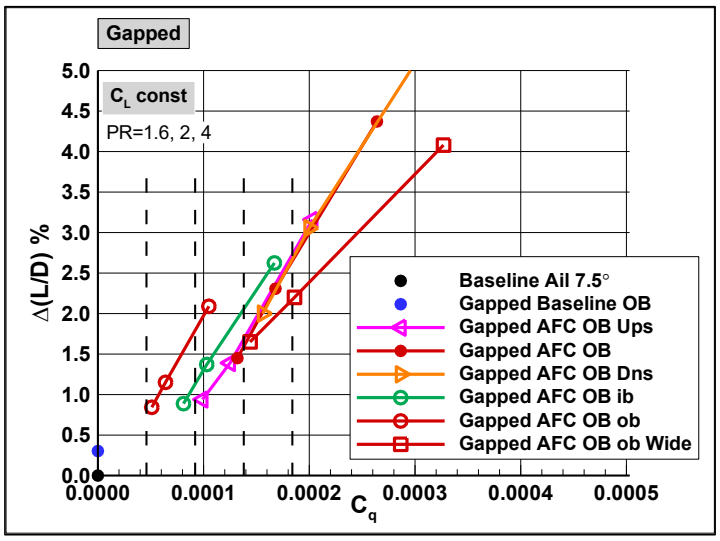

Figure 69 – L/D improvement due to gapped outboard slat.

The improvements in L/D are presented in Figure 69 for the patterns described above and several additional variants. 'OB Ups' denotes a jet that is placed further upstream relative to the original location in the first column in Figure 68. 'OB ib' uses actuation in the inboard half segment of the outboard slat. 'OB ob wide' is a jet with twice the width of actuation 'OB ob'. First, it is noted that the gapped slat with no actuation helps gain about 0.3% in L/D. Using a set of PRs of 1.6, 2 and 4, several of the patterns land in the practical range of mass flow that could be supplied by the APU. In terms of jet placement, the closer to the throat area the jet is, the more effective the actuation. For example, at PR=1.6, 'OB Ups' results in 1% increase in L/D, 'OB' in 1.5% and 'OB Dns' in 2%. Actuation on the outboard part of the slat 'OB ob' is more effective than the inboard segment 'OB ib'. Finally, the wider jet does not yield higher actuation efficiency. An increase of about 2.7% in L/D is achievable with several jet configurations at various pressure levels and within the APU limits. Figure 70 shows the aerodynamic performance of several of the patterns, indicating that the original $C_{L,max}$ is preserved.

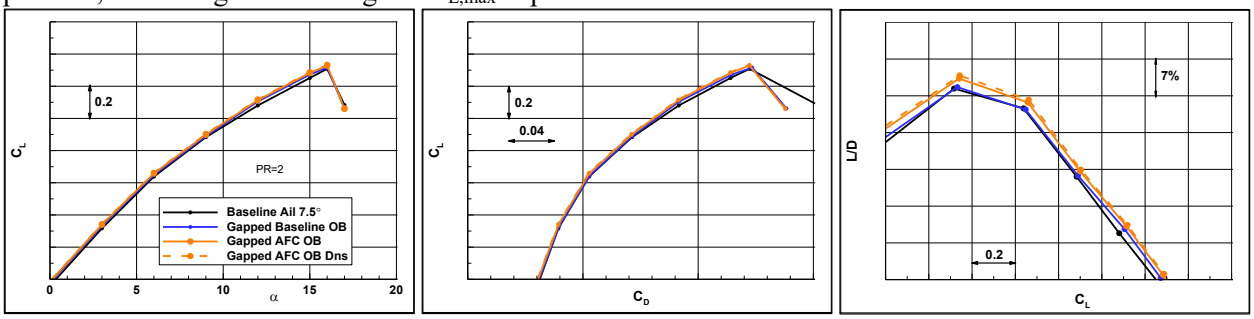

Figure 70 – Aerodynamic performance due to gapped outboard slat.

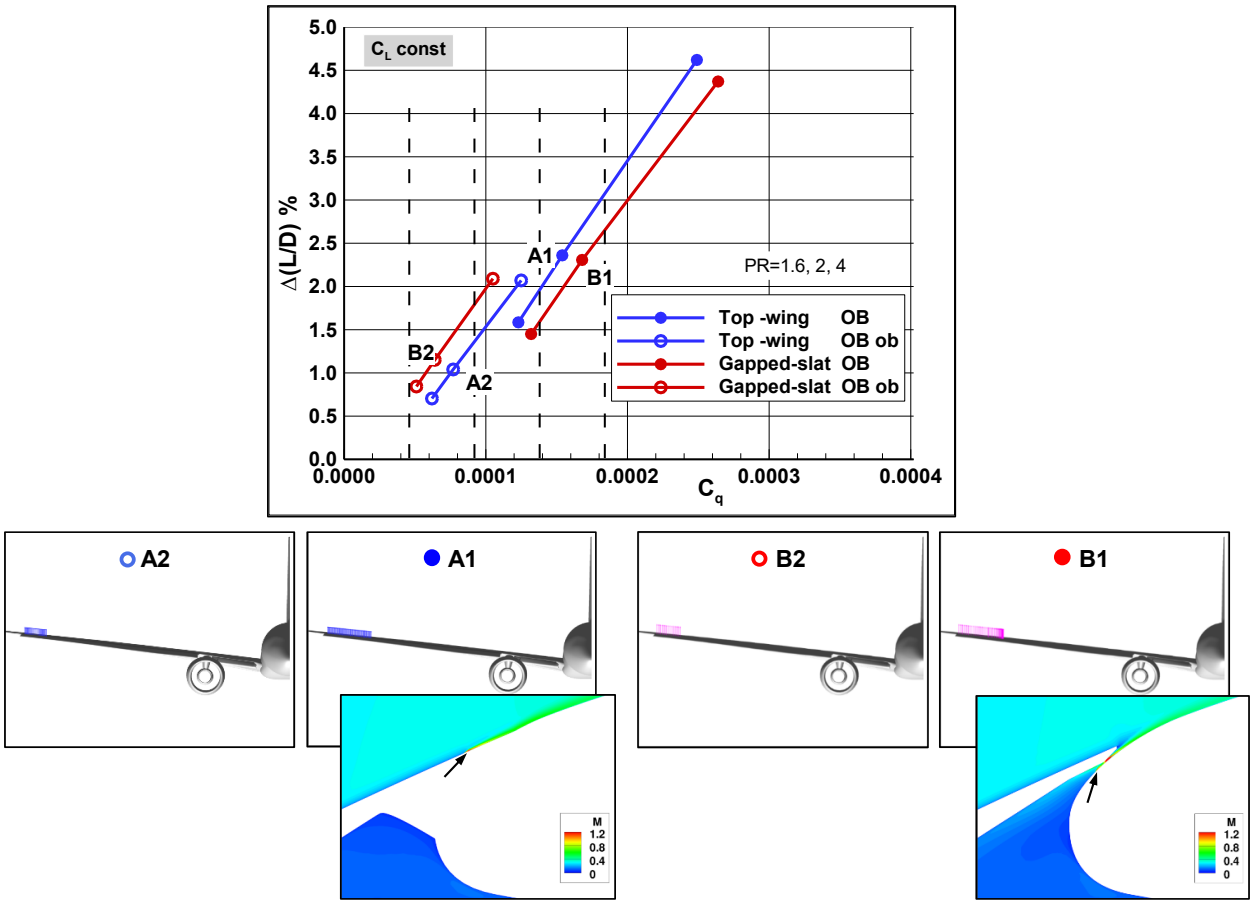

Figure 71 – Aerodynamic performance of Top-wing and Gapped-slat at the outboard slat element.

At this point it becomes obvious that the Top-wing actuation and the Gapped-slat produce similar results. Although there will be different aspects of integration of such systems, it is instructive to compare their aerodynamic performance. This is presented in Figure 71. It is noted that this is merely a comparison of results obtained for two AFC approaches and there was no attempt to implement the flow control in a consistent manner. For example, the jet width and the jet angle to the local surface are different. Nevertheless, the trends in L/D appear to be quite similar with measurable L/D improvement in the practical C_q range. It is interesting that the relative benefits between the two implementations switch as actuation is placed closer to the wingtip. Top-wing is more effective when actuation is applied on the entire outboard slat (OB), whereas the advantage flips over to the Gapped-slat when the actuation is confined to the outboard segment of the slat (OB ob). This implies that further gains could be realized by refining these initial implementations in both actuation approaches.

4.3 AFC in Nacelle-Pylon-Wing Region

The integration of the engine installation with the wing high-lift system introduces interference effects that adversely impact the airplane performance during low speed operations. AFC has been applied in the general wing/pylon region in order to alleviate the aerodynamic shortcomings and improve performance over the range of angles of attack, including $C_{L,max}$. This problem is especially important for the integration of very high-bypass-ratio engines of future airplanes. In addition to the potential to enhance aerodynamic performance, AFC might enable simpler integration of the high-lift system with the pylon. Reduced complexity of this mechanical system might result in lower weight and maintenance costs.

4.3.1 Effect of AFC on the Flow Structure

The flow control layout used for this application is shown in Figure 72 together with the baseline flow at the nominal takeoff condition of α=6°. The inboard Krueger flap and the outboard slats are sealed. The flow features of the baseline can be seen from the cross-sectional cuts of total pressure contours. Three vortex elements form at the chine, the inboard side of the pylon and the inboard edge of the sealed slat. A very fine mesh has been introduced on the fixed wing element in the pylon region for representing small width jets using surface boundary conditions. The flow control is applied on both sides of the pylon station as indicated by the color coded efflux vectors, representing nominal sized jets. The jets lie in the xz plane at the same nominal angle. The results for the baseline and the actuated flows with PR=4 are shown in Figures 73 and 74 for the flows at α=6° and 16°, respectively, the latter representing near $C_{L,max}$ conditions. At α=6° the intensity of vortex elements is substantially reduced by actuation. As the flow incidence increases, flow separation originates at the slat edge, developing into a sizeable bubble at α=16°. The momentum provided by flow control helps suppress the separation and improve the flow quality over this wing segment.

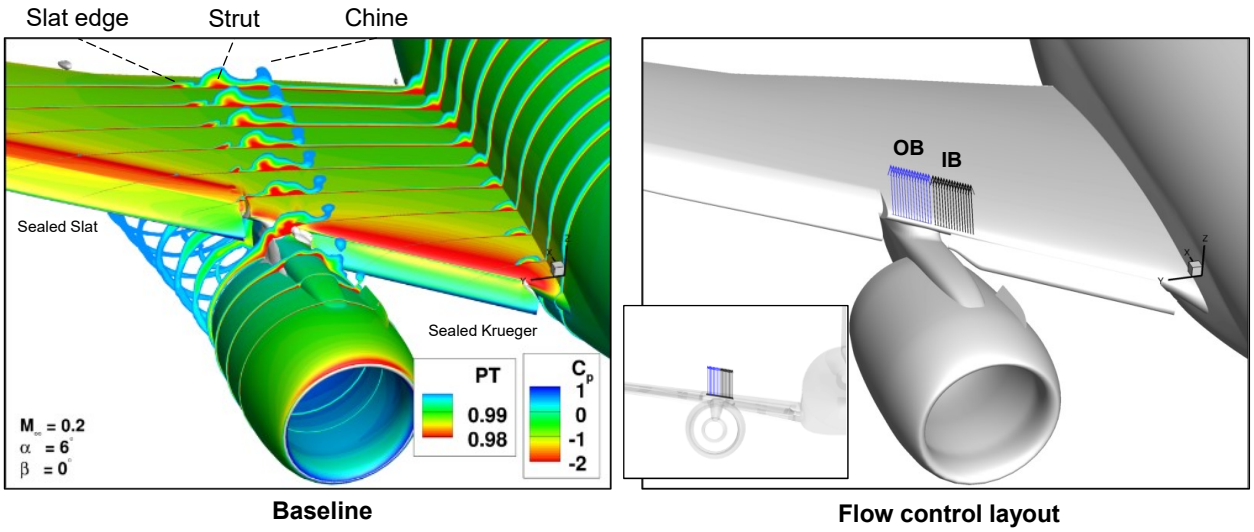

Figure 72 – AFC for improved nacelle/pylon/wing integration.

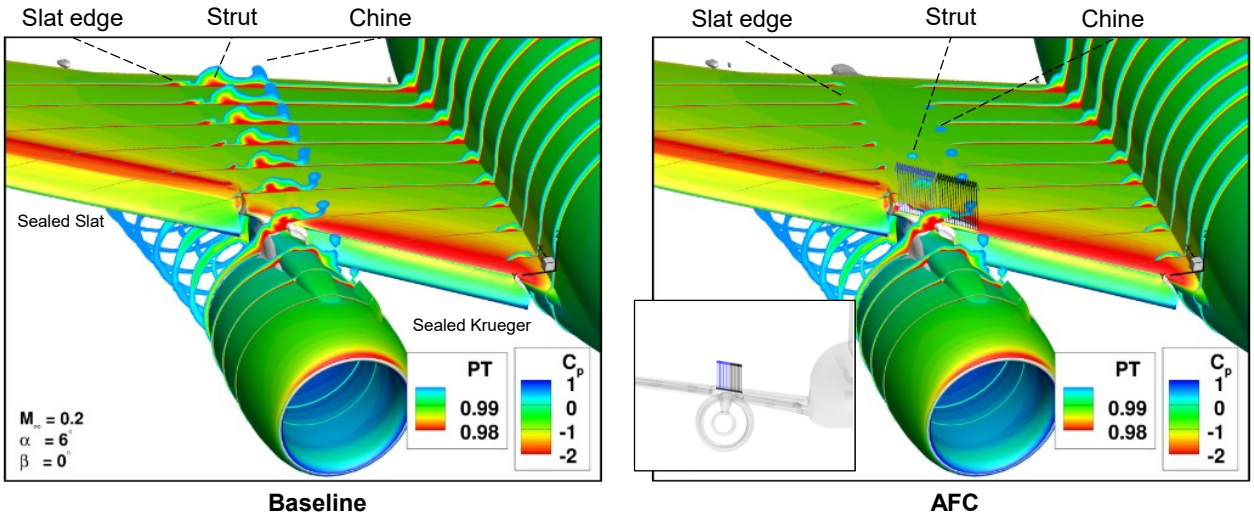

Figure 73 – AFC effect at nacelle/pylon/wing, α=6°.

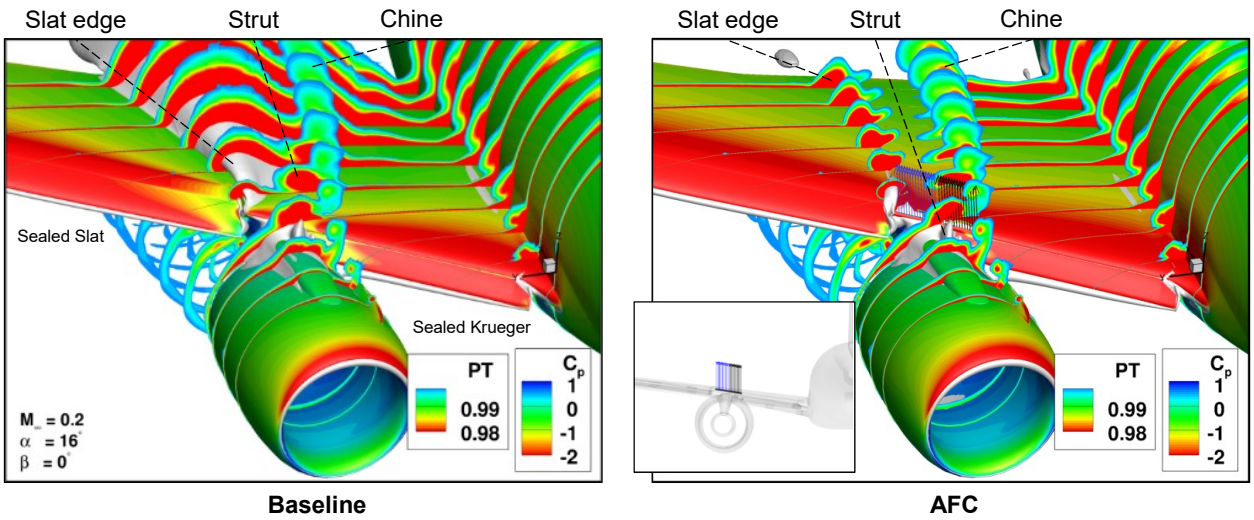

Figure 74 – AFC effect at nacelle/pylon/wing, α=16°.

4.3.2 Sensitivity to AFC Patterns

Figure 75 shows flow fields obtained at α=6° for a set of AFC layouts with PR=4. Spanwise cuts on either sides of the pylon are also presented. The inboard section is a cut through the sealed Krueger flap and the outboard cut slices through the sealed slat. The two columns on the left hand side are the cases shown in Figure 73. The 'Mid' and 'Midx2' notations signify jets whose span lengths are 25% and 50% the size of the nominal jets. Because of the relatively high surface curvature in the area where flow control is applied, the effects of shallower jet angles have also been assessed. The jets marked 'Ang -15' indicate jets having an angle that is smaller by 15 degrees relative to the nominal orientation. Clearly the smaller angle causes the jets to attach quicker to the surface, thereby reducing the tendency of flow recirculation immediately downstream at the foot of the jets. The gains in aerodynamic performance due to AFC is shown in Figure 76. Results indicate that the smaller jet angle is more effective. Additionally, the outboard actuation patterns (OB) are much more effective than the inboard counterparts (IB) as they avert the formation of the separation at the slat edge, especially in terms of maximum lift. Relative to the applications in Sections 4.1 and 4.2, the gains in $C_{L,max}$ due to AFC at the nacelle/pylon/wing are substantial, but the improvement in L/D is fairly modest.

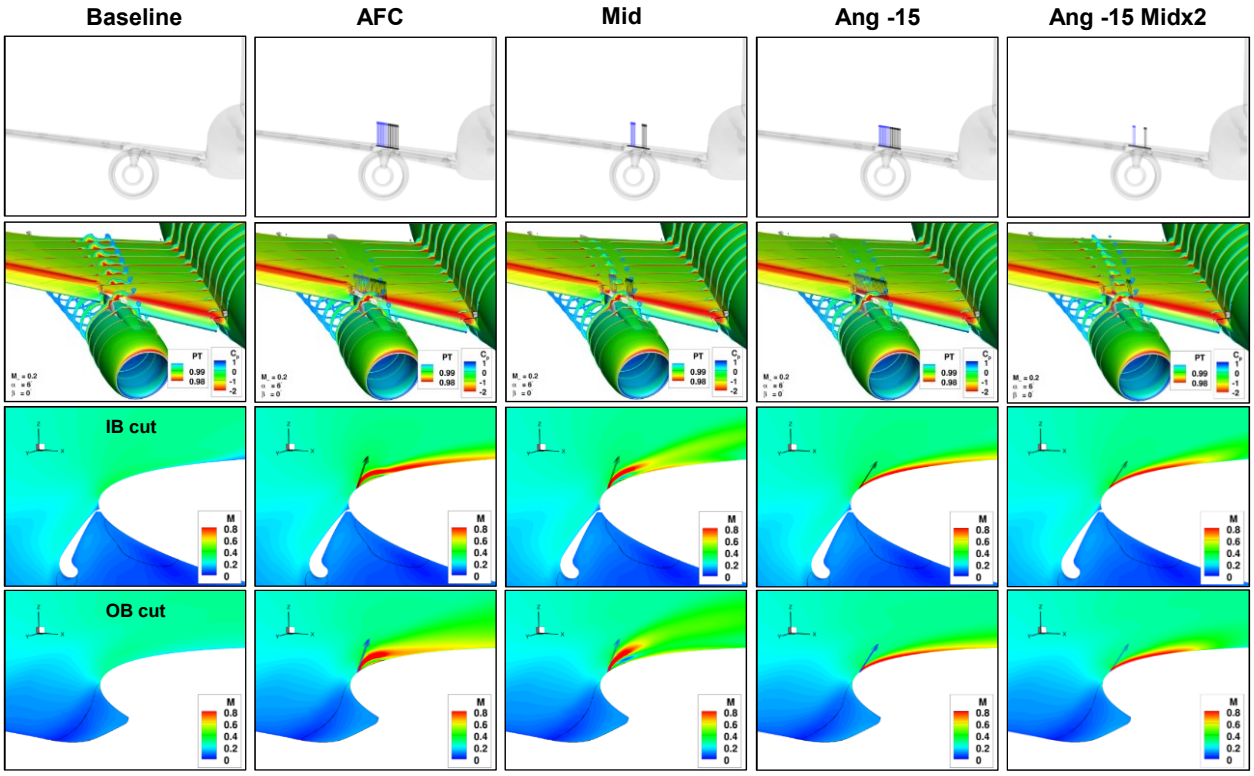

Figure 75 – AFC patterns for the nacelle/pylon/wing application, α=6°.

The separation progression for the baseline and the Ang -15 Midx2 flow control pattern with PR=4 is shown in Figure 77. The baseline flow indicates loss of lift at α=16° due to the separation originating at the slat edge while the controlled flow outright suppresses this flow feature. Instead, the critical separation points occur at α=18° and they shift to the leeward side of the engine cowl and the inboard section of the wing which is protected by the Krueger flap.

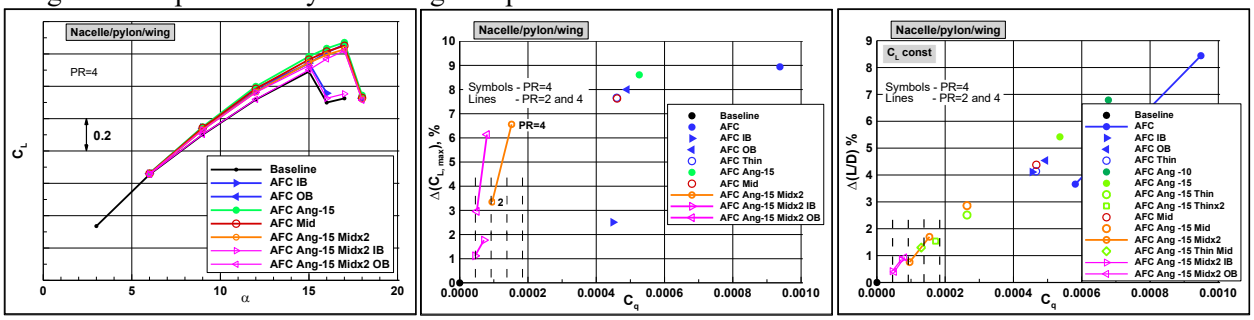

Figure 76 – Aerodynamic performance due to AFC at the nacelle/pylon/wing.

Figure 78 illustrates the difference between inboard vs outboard actuation with the Ang -15 Midx2 pattern and PR=4. Clearly the outboard actuation is most effective in preventing separation, commensurate with the aerodynamic characteristics in Figure 76. In fact, there is no material benefit in using the inboard actuation for either L/D or $C_{L,max}$ improvements for this flow condition. However, inboard actuation improves C_L in the linear range. Examination of the flow structure at α=15° in the top views of the baseline (Figure 77), the IB and OB actuation cases (Figure 78) reveals that the flow quality in the inboard wing section has improved with IB actuation, and the separation pocket at the trailing edge flap is reduced. However, beyond α=15° the separation off of the slat edge dominates the flow and stall ensues.

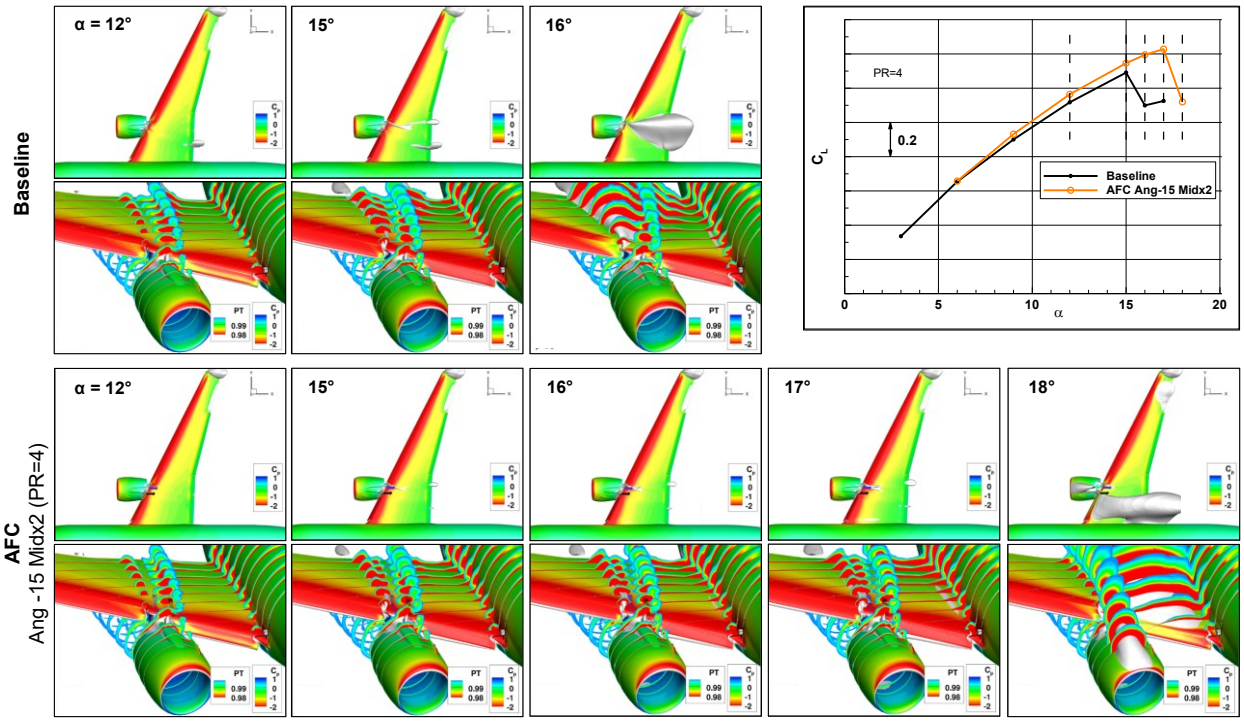

Figure 77 – Flow development with angle of attack for the baseline and the Ang -15 Midx2 pattern with PR=4.

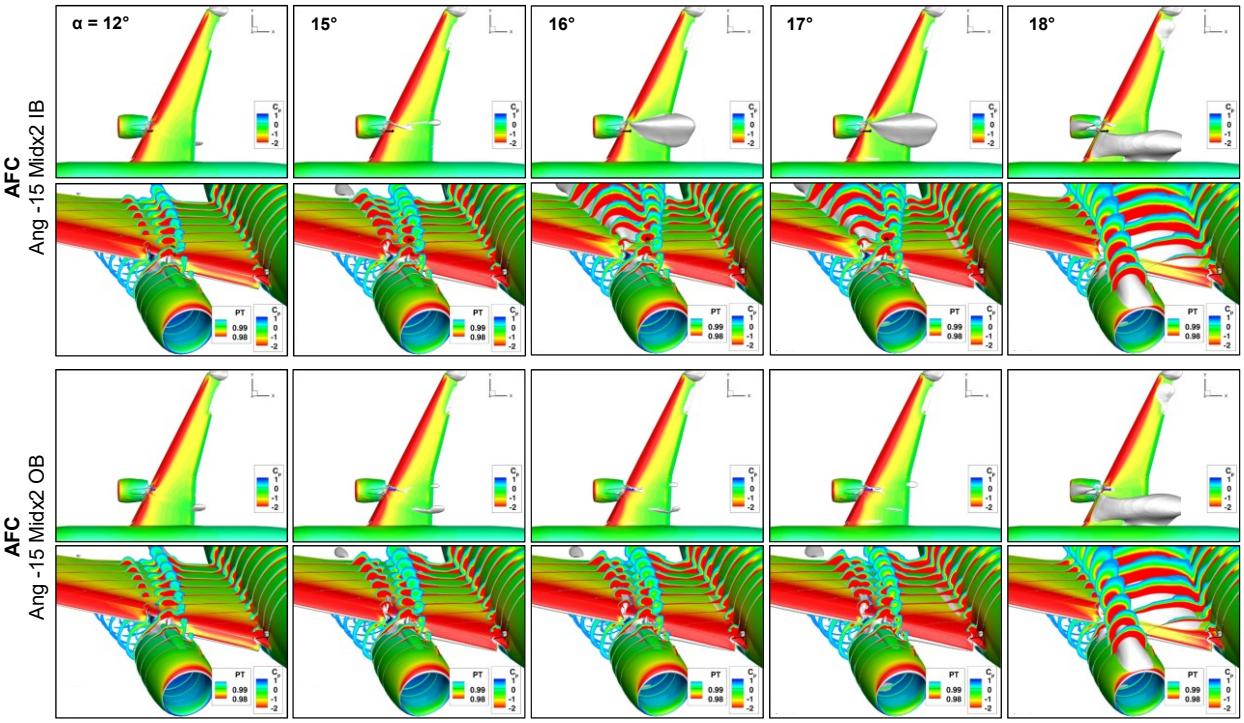

Figure 78 – Flow development with angle of attack for the inboard and outboard actuation, Ang -15 Midx2 patterns with PR=4.

5 Conclusions and Next Steps

Flow control approaches targeting three regions of the wing of a commercial airplane at high-lift conditions have been investigated. In one application, AFC is applied to the deflected aileron in order to reduce flow separation or outright remove it. The increased lift and the reduction in drag results in improved L/D during takeoff, which is a major determinant of airplane performance. The second class of flow control applications targets various locations in the wing leading edge regions, including the slats and the wing element. Depending on the specific applications, the objective is to reduce viscous effects and to control the vortical flow. The third flow control approach is aimed at reducing the interference effects and facilitate the integration of the engine with the wing high-lift system. Here the primary objective is to control the associated vortex system in order to enhance lift up to stall and beyond. The AFC methods have been designed for the least amount of actuation input in order to enable practical integration using onboard sources.

The aerodynamic benefits of some of the more promising AFC candidates are summarized in Figure 79. Significant gains are predicted within the onboard resources in both L/D and $C_{L,max}$, depending on the application. The system integration study (final report document #3 [3]) will help identify the most practical candidates.

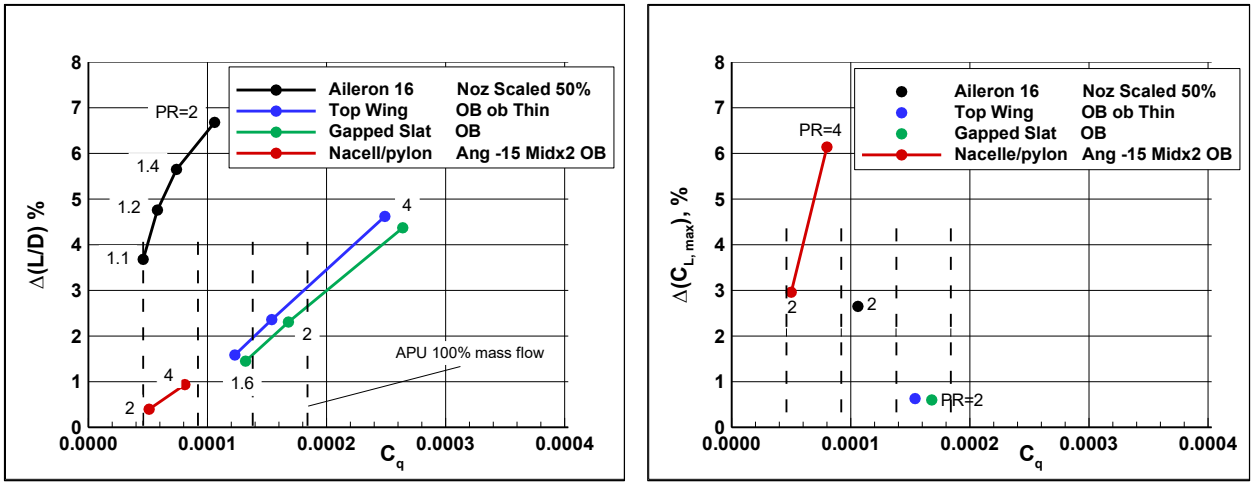

Figure 79 – Aerodynamic performance gains for some of the AFC applications considered in this study.

Next steps are focused around refinements of the estimated gains using more realistic geometrical definitions of both the airplane OML and actuation layouts. Additionally, completing the evaluations for the landing conditions will facilitate a more holistic analysis of net airplane benefits. Finally, there are other potential wing applications for improved airplane performance that have not yet been addressed in the framework of the current study. A more detailed list of the next steps are presented here:

- Incorporate realistic OML aileron
  - Surface curvature might affect AFC
  - Will result in a more accurate estimate of cruise drag penalty due to backward facing step in the integration study (final report document #3 [3])
- Incorporate more realistic representation of AFC using CD nozzle for LE and Nacelle/pylon/wing
  - Potential for improved aero performance, based on the aileron experience (Figure 23)
- Complete the aerodynamic performance for the landing conditions
- Evaluate unsteady actuation with Fluidic Oscillators
  - Potential for more efficient actuation
- Refine the implementations for higher efficiency by exploiting the sensitivities observed in the simulations with respect to the actuation parameters

  - Top-wing, Gapped-slat
  - Nacelle/pylon/wing
- Assess potential for attenuating low-speed buffet (Top-wing, Gapped-slat)
  - Wingtip separation
- Assess potential of enhanced high-lift performance by applying flow control in the flap cove
  - Preliminary internal Boeing study has shown promise

References

1. Whalen, E.A, Shmilovich, A., Spoor, M., Tran, J., Vijgen, P., Lin, J.C., & Andino, M., "Flight Test of an Active Flow Control Enhanced Vertical Tail", *AIAA Journal*, Vol. 56, No. 9, 2018, DOI: 10.2514/1.J056959
2. Garner, P., Meredith, P., & Stoner, R., "Areas for future CFD development as illustrated by transport aircraft applications", *AIAA 10th Computational Fluid Dynamics Conference*, Honolulu, HI, June 24-26, 1991, DOI: 10.2514/6.1991-1527
3. Vijgen, P., Ziebart, A., Shmilovich, A., & Woszidlo, R., "Low-Speed Performance Enhancement using Localized Active Flow Control – Integration Study of Localized Active Flow Control on a Performance Reference Aircraft", *NASA Technical Reports Server*, April, 2022, document ID: 20220006733
4. Buning, P.G., Chiu, I.T., Obayash, S., Rizk, Y.M., & Steger, J.L., "Numerical Simulation of the Integrated Space Shuttle Vehicle in Ascent", *15th AIAA Atmospheric Flight Mechanics Conference*, Minneapolis, MN, Aug 15-17, 1988, DOI: 10.2514/6.1988-4359
5. Shmilovich, A., & Vatsa, V., "Practical Computational Methods for Airplanes with Flow-Control Systems," *AIAA Journal*, Vol. 57, No 1, 2019, DOI: 10.2514/1.J056876
6. Shmilovich, A., "Unconventional Applications and New Approaches for Flow Control", in *Fundamentals of High Lift for Future Civil Aircraft*, *Notes on Numerical Fluid Mechanics and Multidisciplinary Design*, Springer book series, Vol. 145, Edited by Radespiel and Semaan, 2020, DOI: 10.1007/978-3-030-52429-6_1
7. Shmilovich, A., Yadlin, Y., & Whalen, E., "Computational Evaluation of Flow Control for Enhanced Control Authority of a Vertical Tail," *AIAA Journal*, Vol. 54, No 8, 2016, DOI: 10.2514/1.J054712
8. Shmilovich, A., Yadlin, Y., & Whalen, E., "Active Flow Control Computations: From a Single Actuator to a Complete Airplane," *AIAA Journal*, Vol. 56, No. 12, 2018, DOI: 10.2514/1.J056307
9. Shmilovich, A., Yadlin, Y., Dickey, D.E., Hartwich, M.P., & Khodadoust, A., "Development of an Active Flow Control Technique for an Airplane High-Lift Configuration," *AIAA SciTech Forum*, Grapevine, TX, Jan 9-13, 2017, DOI: 10.2514/6.2017-0322
10. Shmilovich, A., & Yadlin, Y., "Flow Control for the Systematic Buildup of High Lift Systems," *AIAA Journal of Aircraft*, Vol. 45, No. 5, 2008, DOI: 10.2514/1.35327
11. Chakravarthy, S., "A Unified-Grid Finite Volume Formulation for Computational Fluid Dynamics," *International Journal for Numerical Methods in Fluids*, Vol. 31, No. 1, 1999, DOI: 10.1002/(SICI)1097-0363(19990915)31:1%3C309::AID-FLD971%3E3.0.CO;2-M
12. Shmilovich, A. & Yadlin, Y., "Flow Control for Enhanced Airplane Takeoff Performance", *AIAA SciTech Forum*, Orlando, FL, Jan 6-10, 2020, DOI: 10.2514/6.2020-0784

Appendix A – AFC Layouts for the Slat Cove

Expanding on Section 4.2.2, a set of simulations have been performed using actuation in the coves of slats 4 and 3, or IB and OB segments per the notation of the planform inset in Figure 51, respectively. The jet is applied at the vertical section of the cove surface. Results have been obtained for the patterns listed in Figure 80 with PR=2 and TR=1. The freestream Mach number is 0.20 and Re=6 million. Simulation were obtained at α=6°. The baseline flow and the AFC patterns are described in Figures 81 through 88 (see list below). Different views and flow field cuts are used to describe the jet efflux and to visualize the impact of the actuation on the airplane flow.

Figure 81 - Baseline
Figure 82 - Streamwise jet, pointing in the x direction — str
Figure 83 - Jet perpendicular to LE in the xy plane — norLE
Figure 84 - Jet in xy plane, 45° off the surface, pointing towards the wingtip — xy45
Figure 85 - Jet in xy plane, 20° off the surface, pointing towards the wingtip — xy20
Figure 86 - Jet in xz plane, 20° off the surface, pointing up — xz20
Clockwise within the cove
Figure 87 - Jet in xz plane, -20° off the surface, pointing down — xzm20
Counterclockwise within the cove
Figure 88- Jet in xy plane, 20° off the surface, IB Slat — xy20 IB
Nearly all patterns listed were also evaluated separately on the IB and OB slats
Figure 90 - Jet in xy plane, 20° off the surface, middle IB and OB slats — xy20 Mid
Figure 91 - Jet in xy plane, 20° off the surface, Segmented — xy20 Seg

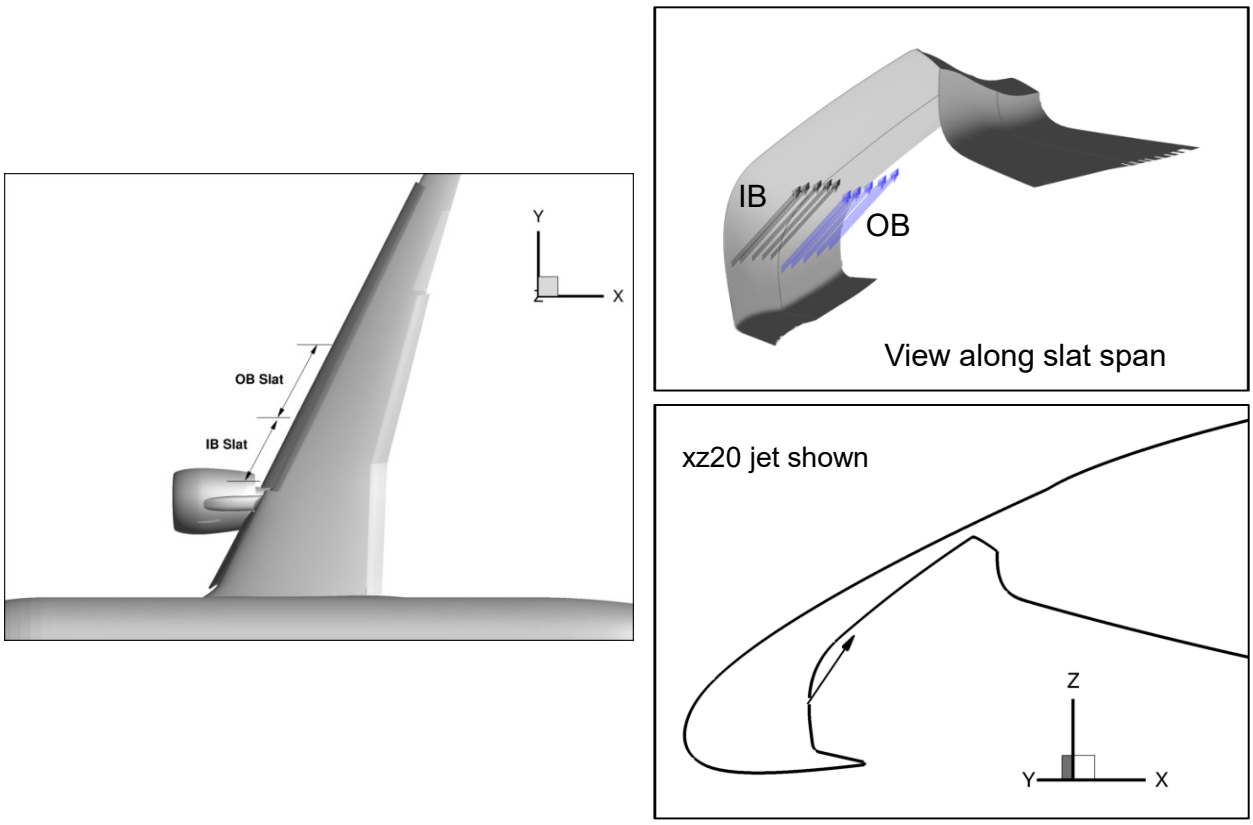

Figure 80 – Actuation patterns investigated for the slat cove application.

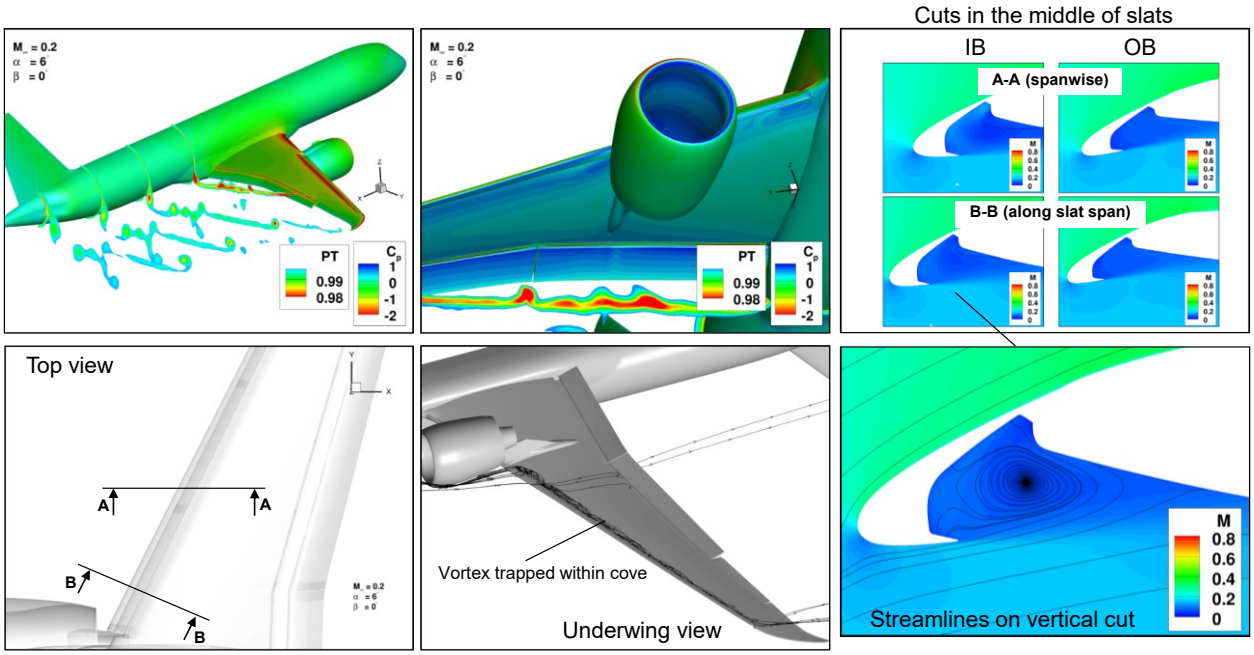

Figure 81 – Baseline flow.

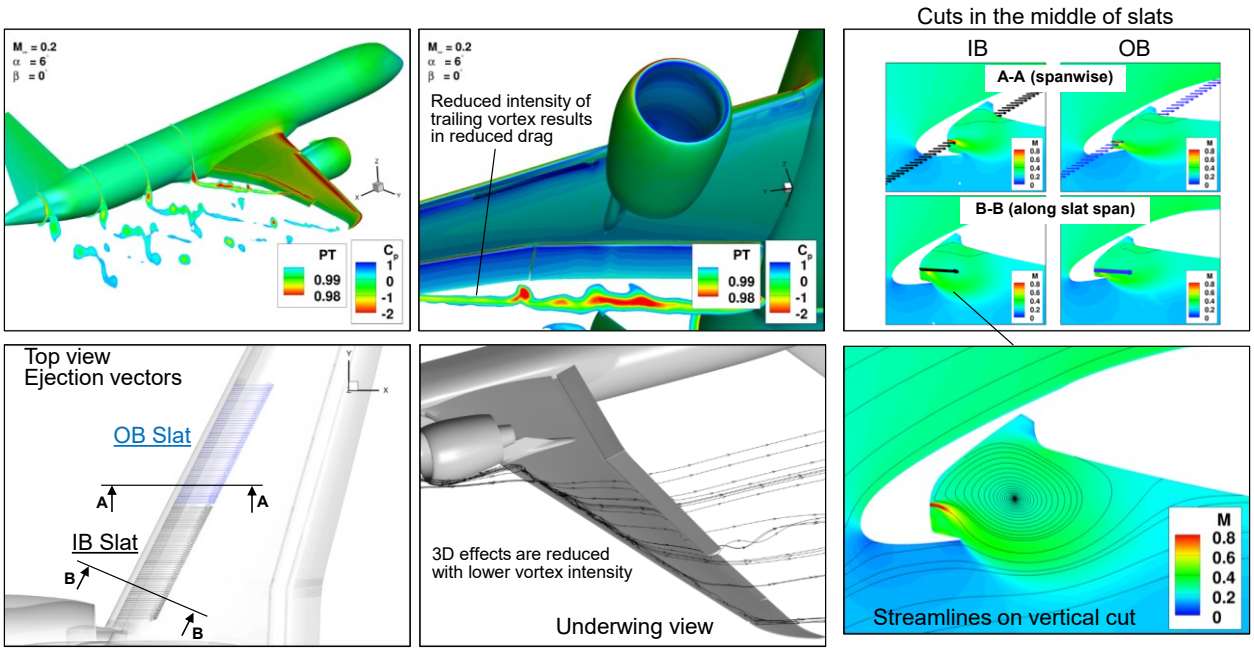

Figure 82 – Streamwise jet: str.

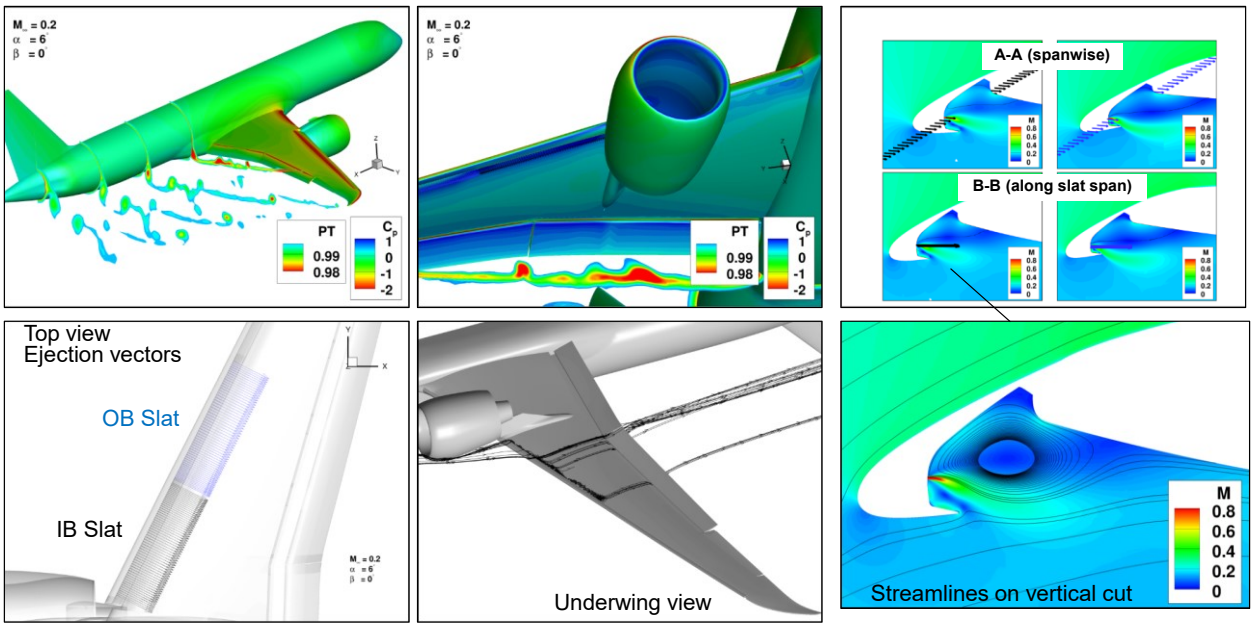

Figure 83 – Jet perpendicular to the wing LE: norLE.

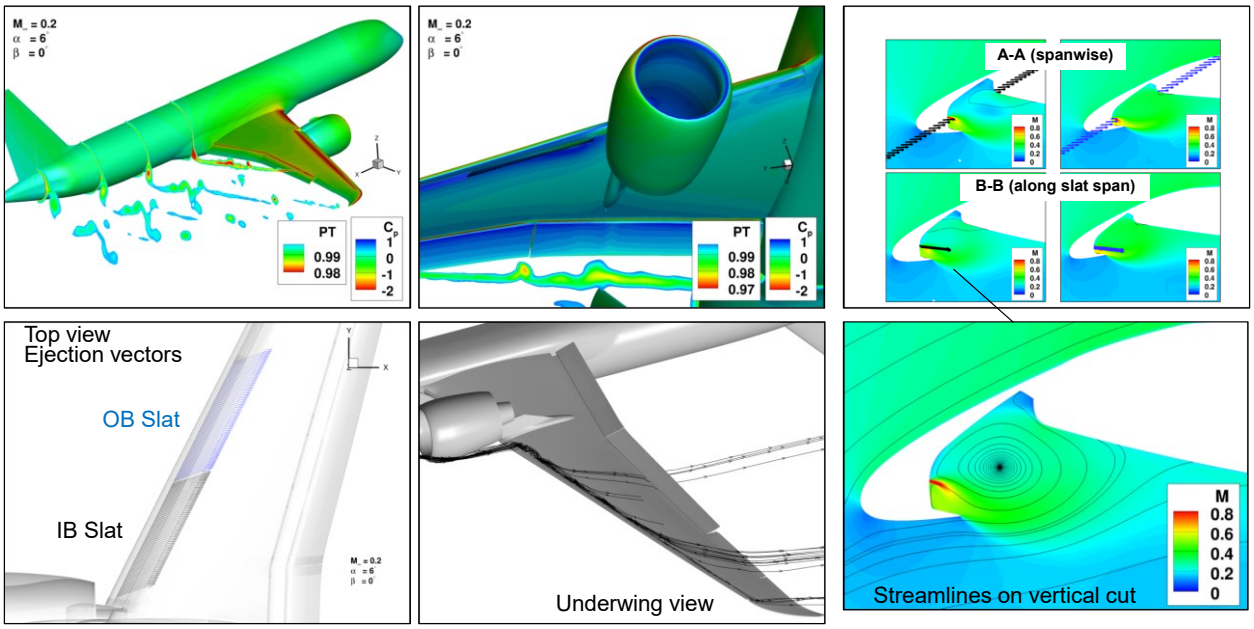

Figure 84 – Spanwise jet component: xy45.

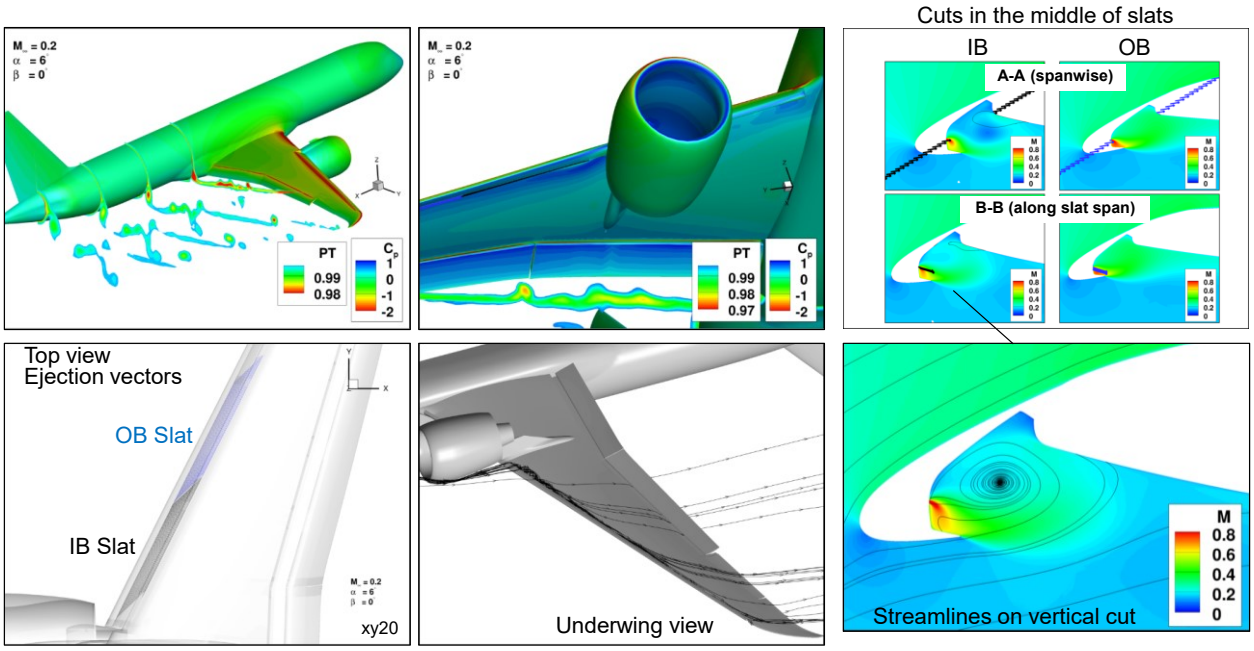

Figure 85 – Spanwise jet component: xy20.

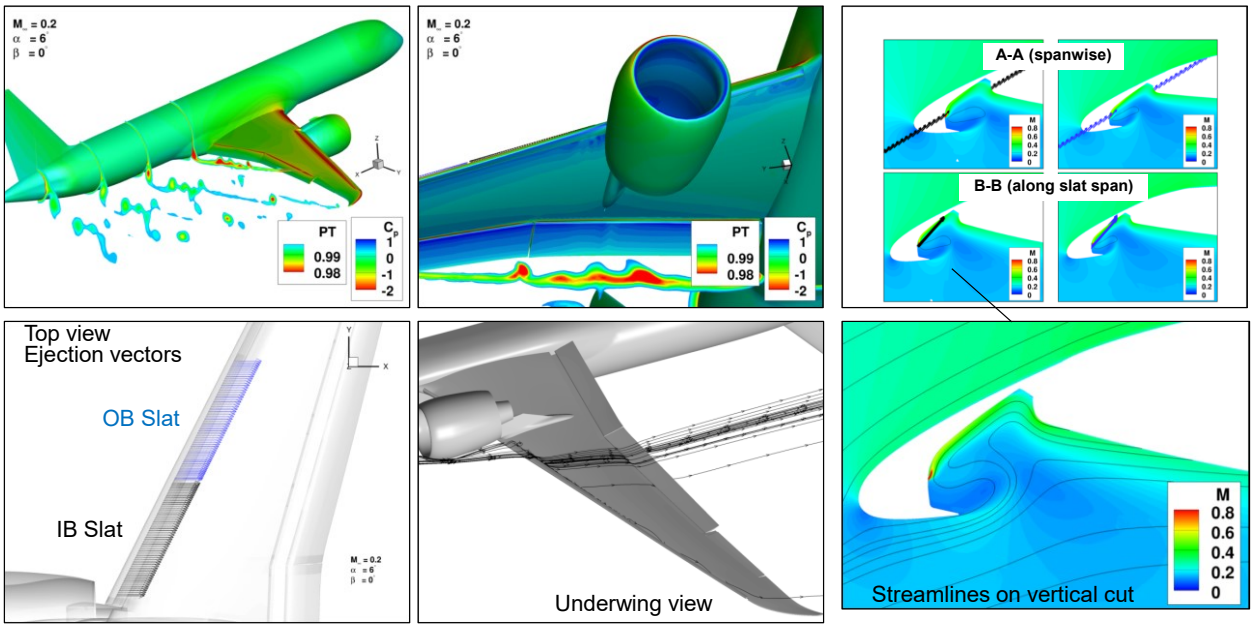

Figure 86 – Clockwise jet (in the vertical plane): xz20.

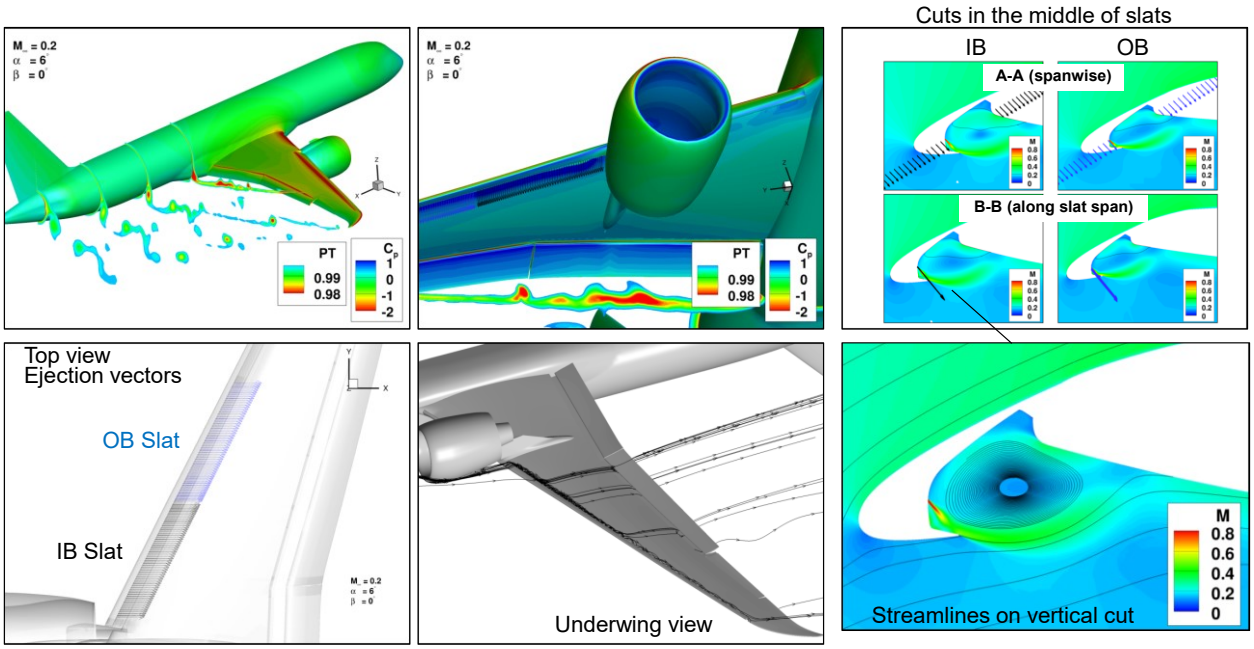

Figure 87 – Counterclockwise jet (in the vertical plane): xzm20.

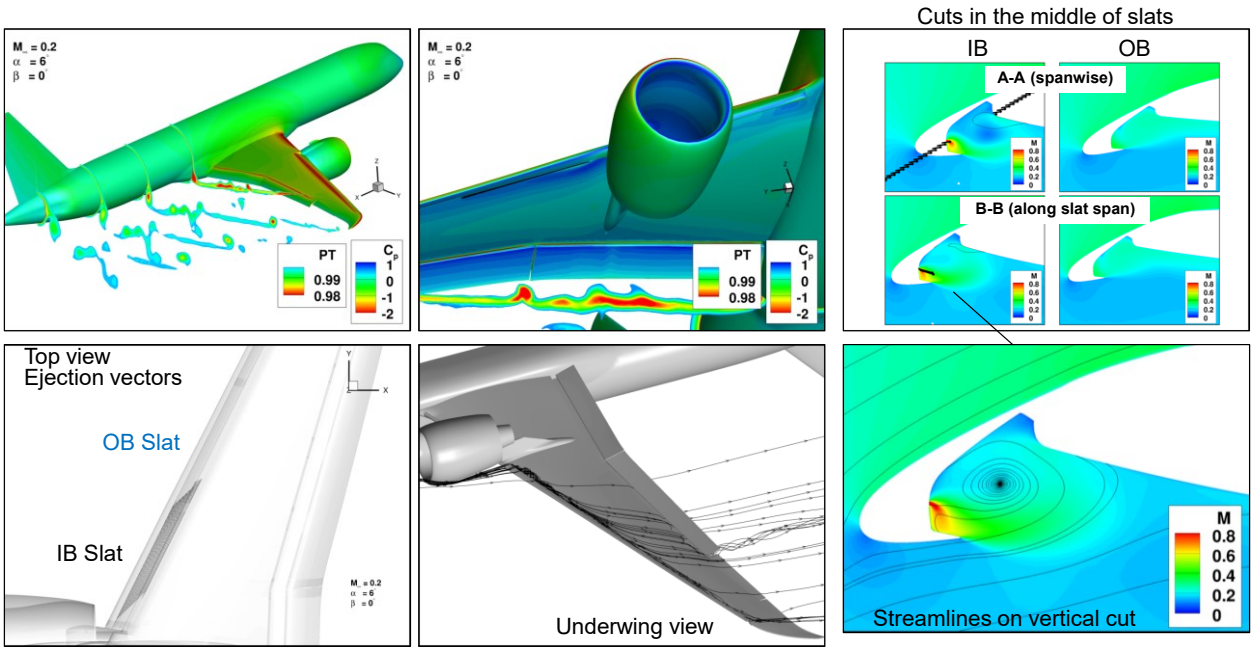

Figure 88 – Spanwise jet component on IB slat: xy20 IB.

The various patterns have different effects on the flow field. However, a more useful comparison takes into account the actuation input in Figure 89. Not all the patterns considered above are included in the plot. Since the jet is applied on a fixed strip along the slat as defined by the surface grid, as the jet angle varies, the mass flow coefficient changes according to the dot product of the area vector and the jet efflux vector, $C_q \sim \mathbf{A}\cdot\mathbf{U}$. These jet patterns were evaluated separately on the IB and OB slats, and on both IB and OB. Each pattern consists of the set of IB, OB and IB+OB applications, denoted by 1, 2 and 3 on the symbols in Figure 89, respectively. Note that $C_q3 = C_q1 + C_q2$. Also, C_q1 is slightly higher than C_q2. The results

indicate that patterns xy45 and xy20 are the most efficient. However, the actuation input is excessive, since C_q of ~0.00018 corresponds to the mass flow that could potentially be supplied by an APU. In order to lower the actuation input to acceptable levels, two more jet layouts (Figures 90 and 91), have been investigated in conjunction with xy20. Those flow fields are presented in Figures 90 and 91. The L/D gains are summarized in Figure 92, where case xy20 corresponds to the point labeled 3 in Figure 89. These patterns use smaller jet area. Although C_q has been reduced, further improvements have to be made in order to bring the actuation level down to practical levels. Further refinements to the slat cove application will be addressed in Section 4.2.2.

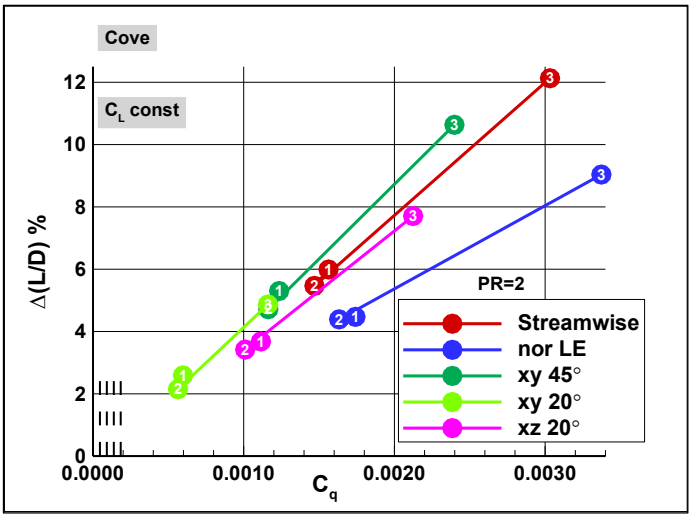

Figure 89 – Aerodynamic performance vs actuation input.

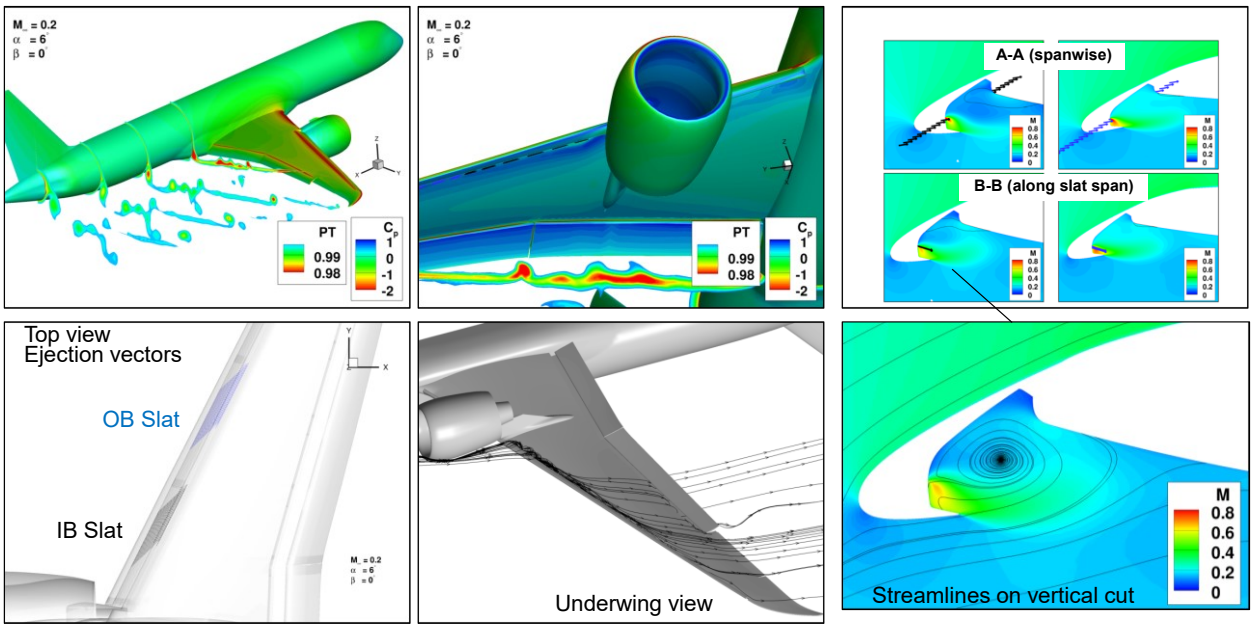

Figure 90 – Jet at the middle of the slats: xy20 Mid.

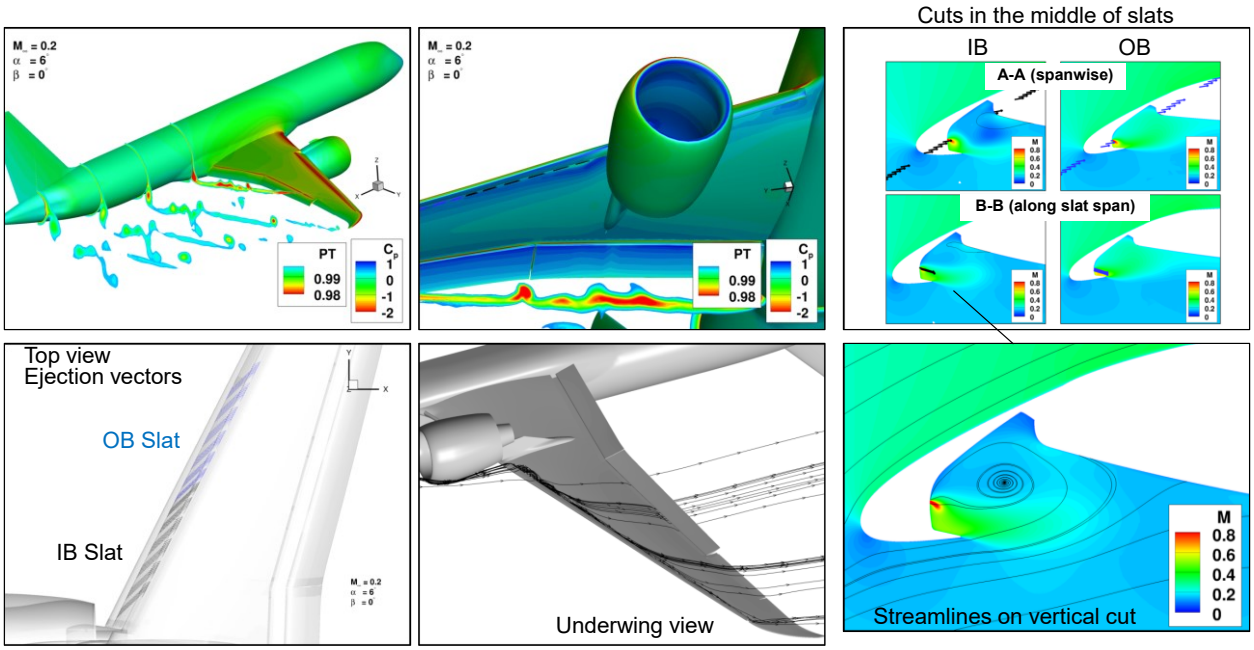

Figure 91 – Span segmented jets: xy20 Seg.

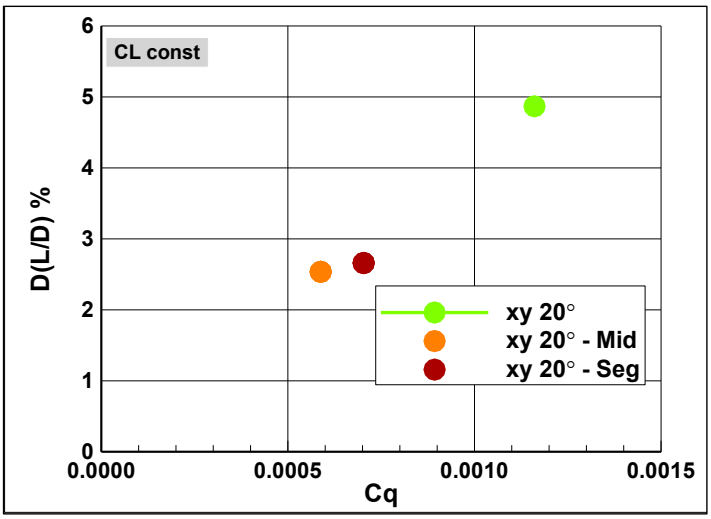

Figure 92 – Aerodynamic performance vs actuation input, xy20 applied on both IB and OB slats.

Appendix B – AFC for All Gapped Slats

This portion of the study laid the groundwork for the outboard gapped slat described in Section 4.2.6. The grid system incorporated gapped slats on all four elements and all the solutions are obtained on the same grid. Figure 93 shows the results for AFC applied at all slat elements for a set of PRs. The ejection vectors of the individual slats are color coded. The jet location in these cases is considered nominal and they have a nominal width. The cross-sectional cuts show the flow development at the gap as function of actuation intensity, similar to the description in Section 4.2.6 for the Slat 2 application. Although quite effective in augmenting AFC, actuation input is excessive. The effect of jet location in relation to the gap is shown in Figure 94, where upstream (Ups) and downstream (Dns) placements are considered for PR=2. In terms of L/D, the predictions indicate slightly higher effectiveness when the jet is closer to the gap. Effects of jet size are described in Figure 95 for PR=2. The jets labeled 'Mid' imply 50% smaller spanwise jets applied at the center of each of the slat elements. Since the same grid system is being used in this case, the unactuated span segments remain gapped. The jets marked 'Thin' are half the size of the nominal jet width. The different jet sizes have approximately the same effects on L/D.

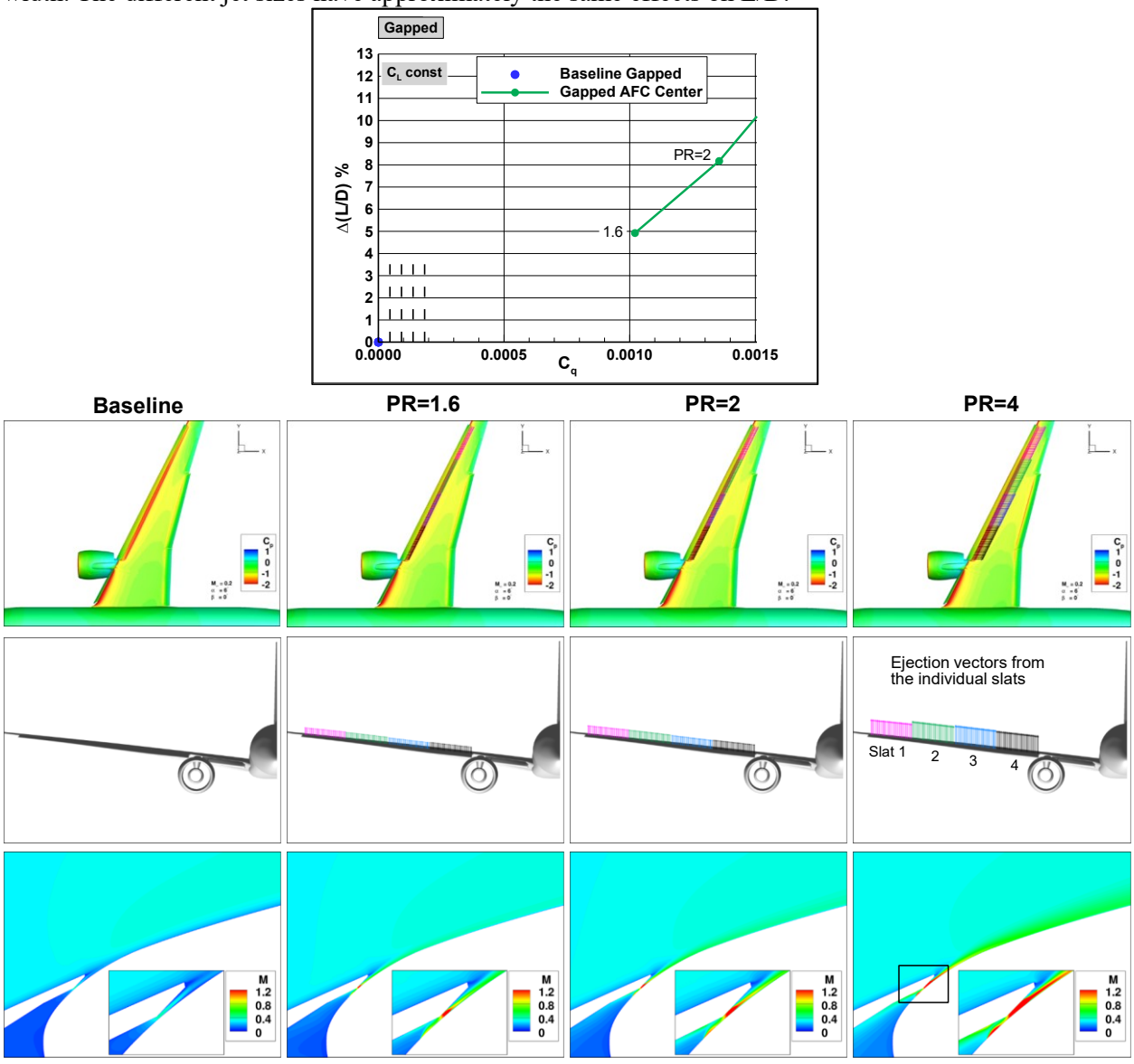

Figure 93 – AFC applied to all Gapped slat elements.

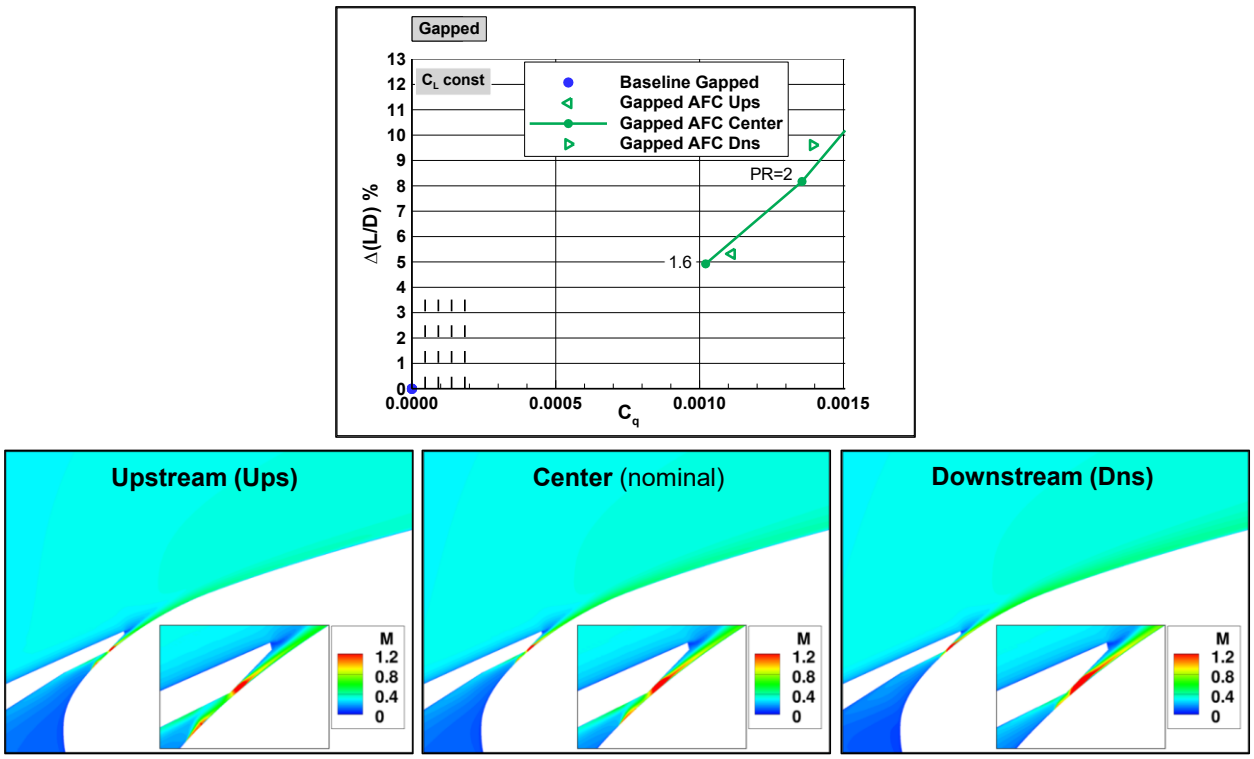

Figure 94 – Effect of jet location on gapped slats.

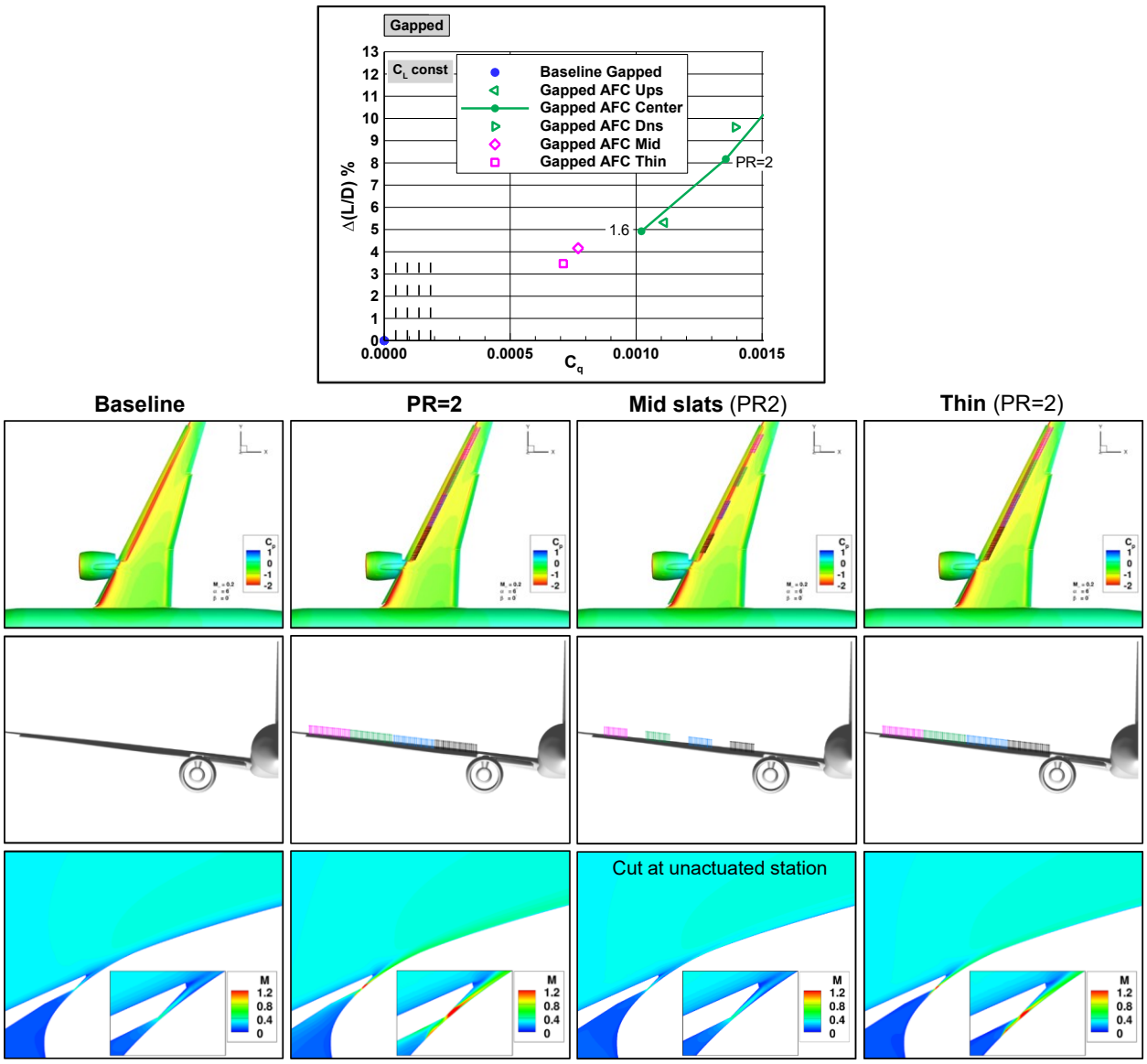

Figure 95 – Effect of jet size on gapped slats.

The effect of actuation on the individual slats is shown in Figure 96. A different notation is adopted here, where slat 4 is marked IB1, slat 3 is IB2, salt 2 is IB3 and slat 1 is IB4. It is noted that the mass flow of the slats are not the same because the jet conditions are applied along grid strips and the grid distribution is proportional to the local chord. Hence the C_q of the inboard slats are higher than the outboard slats. Similar to other LE applications in Section 4.2, here too the outboard actuation is more effective. The L/D gains for actuation on just IB4 (slat 1) for a set of AFC patterns (as in Figures 94 and 95) are shown in Figure 97. Here IB4 OB indicates actuation on the outboard 50% of the outboard slat. There are a number of jet configurations that look attractive in terms of L/D gains per input comparable to the APU supply. However, examination of the lift curve in Figure 98 obtained for this grid system with all gapped slats reveals that there is a notable degradation in maximum lift compared to the sealed slat configuration. Since the intent is to use flow control only on the outboard slat, a new grid system had to be developed such that only the actuated slat is gapped. This part of the analysis is described in Section 4.2.6.

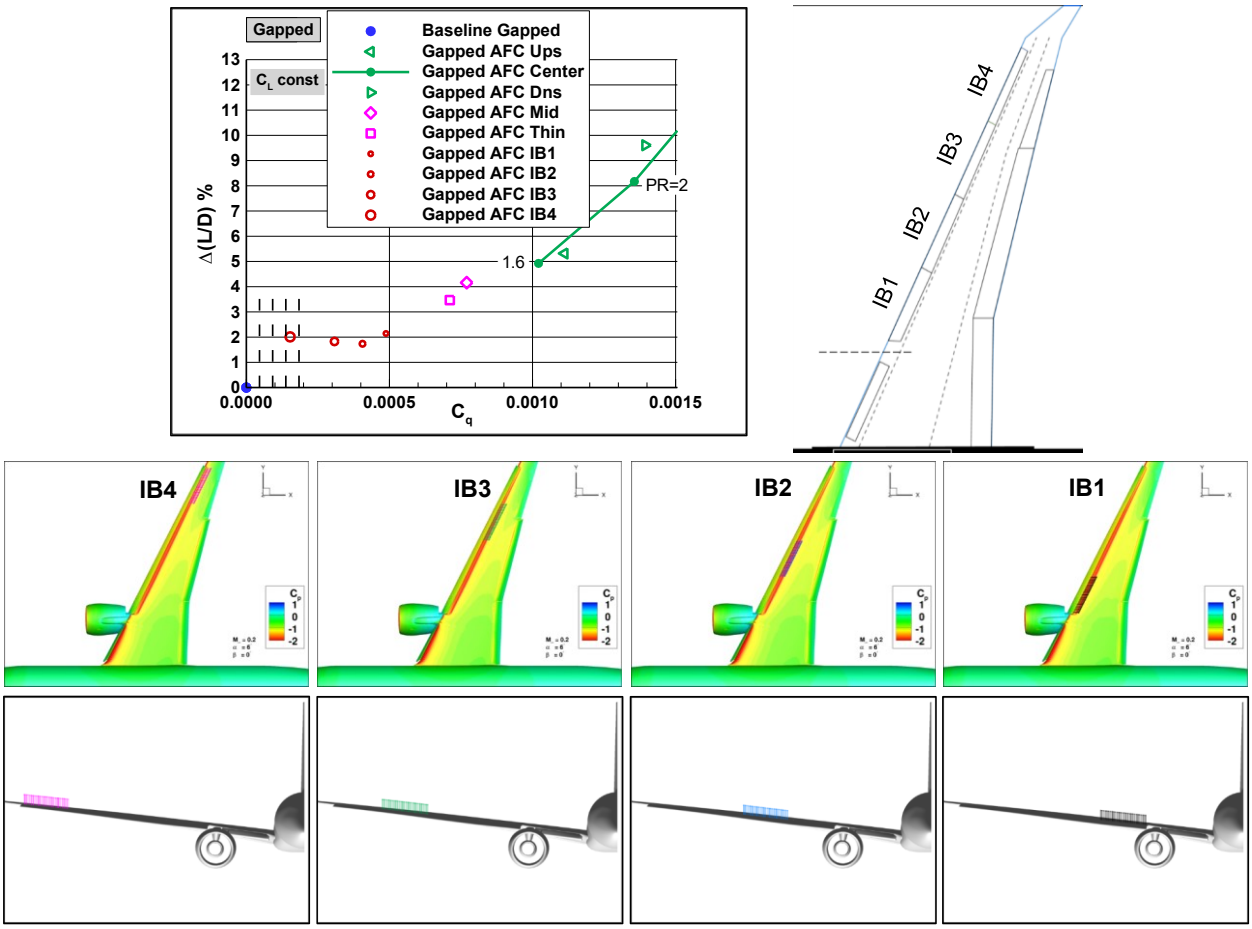

Figure 96 – Actuation applied at individual slat elements.

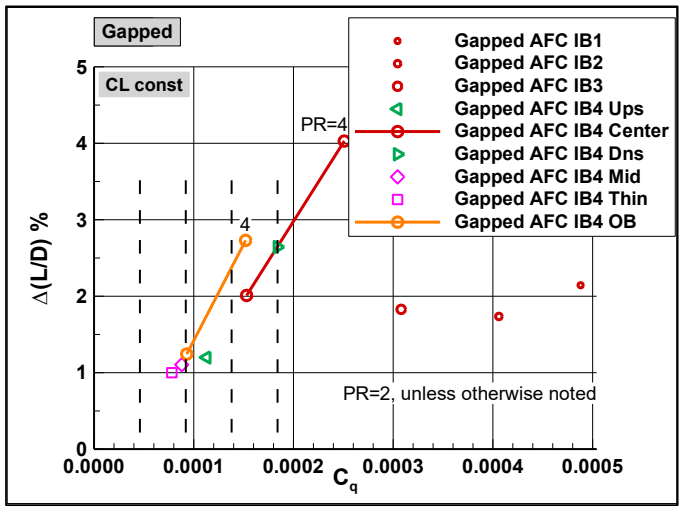

Figure 97 – Actuation patterns for the Gapped slat with actuation on the outboard slat IB4.

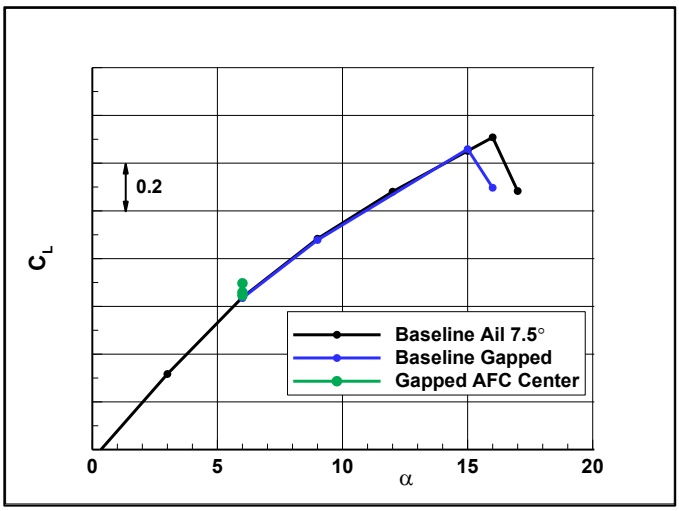

Figure 98 – Degradation in maximum lift due to unactuated gapped slats.